Measurement of $\sin(2\phi_1)$ using $J/\psi\ K_L^0$ decay of B mesons

（ B 中間子の $J/\psi\ K_L^0$ 崩壊による $\sin(2\phi_1)$ の測定 ）

樋口　格

平成 15 年

Abstract

We present a measurement of a time-dependent difference between the decay rate $B_d^0 \to J/\psi K_L$ and the decay rate of its charge-parity (CP) conjugate, $\bar{B}_d^0 \to J/\psi K_L$.

In the standard model (SM) of paricle physics, such CP-violation in the weak interactions can be accomodated via the Kobayashi-Maskawa (KM) mechanism, which is known as the Cabbibo-Kobayashi-Maskawa (CKM) matrix. This model predicts the time-dependent CP-asymmetry, $A(t)$, to take the form

$$A(\Delta t) \equiv \frac{\Gamma_{\bar{B}_d^0 \to J/\psi K_L^0} - \Gamma_{B_d^0 \to J/\psi K_L^0}}{\Gamma_{\bar{B}_d^0 \to J/\psi K_L^0} + \Gamma_{B_d^0 \to J/\psi K_L^0}} = -\sin 2\phi_1 \cdot \sin(\Delta m_d \cdot \Delta t)$$

where $\phi_1 = arg(-V_{cd}V_{cb}^*/V_{td}V_{tb}^*)$ is convention-independent combination of CKM matrix elements, and Δm_d is the mass differnce between the B_d meson mass eigenstates. The ϕ_1 can be interpreted as one of the three inner angles of the "CKM Unitarity Triangle" which is the graphical representation of the unitarity condition

$$\sum_{i=u,c,t} V_{ij}V_{ik}^* = \delta_{jk} \quad (j,k = d,s,b).$$

Using $140/fb$ of e^+e^- collition data (≈ 152 Million $B\bar{B}$ Pairs) collected with the Belle detector at the KEKB accelerator, we reconstruct 2332 $B^0 \to J/\psi\ K_L^0$ candidates after vertexing and flavor tagging. Using these candidates, we measure

$$\sin 2\phi_1 = 0.747 \pm 0.128(statistical) \pm 0.057(systematic).$$

Acknowledgements

Feb 2004
Higuchi Itaru

I would likel to acknowledge everyone who helped me directly or indirectly to complete this thesis. But it may need almost an infinite list to do so. Here I would like to express my graritude to those who especially impressed me.

I would like to express my gratitude to my supervisor, A. Yamaguchi, giving me an opportunity for the research in the wonderful world of high energy physics and for his support for my research and guidance for my research activity.

I am grateful to H. Yamamoto. He taught me not only about high-energy phisics, but also other analysis. He adviced me to understand more deeply.

I thank my advisor, T. Nagamine, for his kind and parient guaidance during my Belle years.

I am deeply thankful to the members of KLM group. K.Abe, Y.Hoshi, D.Marlow, Y.Mikami, E.Nakano, K.Neichi, T.Sarangi, Y.Teramoto, Y.Yusa and J.G.Wang helped me to understand KLM system by software and hardware both sides.

It was a pleasure to meet and work with all the talented and intersting individuals in the charmonium, flavor tag and CP-fit groups. The analysis presented in this thesis builds on, and incorporates the work of many. Among them are K. Hanagaki, S. E. Vahsen, M.Yamaga, M. Yokoyama, who all worked directly on the $B^0 \rightarrow J/\psi\ K_L^0$ analysis. K.Miyabayashi coordinated and guided charmonium study, and A.Ishikawa and T.Tsukamoto help to generate charmonium Monte Carlo for a short period of time. M. Hazumi and Y. Sakai coordinated and guided the CP-violation measurement efforts at KEK. K. Hara, T. Higuchi, H. Kakuno, K. Sumisawa, T. Shibata and T. Tomura wrote the flavor tagging, CP-fittig and vertexing software, and I greatly appreciate their kind assistance on many occasions.

Y.Enari, T.Hokuue, Y.Iwasaki, Y.Unno are my smoker friends during my Belle yeares. I enjoyed my smoking life without any sick.

My appreciation goes to A. Suzuki, J. Shirai, F. Suekane, K. Inoue, T. Hayashino, T. Hasegawa, M. Koga, Y. Kishimoto, K. Tamae, H. Ogawa, T. Iwamoto, S. Enomoto, H. Watanabe and other RCNS (Research Center for Neutrino Science, Tohoku University) members. I enjoyed my Sendai life.

During the Tohoku years, I enjoyed fellowship with the other students and graduated students, Y. Gando, F. Handa, H. Ikeda, T. Kawaguchi, H. Kinoshita, N.

Murono, K. Tsuchiya, K. Watanabe and T. Yoshida.

Finally, I would like to thank my family who have been supported and encouraged me for along time. My parents, Takuya and Shizue Higuchi have been continuously supporint me since I was born. My brother Tamotsu also supported me in various ways. Althogh we are liveing aparte from each other, I believe we always connet as family.

Contents

List of Figures

List of Tables

Chapter 1

Introduction

One of the ultimate studies in modern science is to understand a universe is made of *matter*, not "$anti-matter$" or not both. The population of $anti-matter$ is very small now and $anti-matter$ is unstable. However, according to the theory of cosmology, the population of $anti-matter$ is produced as same as that of *matter* at the beginning of the universe. Where does $anti-matter$ go ? What is the difference between *matter* and $anti-matter$?

A.Sakharov pointed out that there are three essential elements of construct theories which can explain the difference between *matter* and $anti-matter$ in the universe [1].

1. departure from thermal equilibrium.
2. In the early universe, there are reactions which changes baryon number.
3. CP-violation is occurred.

Here, CP-violation means that there exists the difference between *matter* and $anti-matter$. Therefore CP-violation is one of the fundamental phenomenon to understand the history of the universe.

Physicist consider that there was only charged asymmetry between *matter* and $anti-matter$. But Fitch-Cronin observed that CP-violation in K_L^0 decay in 1964 [2]. After that, great efforts were made to understand this CP-violation by both sides of an experiment and theory.

In 1973, Kobayashi and Maskawa noted the theory of quark mixing which can introduce CP-violation within the framework of the Standard Model of elementary particle physics. They demonstrated that quark-flavor mixing matrix with measurable complex phase introduces CP-violation into quark interactions. This requirement is satisfied if there are at least six flavors of quarks, while only three types of quarks we known when KM proposed their model.

In 1980, Sanda and Carter pointed out that the KM mechanism contained the possibility of large CP-violation in certain decay mode of the B meson [3].

In this thesis, we present a measurement of the CP-asymmetry in the $B^0 \rightarrow J/\psi\ K_L^0$ decay using $140/fb$ data sample (152 million B and $\bar{B}$ pairs) collected at the $\Upsilon(4S)$ resonance with the Belle detector at at KEK B-factory (asymmetric e^+e^- collider). Outline of this thesis is following:

- In Chapter 2, we explain theoretical description of CP-violation in neutral B^0 meson system and how to approach to measure it.
- In Chapter 3, we explain experimental system used in this thesis.
- In Chapter 4, we explain the reconstruction and selection of $B^0 \rightarrow J/\psi\ K_L^0$ decay.
- In Chapter 5, we measure CP-asymmetry parameter $\sin 2\phi_1$.
- In Chapter 6, we conclude and discuss about our result.

Chapter 2

CP-Violation in the Neutral B Meson System

In this chapter, we introduce CP-violation in neutral B meson system. First we discuss the "Symmetry" in physics. Then, we consider a historical flow until finding P-violation and CP-violation in neutral K meson system. Next, we discuss to understand CP-violation under the Standard Model by Kobayashi-Maskawa mechanism. Finally, we introduce CP-violation parameter in neutral B meson system to observe at Belle.

2.1 Symmetries

Symmetries are very important factors in physics. Basically, we consider that physics is symmetrical. And we try to find theoretical rules under the Symmetries or Asymmetries which is considered symmetrical. In particle physics, there are three elemental Symmetries which are symmetrical under C, P, T transformation.

1. Parity (P) : Reverse three-dimensional coordinates transformation;
   $P|(t,x,y,z)\rangle = |(t,-x,-y,-z)\rangle$.
2. Charge conjugation (C) : Turn particles(anti-particles) into their anti-particles(particles) transformation.
   $C|f\rangle = |\bar{f}\rangle$ and $C|\bar{f}\rangle = |f\rangle$.
3. Time reversal (T) : Inversion of the time coordinate.

If the particle state is eigenstate of these symmetries or combination of them, the particle has eigenvalue which is $+1$ or -1. We call these eigenstate of $+1(-1)$ by even(odd) state.

In past we consider that C, P, T symmetries and the combination of these symmetries, CP and CPT are invariant under the electromagnetic, strong and weak interaction.

2.2 Kaon system

2.2.1 Party-violation

In past, we have been considered that party is invariant under the electromagnetic, strong and weak interaction. But in 1957, two strange decays are found, called "$\theta - \tau$ puzzle". In this case, two particles, which are named θ and τ, decay into different pion state,

$$\begin{aligned} \theta &\rightarrow \pi^+\pi^0 \\ \tau &\rightarrow \pi^+\pi^+\pi^-, \end{aligned}$$

but we can not distinguish theirs mass and lifetime even if these particle's parity are opposite. Why these particle's mass and lifetime are same even if these parity are different?

In 1956, T.D. Lee and C.N. Yang solved this problem. They investigated the past experiments and noticed that parity invariance had been verified sufficiently in the electromagnetic and strong interaction, but there was no experimental confirmation in weak interactions. They proposed that θ and τ are the same particle, which is called K^+ now, and parity is violated in one of them decay.

2.2.2 Neutral kaon system

We can describe eigen states of CP transformation with mixture of the two states K^0 and $\bar{K}^0$,

$$\begin{aligned} |K_1^0\rangle &= \frac{1}{\sqrt{2}}\left(|K^0\rangle + |\bar{K}^0\rangle\right) \\ |K_2^0\rangle &= \frac{1}{\sqrt{2}}\left(|K^0\rangle - |\bar{K}^0\rangle\right) \end{aligned}$$

where $CP|K^0\rangle = |\bar{K}^0\rangle$, $CP|\bar{K}^0\rangle = |K^0\rangle$. Thus $CP|K_1^0\rangle = +|K_1^0\rangle$, $CP|K_2^0\rangle = -|K_2^0\rangle$. If we consider decay into pions, $CP|2\pi\rangle = +|2\pi\rangle$ and $CP|3\pi\rangle = -|3\pi\rangle$. Therefore, only K_1^0 can decay into 2π and K_2^0 can decay into 3π.

$$\begin{aligned} |K_1^0\rangle \rightarrow 2\pi \quad &, \quad |K_1^0\rangle \not\rightarrow 3\pi \\ |K_2^0\rangle \rightarrow 3\pi \quad &, \quad |K_2^0\rangle \not\rightarrow 2\pi \end{aligned}$$

We can expect that the lifetime of K_2^0 is longer than that of K_1^0, because $M_\pi \approx 135\ MeV/c^2$ and $M_K \approx 500\ MeV/c^2$. So phase space for $|K_2^0\rangle \rightarrow 3\pi$ [1] is smaller

---

[1] $Q = m_K - \sum_{i=1}^{n} m_\pi$

compared with $|K_1^0\rangle \to 2\pi$, we call K_1^0 by K_S^0 ("short" lifetime) and K_2^0 by K_L^0("long" lifetime). Actually, the lifetime of these particles are,

$$\begin{array}{lllllll} \tau_{K_S^0} & = & 0.8926 & \pm & 0.0012 & \times 10^{-10} & \text{s} \\ \tau_{K_L^0} & = & 5.15 & \pm & 0.04 & \times 10^{-8} & \text{s.} \end{array}$$

If CP invariance is not violating, K_L^0 can not decay into two pions. Because K_L^0 is CP-even state. But, in 1964, Fitch-Cronin found that CP is violating under weak interaction in neutral K_L^0 decay. They observed fraction of K_L^0 meson decay into $\pi^+\pi^-$. [2]

$$BR(K_L^0 \to \pi^+\pi^-) \equiv \frac{\Gamma(K_L^0 \to \pi^+\pi^-)}{\Gamma(K_L^0 \to all)} = (2.0 \pm 0.4) \times 10^{-3}.$$

The fact of $K_L^0 \to \pi^+\pi^-$ is concluded that K_L^0 is not pure K_1. So, we can re-write K_L^0 and K_S^0 as follows,

$$\begin{aligned} |K_S^0\rangle &= \frac{|K_1^0\rangle + \epsilon_S|K_2^0\rangle}{\sqrt{1+|\epsilon_S|}} \\ |K_L^0\rangle &= \frac{|K_2^0\rangle + \epsilon_L|K_1^0\rangle}{\sqrt{1+|\epsilon_L|}} \end{aligned}$$

where $\epsilon_{S,L}$ is parameter of mixture. In other words, K^0 changes to $\bar{K^0}$ and $\bar{K^0}$ changes to K^0 in time dependent. Figure 2.1 shows feynman diagram this oscillation.

This was first observation of CP-violation. Now, we consider that C, P, T symmetries and combination of these symmetries, CP, are invariance under electromagnetic and strong interaction, and these are violating under weak interaction, and combination of three symmetries, CPT, is invariance under electromagnetic ,strong and weak interaction.

2.3 KM matrix and unitarity triangle

2.3.1 Cabibbo angle

Measurement of the semi-leptonic decay, when we compare decay rates whose change of strangeness, Δs, equals 1 and whose change of strangeness equals 0, it was suppressed by factor 20. It is not only K's leponic decay but also general decay whose Δs is not equals 0. In other word, decays whose $\Delta s \neq 0$ are conformed to same regulations universally. But between $\Delta s = 0$ and $\Delta s \neq 0$, there is no regulation. In 1963, N.Cabibbo proposed that particle state does not necessarily need to be in the state of mass. It is allowed that mixture of state of mass [4].

---

[2] In 1967, $K_L^0 \to \pi^0\pi^0$ decay is also found.

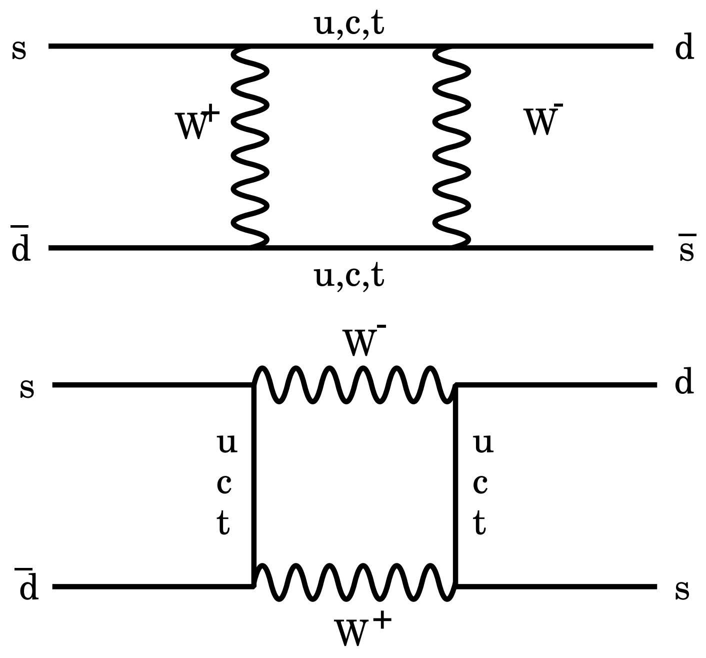

Figure 2.1: $K^0 - \bar{K}^0$ diagrams

We can write s and d quark states in weak interaction that they are rotation of pure d and s flavor eigensates with Cabibbo angle, θ_c

$$\begin{pmatrix} |d'\rangle \\ |s'\rangle \end{pmatrix} = \begin{pmatrix} \cos\theta_C & \sin\theta_C \\ -\sin\theta_C & \cos\theta_C \end{pmatrix} \begin{pmatrix} |d\rangle \\ |s\rangle \end{pmatrix}. \tag{2.1}$$

By experimental results, we know

$$\sin\theta_C \approx 0.22 \ , \ \ \cos\theta_C \approx 0.98. \tag{2.2}$$

2.3.2 Kobayashi-Maskawa matrix

In 1973, M. Kobayashi and T.Maskawa suggest theory of weak interaction [5]. It is concluded that no realistic models of CP-violation exist in the quartet scheme without introducing any other new fields. In this theory, CP-violation is occurred if mixing matrix , V becomes $N \times N$ unitary matrix. N^2-dimensional real variable space, we can define ${}_NC_2 = N(N-1)/2$ rotation. So, we can write ${}_NC_2$ parameter by rotation angle θ_i. Remaining parameter's are written by θ_j. On the other hand, the phases of the quark fields can be rotated freely, except an overall phase.

$$\begin{aligned} U \rightarrow F_U U &= \begin{bmatrix} e^{i\phi_u} & & & \\ & e^{i\phi_c} & & \\ & & e^{i\phi_t} & \\ & & & . \end{bmatrix} U \\ D \rightarrow F_D D &= \begin{bmatrix} e^{i\phi_d} & & & \\ & e^{i\phi_s} & & \\ & & e^{i\phi_s} & \\ & & & . \end{bmatrix} D. \end{aligned}$$

By these transformation,

$$V \rightarrow F_U^* V F_D.$$

That is,

$$V_{ij} \rightarrow \exp[-i(\phi_{uj} - \phi_{dk})] V_{jk}.$$

Finally, we can write V with $(N-1)(N-2)/2$ independent phases. Thus, if $N \leq 2$, we can write mixing matrix V with real, which means there are one angle (θ_C) and no phase. But, if $N \geq 3$ we can explain the effect of CP-violation. we can write the quark mixing matrix under the Standard Model, called "Cabibbo-Kobayashi-Maskawa(CKM) matrix", as following,

$$V = \begin{pmatrix} V_{ud} & V_{us} & V_{ub} \\ V_{cd} & V_{cs} & V_{cb} \\ V_{td} & V_{ts} & V_{tb} \end{pmatrix} = \begin{pmatrix} c_1 c_2 & s_1 c_1 & s_2 e^{-i\delta} \\ -s_1 c_3 - c_1 s_2 s_3 e^{-i\delta} & c_1 s_3 - s_1 s_2 s_3 e^{i\delta} & c_2 s_3 \\ -s_1 s_3 - c_1 s_2 c_3 e^{-i\delta} & c_1 c_3 - s_1 s_2 c_3 e^{i\delta} & c_2 s_3 \end{pmatrix} \tag{2.3}$$

where $c_i = \cos\theta_i$ and $s_i = \sin\theta_i$.

Wolfenstein expanded CKM matrix in powers of a small parameter $\lambda = \sin\theta_C = 0.22 = V_{us}$. By measurement of the lifetime of $B(\tau_B)$

$$V_{cb} \sim 0.06 = A\lambda^2, \tag{2.4}$$

and using following assumption,

$$\begin{aligned} A\lambda^2 &= (S_2^2 + s_3^2 + 2 s_2 s_3 \cos\delta)^{1/2} \\ A^2\lambda^4\eta &= s_2 s_3 \sin\delta \\ A\lambda^2(\rho^2+\eta^2)^{1/2} &= s_3 \ or \ A\lambda^2(\rho^2+\eta^2)^1/2 = s_2 \end{aligned}$$

where ρ and η a real parameters of order unity, we can write CKM in order λ^3 in Wolfenstein parametrization [6] as,

$$V = \begin{pmatrix} 1 - \frac{\lambda^2}{2} & \lambda & \lambda^3 A(\rho - i\eta) \\ -\lambda & 1 - \frac{\lambda^2}{2} & \lambda^2 A \\ \lambda^3 A(1 - \rho - i\eta) & -\lambda^2 A & 1 \end{pmatrix} + O\left(\lambda^4\right). \tag{2.5}$$

2.3.3 Unitarity triangle

If we consider the unitarity of the CKM matrix, we can obtain following relations,

$$\begin{aligned}
V_{ud}V_{cd}^* + V_{us}V_{cs}^* + V_{ub}V_{cb}^* &= 0 \\
V_{ud}V_{us}^* + V_{cd}V_{cs}^* + V_{td}V_{ts}^* &= 0 \\
V_{td}V_{cd}^* + V_{ts}V_{cs}^* + V_{tb}V_{cb}^* &= 0 \\
V_{us}V_{ub}^* + V_{cs}V_{cb}^* + V_{ts}V_{tb}^* &= 0 \\
V_{td}V_{ud}^* + V_{ts}V_{us}^* + V_{tb}V_{ub}^* &= 0 \\
V_{ud}V_{ub}^* + V_{cd}V_{cb}^* + V_{td}V_{tb}^* &= 0
\end{aligned}$$

And if we consider only complex phase, we use only following equation,

$$V_{td}V_{tb}^* + V_{cd}V_{cb}^* + V_{ud}V_{ub}^* = 0, \tag{2.6}$$

and use Wolfenstein parameters, $V_{ub}^* \approx 1, V_{cd} \approx -\lambda, V_{tb} \approx 1$, we can write equation 2.6 as

$$V_{ub}^* - \lambda V_{cb}^* + V_{td} = 0.$$

Figure 2.2 shows these unitarity triangle image.

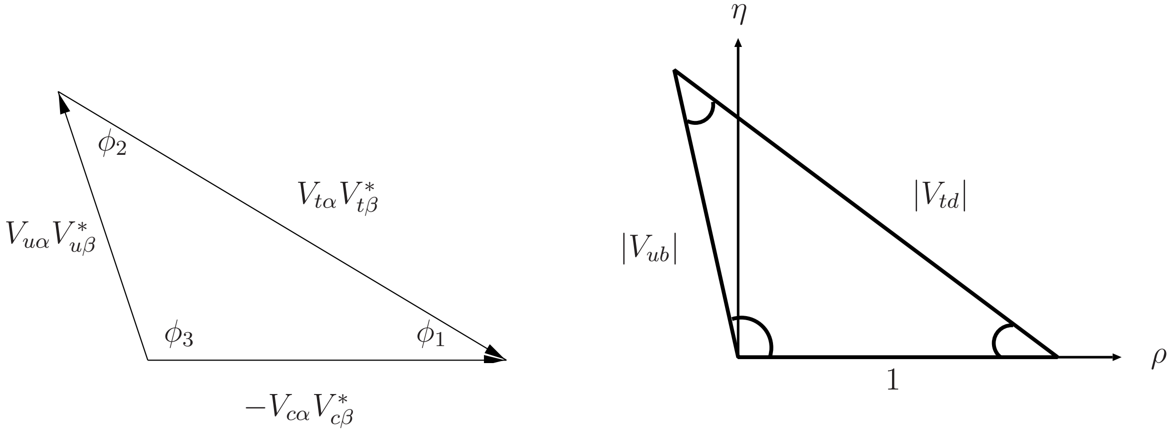

Figure 2.2: unitarity triangle; Left triangle is just unitarity triangle, right one is triangle with using Wolfenstein parameters.

$$\phi_1 \equiv arg\left(\frac{V_{cd}V_{cb}^*}{V_{td}V_{tb}^*}\right), \phi_2 \equiv arg\left(\frac{V_{ud}V_{ub}^*}{V_{td}V_{tb}^*}\right), \phi_3 \equiv arg\left(\frac{V_{cd}V_{cb}^*}{V_{ud}V_{ub}^*}\right). \tag{2.7}$$

$$\frac{V_{ub}}{V_{cd}} = 0.008 \pm 0.03\ ,\ \sqrt{\rho^2+\eta^2} < 0.36 \pm 0.14.$$

2.4 CP-violation in neutral B^0 meson system

We observe CP-violation in neutral $K^0, \bar{K^0}$ system. If we changed s quark to b quark, we can consider neutral $B^0, \bar{B}^0$ system. In this section, we discuss about CP-violation in neutral B^0 meson system. First we try to describe time-evolution of B^0. Second we consider $B \to f_{cp}$. Finally, we approach $B^0 \to J/\psi\ K_L^0$ decay and Kobayashi-Maskawa matrix parameter.

2.4.1 Time evolution of B^0

First, we consider the time-evolution of neutral B^0 meson system, only consider about $|B^0\rangle$. We can write $|\Psi_B(t)\rangle$ as linear combination of B^0 and $\bar{B}^0$, like neutral K system, shown in eq 2.8.

$$|\Psi_B(t)\rangle = a(t)|B^0\rangle + b(t)|\bar{B}^0\rangle \quad or \quad \sqrt{\Psi}_B(t) = \begin{pmatrix} a(t) \\ b(t) \end{pmatrix}$$

which is obtained from the time-dependent *Shrödinger* equation

$$i\frac{\partial}{\partial t}|\Psi_B(t)\rangle = \mathbf{H}|\Psi_B(t)\rangle \tag{2.8}$$

where $\mathbf{H} = \mathbf{M} - \frac{\mathbf{i}}{\mathbf{2}}\Gamma$, $\mathbf{M}$ is mass matirx and Γ is decay matrix. $\boldsymbol{M}$ and $\boldsymbol{\Gamma}$ are Hermitian,

$$M_{21} = M_{12}^* \ , \ \Gamma_{21} = \Gamma_{12}^*,$$

according to CPT invariance, we define M_{00} and Γ_{00} as,

$$M_{11} = M_{22} \equiv M_{00} \ , \ \Gamma_{11} = \Gamma_{22} \equiv \Gamma_{00}.$$

Then we can describe Hamiltonian $\mathbf{H}$ as,

$$\mathbf{H} = \begin{pmatrix} M_{00} - \frac{i}{2}\Gamma_{00} & M_{12} - \frac{i}{2}\Gamma_{12} \\ M_{12}^* - \frac{i}{2}\Gamma_{12}^* & M_{00} - \frac{i}{2}\Gamma_{00} \end{pmatrix}.$$

Eigenstates of this Hamiltonian is mass-eigenstate of particles. We define two mass-eigenstates as,

$$\begin{aligned} |B_H\rangle &= p|B^0\rangle + q|\bar{B}^0\rangle \\ |B_L\rangle &= p|B^0\rangle - q|\bar{B}^0\rangle \end{aligned}$$

where $p = \sqrt{M_{12} - \frac{i}{2}\Gamma_{12}}$, $q = \sqrt{M_{12}^* - \frac{i}{2}\Gamma_{12}^*}$. we can express time-evolution of mass eigenstate as

$$\begin{aligned} |B_H(t)\rangle &= e_H(t)|B_H(0)\rangle \\ |B_L(t)\rangle &= e_L(t)|B_L(0)\rangle \end{aligned}$$

where $e_\alpha(t) = e^{-im_\alpha t - \frac{\gamma_\alpha}{2}t}$. m_H and m_L are each mass-eigenstate value and γ_H and γ_L are each decay rate. then we obtain time-evolution of pure $|B^0(t)\rangle, |\bar{B}^0(t)\rangle$ state,

$$|B^0(t)\rangle = \left(\frac{e_H + e_L}{2}|B^0\rangle + \frac{e_H - e_L}{2}\frac{q}{p}|\bar{B}^0\rangle\right) \tag{2.9}$$

$$|\bar{B}^0(t)\rangle = \left(\frac{e_H + e_L}{2}|\bar{B}^0\rangle + \frac{e_H - e_L}{2}\frac{p}{q}|B^0\rangle\right) \tag{2.10}$$

here, using $\bar{m} = (m_H + m_L)/2$, $\delta m_d = m_H - m_L$, $\bar{\gamma} = (\gamma_H + \gamma_L)/2$, $\delta\gamma = \gamma_H - \gamma_L$, we can re-write $e_H \pm e_L$ term as,

$$\begin{aligned} e_H \pm e_L &= e^{im_H t - \frac{\gamma_H}{2}t} \pm e^{im_L t - \frac{\gamma_L}{2}t} \\ &= e^{i(\bar{m} - \frac{i}{2}\bar{\gamma})t}\left(e^{-i\cdot\frac{1}{2}(\delta m_d - \frac{i}{2}\delta\gamma)t} \pm e^{+i\cdot\frac{1}{2}(\delta m_d - \frac{i}{2}\delta\gamma)t}\right). \end{aligned}$$

In the B_d^0 meson system, $\delta\gamma/\gamma$ is much smaller than unity, because the difference is produces by common decay channels to B^0 and $\bar{B}^0$ with branching fractions of order 10^{-3} or less. Thus their term containing $\delta\gamma/\gamma$ is usually dropped out and $\bar{\gamma} = \gamma$. So we can write Equation (2.9) and (2.10) as

$$\begin{aligned} e_H \pm e_L &= e^{-i(\bar{m} - \frac{\gamma}{2})t}\left(e^{-i\frac{\delta m_d}{2}t} \pm e^{i\frac{\delta m_d}{2}t}\right) \\ e_H + e_L &= e^{-i(\bar{m} - \frac{\gamma}{2})t} \cdot 2\cos\frac{\delta m_d}{2}t \\ e_H - e_L &= e^{-i(\bar{m} - \frac{\gamma}{2})t} \cdot -2i\sin\frac{\delta m_d}{2}t \end{aligned}$$

therefore,

$$\begin{aligned} |B^0(t)\rangle &= e^{-i(\bar{m} - \frac{i}{2}\gamma)t}\left(\cos\frac{\delta m_d}{2}t|B^0\rangle - i\frac{q}{p}\sin\frac{\delta m_d}{2}t|\bar{B}^0\rangle\right) \\ |\bar{B}^0(t)\rangle &= e^{-i(\bar{m} - \frac{i}{2}\gamma)t}\left(\cos\frac{\delta m_d}{2}t|\bar{B}^0\rangle - i\frac{p}{q}\sin\frac{\delta m_d}{2}t|B^0\rangle\right). \end{aligned}$$

If pure B^0 exist at $t = 0$, $\bar{B}^0$ is mixed with time. It changes to pure $\bar{B}^0$ at $t = \pi/2\delta m_d$, and then it changes to pure B^0 at $t = \pi/\delta m_d$ again, and vice versa. This $B^0 - \bar{B}^0$ mixing-oscillation image ignoring decay by time ($e^{-i(\bar{m} - \frac{i}{2}\gamma)t}$) effect shown in Figure 2.3. This $B^0 - \bar{B}^0$ mixing-oscillation feynman diagram is shown in Figure 2.4.

2.4.2 B meson decay in to CP eigenstate

Next, we consider that initially pure B^0 or $\bar{B}^0$ decay into the CP-eigenstate, f_{CP} shown in Figure 2.5, $CP|f_{cp}\rangle = \pm|f_{cp}\rangle = \eta|f_{cp}\rangle$. Due to $B^0 - \bar{B}^0$ mixing, there are two decay channels,

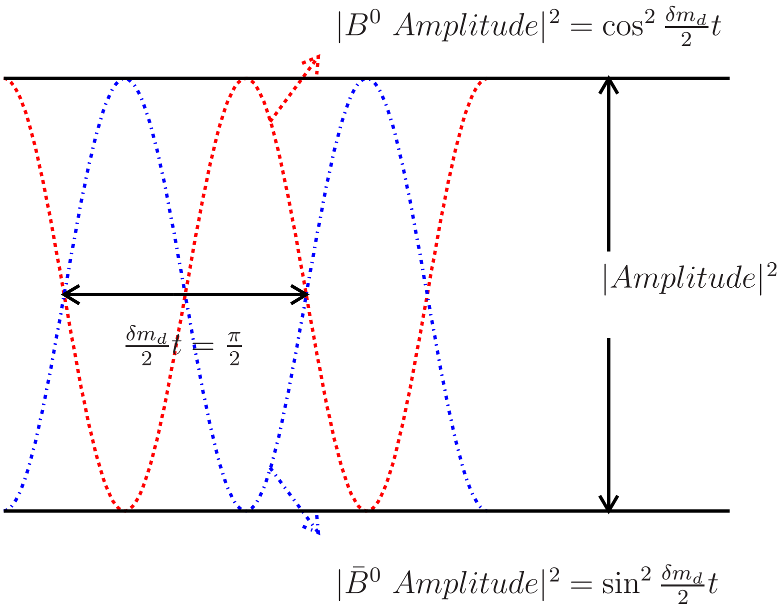

Figure 2.3: $B^0 - \bar{B}^0$ system time-evolution. Red (Blue) curve is existence of B^0 ($\bar{B}^0$). Top (Bottom) black line is pure B^0 ($\bar{B}^0$).

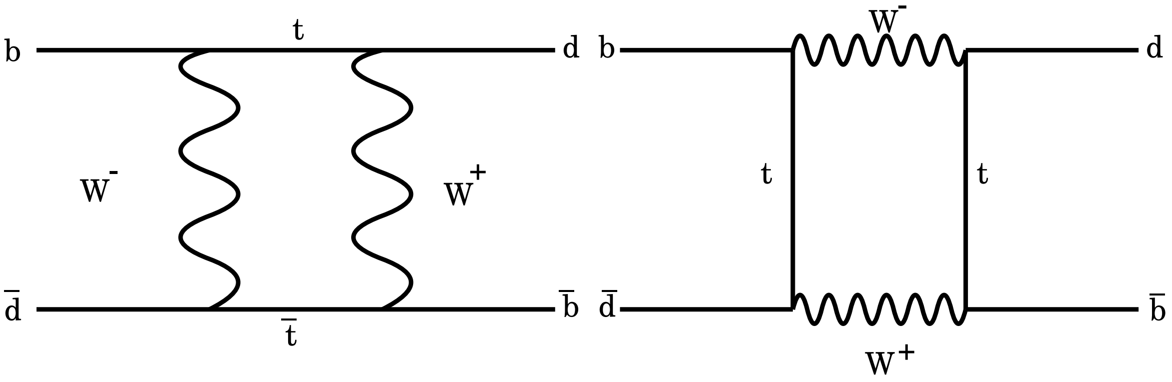

Figure 2.4: B^0- $\bar{B}^0$ mixing diagrams

$B^0 \rightarrow f_{cp}$ shown Figure 2.5 with blue solid line.
$\bar{B}^0 \rightarrow B^0 \rightarrow f_{cp}$ shown Figure 2.5 with red solid line.

$\bar{B}^0 \rightarrow f_{cp}$ shown Figure 2.5 with red dashed line.
$B^0 \rightarrow \bar{B}^0 \rightarrow f_{cp}$ shown Figure 2.5 with blue dashed line.

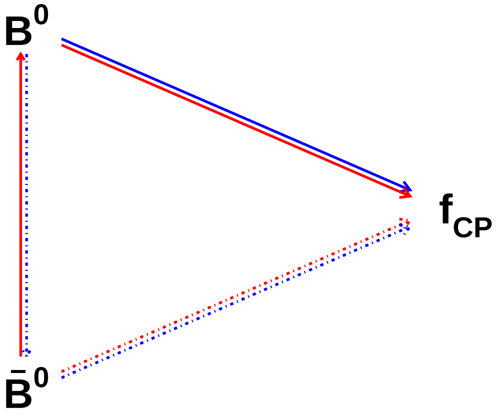

Figure 2.5: decay path into f_{cp}

We define the time-dependent CP-asymmetry as,

$$A_{cp}(t) \equiv \frac{\Gamma(\bar{B} \rightarrow f_{cp}) - \Gamma(B \rightarrow f_{cp})}{\Gamma(\bar{B} \rightarrow f_{cp}) + \Gamma(B \rightarrow f_{cp})}. \tag{2.11}$$

To obtain this asymmetry, first we calculate each time-dependent decay width using following decay amplitude,

$$A_f \equiv \langle f_{cp}|B^0\rangle \ , \ \bar{A}_f \equiv \langle f_{cp}|B^0\rangle.$$

For convenience, we use

$$\lambda \equiv \frac{q}{p}\frac{\bar{A}}{A}.$$

The time-dependent decay amplitude from Equation (2.9) and (2.10) following as,

$$\begin{aligned}
\langle f_{cp}|B^0(t)\rangle &= e^{i(\bar{m}-\frac{i}{2})t} A \left(\cos\frac{\delta m_d}{2}t - i\lambda \sin\frac{\delta m_d}{2}t\right) \\
\langle f_{cp}|\bar{B}^0(t)\rangle &= e^{i(\bar{m}-\frac{i}{2})t} A \left(\frac{p}{q}\right) \left(\lambda \cos\frac{\delta m_d}{2}t - i \sin\frac{\delta m_d}{2}t\right)
\end{aligned}$$

Thus we obtain the time-dependent decay width following,

$$\begin{aligned}
\Gamma(B^0(t) \to f_{cp}) &= |\langle f_{cp}|B^0(t)\rangle|^2 \\
&= |A_f|^2 e^{-\gamma t} \\
&\quad \times[\cos^2\frac{\delta m_d}{2}t - \Im(\lambda)\sin(\delta m_d t) + |\lambda|^2 \sin^2\frac{\delta m_d}{2}t] \quad (2.12) \\
\Gamma(\bar{B}^0(t) \to f_{cp}) &= |\langle f_{cp}|\bar{B}^0(t)\rangle|^2 \\
&= |\frac{p}{q}|^2 |A_f|^2 e^{-\gamma t} \\
&\quad \times[\sin^2\frac{\delta m_d}{2}t + \Im(\lambda)\sin(\delta m_d t) + |\lambda|^2 \cos^2\frac{\delta m_d}{2}t] \quad (2.13)
\end{aligned}$$

$|q/p| \approx 1$ is very good approximation in B^0 meson system. Therefore, we can write Equation (2.11) as

$$A_{cp}(t) = \frac{(|\lambda|^2 - 1)\cos(\delta m_d t) + 2\Im(\lambda)\sin(\delta m_d t)}{1 + |\lambda|^2}. \tag{2.14}$$

For neutral B meson system, CP-asymmetry is appeared if $\Im(\lambda) \neq 0$ or $|\lambda|^2 \neq 1$. $\Im(\lambda) \neq 0$ means that the phase in $B^0 - \bar{B}^0$ mixing is different from phase in the decay. This CP-violation is called *mixing − induced CP violation*. $|\lambda|^2 \neq 1$ means that the sizes of the decay amplitude are different. In other words, $|A_f| \neq |\bar{A}_f|$. This CP-violation is called *direct CP violation*. If there are two or more Feynman diagrams under weak interaction, *direct CP violation* is appeared. If their is one amplitude in the decay to the final CP-state, $|A_f| = |\bar{A}_f|$. then we can write Equation (2.14) as

$$A_{cp}(t) = \Im(\lambda)\sin(\delta m_d t). \tag{2.15}$$

2.4.3 CP-asymmetry in $B^0 \to J/\psi\ K_L^0$

In this thesis, we select f_{cp} as $B^0 \to J/\psi\ K_L^0$ decay. Figure 2.6 shows the Feynman diagram for this decay. In the B meson system, the contribution from penguin diagram is small. So, we can consider only tree diagram case and ignore penguin diagram phase.

In the KM mechanism, $\frac{\bar{A}_f}{A_f}$ is expressed with CKM matrix elements as,

$$\begin{aligned}
\frac{\bar{A}_f}{A_f} &= \frac{\bar{A}(B \to J/\psi\ K_L^0)}{A(B \to J/\psi\ K_L^0)} \\
&= \frac{V_{cb}V_{cs}^*}{V_{cb}^*V_{cs}}.
\end{aligned}$$

Next, we consider the term of q/p. If we have K^0 at the final states, we need add K^0 effect. This is because $K^0 - \bar{K}^0$-oscillation. So, we can express $(q/p)_{B\to J/\psi\ K_L^0}$

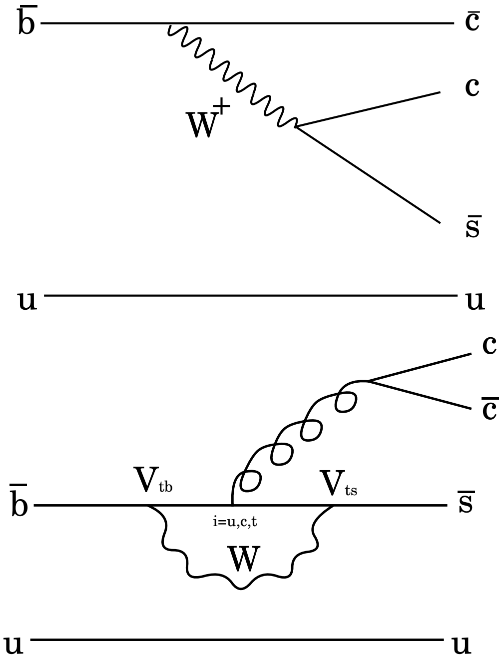

Figure 2.6: Fyenman diagram for $B^0 \rightarrow J/\psi\ K_L^0$. Upper (Lower) one is Tree (Penguin) diagram.

as,

$$\begin{aligned}\left(\frac{q}{p}\right)_{B\rightarrow J/\psi\ K_L^0} &= \left(\frac{q}{p}\right)_{B^0}\left(\frac{q}{p}\right)_{K^0} \\ &\approx \frac{V_{tb}^*V_{td}}{V_{tb}V_{td}^*}\frac{V_{cs}V_{cd}^*}{V_{cs}^*V_{cd}},\end{aligned}$$

therefore, we can express λ with CP-eigenstate value, η

$$\begin{aligned}\lambda_{B\rightarrow J/\psi\ K_L^0} &= \left(\frac{q}{p}\right)_{B\rightarrow J/\psi\ K_L^0}\frac{\bar{A}(B\rightarrow J/\psi\ K_L^0)}{A(B\rightarrow J/\psi\ K_L^0)} \\ &= \frac{V_{tb}^*V_{td}}{V_{tb}V_{td}^*}\frac{V_{cs}V_{cd}^*}{V_{cs}^*V_{cd}}\frac{V_{cb}V_{cs}^*}{V_{cb}^*V_{cs}} \\ &= \frac{V_{tb}^*V_{td}}{V_{cb}^*V_{cd}}\frac{V_{cb}V_{cd}^*}{V_{tb}V_{td}^*} \\ &= \eta\ e^{-2i\phi_1}. \qquad (2.16)\end{aligned}$$

Finally, we obtain CP-asymmetry parameter from Equation (2.15) as

$$A_{cp}(t) = -\eta\ \sin 2\phi_1 \cdot \sin(\delta m_d t). \qquad (2.17)$$

For $B^0 \to J/\psi\ K_L^0$ case η is $+1$. On the other hand, there is the CP-eigenstate event $B^0 \to J/\psi\ K_S^0$ which is called "Golden plate mode". This event's η is -1. So, In $B^0 \to J/\psi\ K_L^0$ case, we get same amplitude $\sin 2\phi_1$, but sign is opposite.

2.4.4 Δt distributions and time-dependent asymmetry

The decay rate for $(B^0\bar{B}^0)_{\Upsilon(4S)} \to J/\psi\ K_L^0(t_2), B^0(t_1)$, where one B meson decays into $B^0 \to J/\psi\ K_L^0$ at time t_2, and the other B meson is tagged as B^0 at time t_1, is expressed from Equation (2.12) and (2.16) as,

$$\Gamma((B^0\bar{B}^0)_{\Upsilon(4S)} \to B^0(t_1), J/\psi\ K_L^0(t_2)) \ \propto\ e^{\Gamma(t_1+t_1)}[1 - \eta \sin 2\phi_1 \sin \Delta m_d \Delta t].$$

On the other hand, the decay rate for $(B^0\bar{B}^0)_{\Upsilon(4S)} \to J/\psi\ K_L^0(t_2), \bar{B}^0(t_1)$, where one B meson decay into $B^0 \to J/\psi\ K_L^0$ at time t_2, and the other B meson is tagged as $\bar{B}^0$ at time t_1, is expressed from Equation (2.13) and (2.16) as,

$$\Gamma((B^0\bar{B}^0)_{\Upsilon(4S)} \to J/\psi\ K_L^0(t_2), \bar{B}^0(t_1)) \ \propto\ e^{\Gamma(t_1+t_1)}[1 + \eta \sin 2\phi_1 \sin \Delta m_d \Delta t]$$

where $\Delta t = t_2 - t_1$. The t_1 for the flavor-tag side and t_2 for the CP-eigenstate side are defined as t_{tag} and t_{CP}, respectively. In experiment, we can measure only Δt. This is because we do not know exact position where B meson pair are produced. The Δt values is in range from $-\infty$ to $+\infty$. These time evolutions calculated for $B^0 \to J/\psi\ K_L^0$ with $\sin 2\phi_1 = +0.7$ are shown in Figure 2.7. Equation (2.17) is described using Δt as,

$$A_{cp}(\Delta t) = -\eta\ \sin 2\phi_1 \cdot \sin(\Delta m_d \Delta t). \tag{2.18}$$

From Figure 2.7, the time-dependent CP-asymmetry is obtained as shown in Figure 2.8.

2.5 How to measure CP asymmetry in neutral B^0 meson system at Belle

The CP-asymmetry comes of depending on the decay time differrence between B^0-$\bar{B}^0$ meson pairs, but the asymmetry vanishes in the time integral rate. To measure CP-asymmetry, we need following necessarily things,

1 Asymmetric collider

2 Produce huge number of B

3 Good $B^0 \to J/\psi\ K_L^0$ reconstruction

4 Good decay vertex detection

5 Good flavor tagging system.

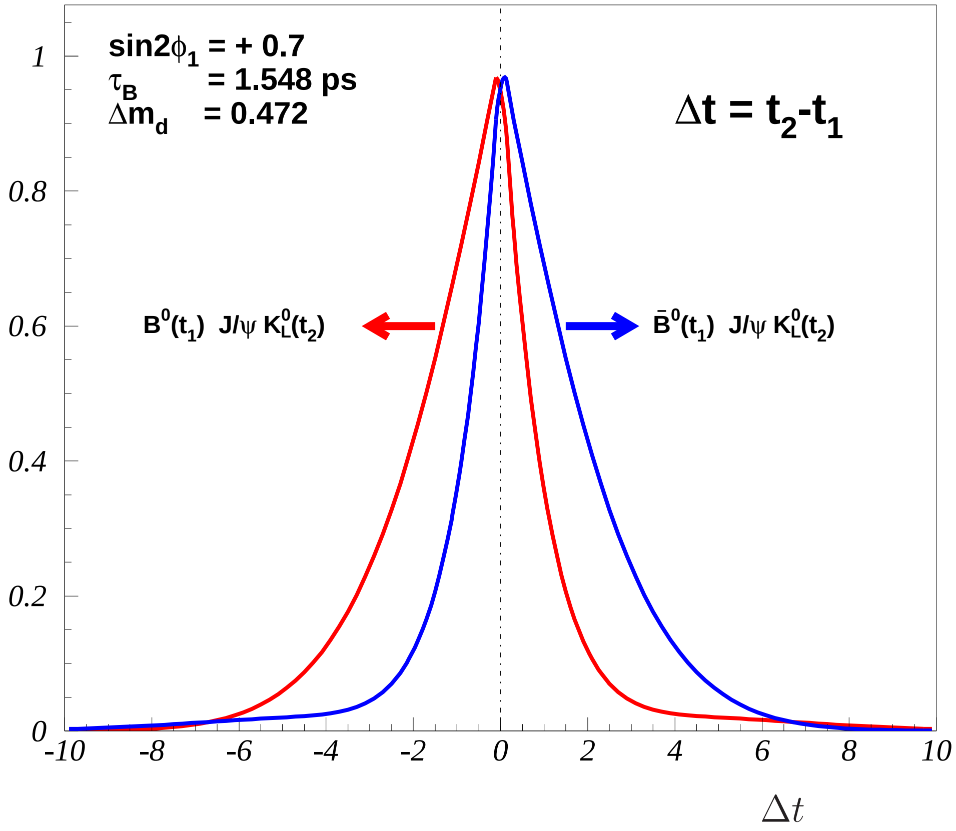

Figure 2.7: Expectation of proper time distribution with $B^0 \to J/\psi\ K_L^0$

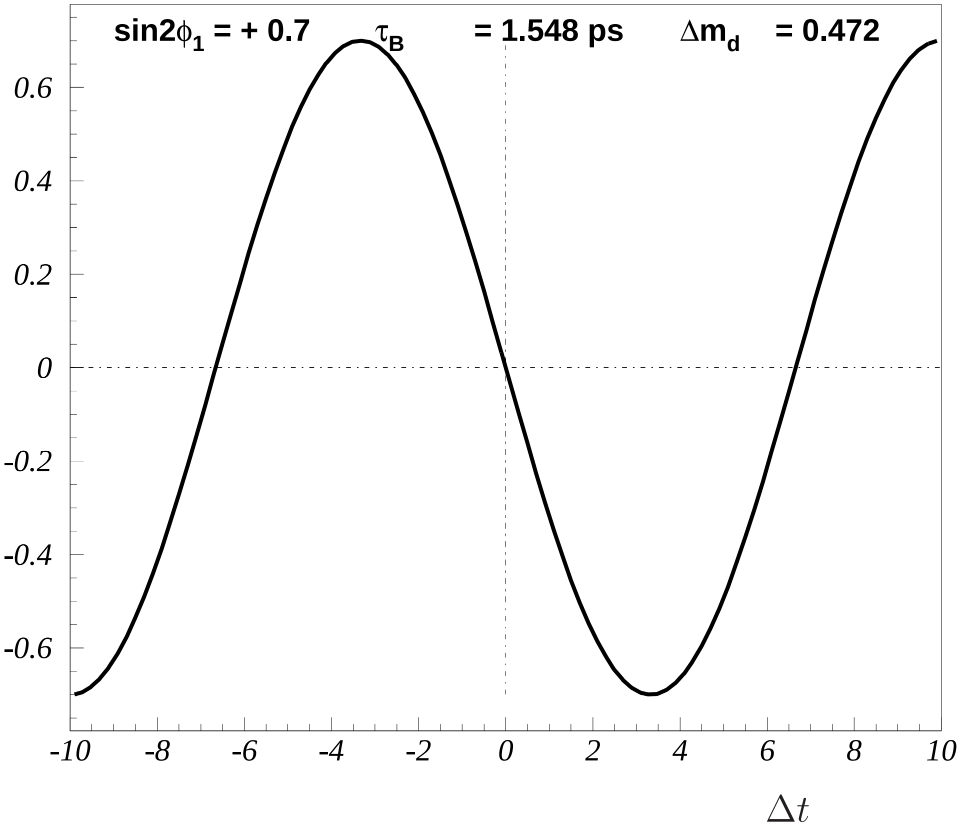

Figure 2.8: CP-asymmetry distribution with $B^0 \rightarrow J/\psi\ K_L^0$

2.5.1 Asymmetric collider

When we examin the CP-asymmetry, we need to measure the difference of decay time between B^0-$\bar{B}^0$ meson pairs. The difference is measured by moving B mesons in laboratory frame. To product such B meson pairs, we use an asymmetric e^+e^- collider with two rings, KEKB accelerator, described in Chapter 3 KEKB accelerator of having center-of-mass energy of 10.58 GeV, equal to the $\Upsilon(4S)$ mass. $\Upsilon(4S)$ decays only into B meson pairs.

2.5.2 Produce huge number of B

For the observation of time-dependent CP-asymmetry with good statistics, we need a lot of B^0-$\bar{B}^0$ meson pairs. The design luminosity of KEKB is $10^{34}/cm^2/sec$, which means that it is possible to product 100 million B meson pairs per year.

2.5.3 Good $B^0 \rightarrow J/\psi\ K_L^0$ reconstruction

When we reconstruct the event, we use many informations from sub-detectors at BELLE, shown in Chapter 3. In this thesis, we use $B^0 \rightarrow J/\psi\ K_L^0$ event as CP-eigenstate, so we need to reconstruct the B^0 and/or $\bar{B}^0$ event decaying into the CP-eigenstate with good quality, and we have to suppress background events in order to measure the correct CP-asymmetry, shown in Chapter 4.

2.5.4 Good decay vertex detection

The difference of decay time between B mesons is obtained by the difference between B^0 and $\bar{B}^0$ decay vertex points measured at a silicon vertex detector.

2.5.5 Good flavor tagging system

We need to determine the flavor of Bmeson decaying into CP-eigenstate to define the sign of the decay time difference. Therefore, we use flavor specific decay modes in B meson, shown in Chapter 5.

As mentioned above, experimentally necessary informations to measured the CP-asymmetry parameter are shown schematically in Figure 2.9.

2.5.6 Coordinate System

The Belle coordinate system is that the z axis is defined as anti-parallel to the positron beam direction, the x-axis is horizontally pointed out of the ring, and the y-axis is vertical direction. The Belle (x,y,z) coordinates are as follows (see Figure 2.10):

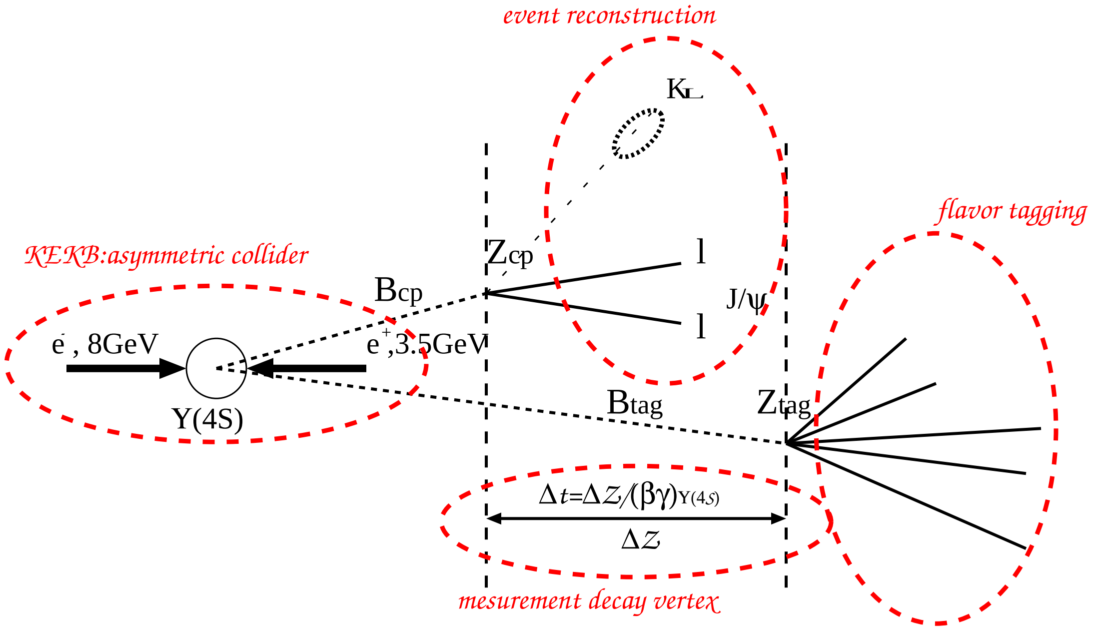

Figure 2.9: Experimental chematic picture of the time-dependent CP asymmetry measurement with $B^0 \to J/\psi\ K_L^0$

x : horizontal, outward to the KEKB ring
y : vertical, upward
z : opposite of the positron beam direction
r : $\sqrt{x^2 + y^2}$
θ : the polar angle from z axis
ϕ : the azimuth angle around z axis

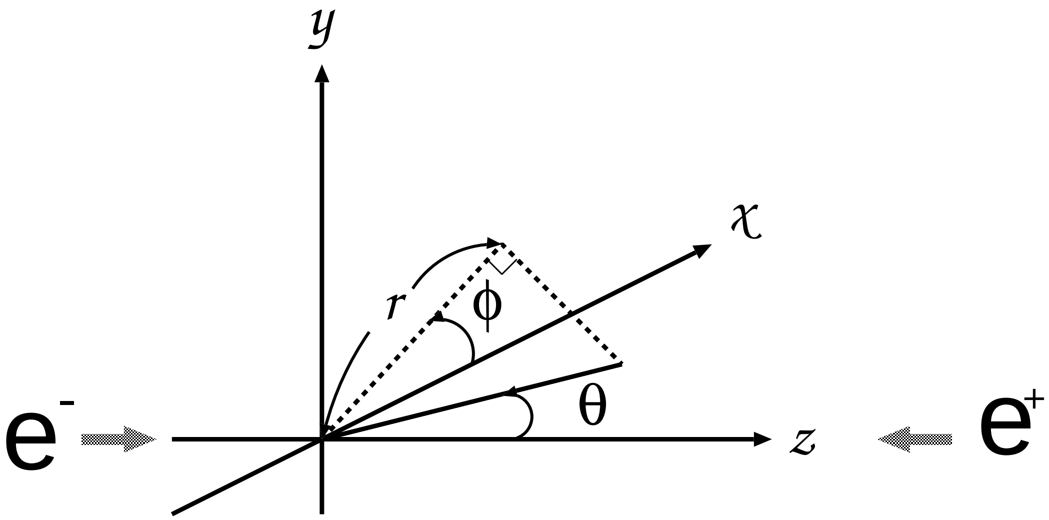

Figure 2.10: three-demantional coordinate

Chapter 3

B Factory

3.1 KEKB accelerator

KEKB accelerator, shown in Figure 3.1, is an asymmetric energy e^+e^- collider of about 3 km across, which consists of two storage rings for $E_{e^+} = 8.0\ GeV$ and $E_{e^-} = 3.5\ GeV$ and an injection linear accelerator for them. The center-of-mass energy is 10.58 GeV, which corresponds to the mass of $\Upsilon(4S)$ resonance. The Lorentz boost factor $\beta\gamma \simeq 0.425$ corresponds to the average distance of the two B meson decay vertices of approximately 200 μm.

The current peak luminosity is $= 1.05765 \times 10^{34}$, the highest achieved by any particle accelerator in the world. The integrated luminosity exceed 160 fb^{-1}. Figure 3.2 shows the daily and integrated luminosity record by Belle detector versus time. Figure 3.3 shows a typical beam current and luminosity for one-day. The detail discription of the KEKB accelarator is found in the refference [7].

3.2 Belle detector

Belle detector, shown in Figure 3.4, was designed for the precise study of B meson decays. The detector is roughly symmetric in ϕ with the positron beam as its symmetry axis, otherwise the electron beam comes in with 22 $mrad$ angle. The detector is asymmetrical to the forward and backward to maximize coverage of solid angle in the boosted center-of-mass (CMS) frame. Belle's combined detector coverage is between polar angles of 17° and 150°.

Belle's most inner detector is **S**ilicon **V**ertex **D**etector (SVD), which surrounds Beam pipe. It is used to measure the decay vertex of B mesons and other short-lifetime particles. **C**entral **D**rift **C**hamber (CDC), is used for charged particle tracking and momentum measurement, as well **P**article **I**dentification (**PID**) in the lower momentum range less than 1.0 GeV by ionization measurement (dE/dx). **A**erogel **C**herenkov **C**ounter (ACC), which made up of Cherenkov threshold counters located outside the CDC. It provides K/π separation in the momentum range 1.2 to

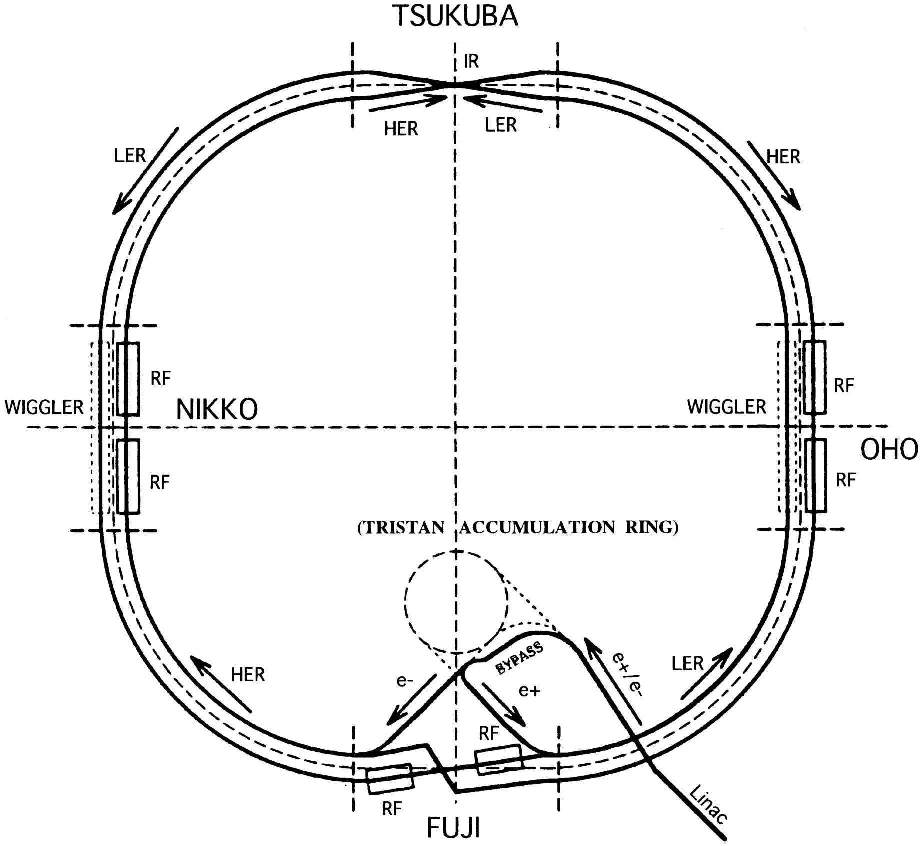

Figure 3.1: KEKB accelerator

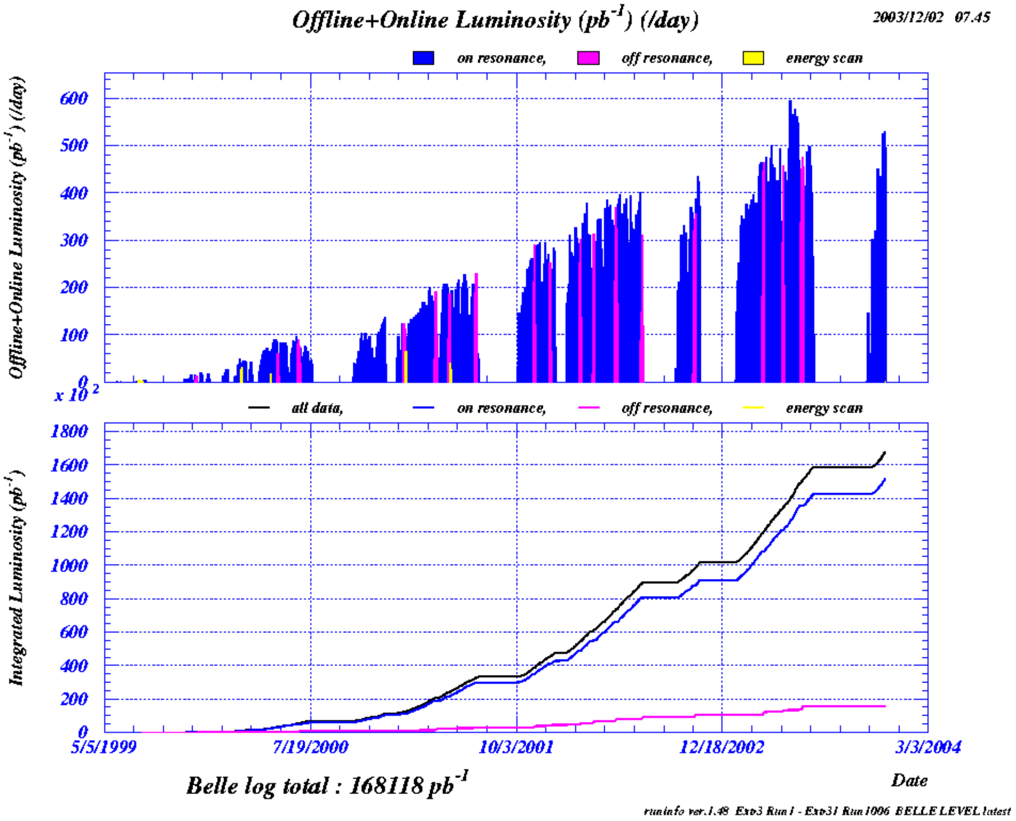

Figure 3.2: Upper (Lower) figure is KEKB daily (total) integrated luminosity, recorded by Belle

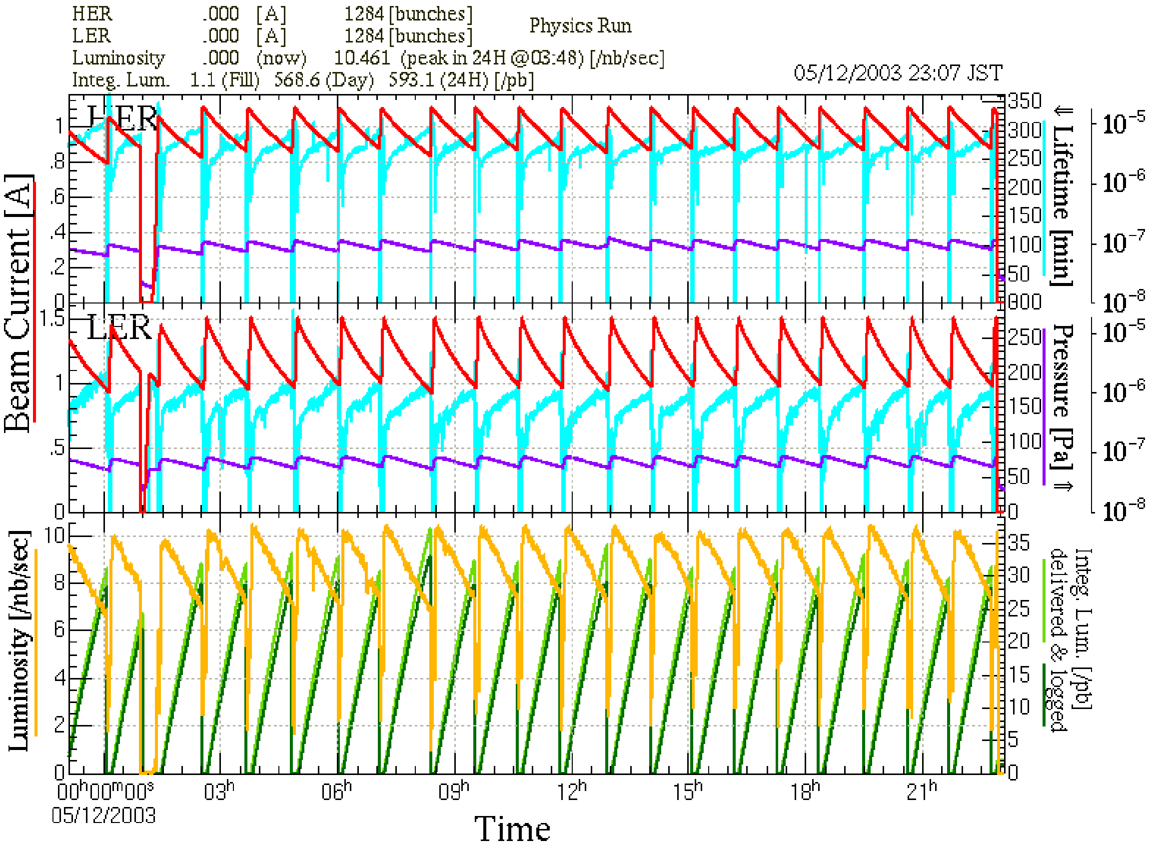

Figure 3.3: One day luminosity figure. top (middle) figure is HER (LER) information. bottom figure is luminosity status. we can see over $10/nb/sec$.

parameters	LER	HER	unit
Circumference	3018		m
Luminosity	$1 \times 10^{34}(2 \times 10^{33})\mathrm{cm}^{-2}\mathrm{sec}^{-1}$		$cm^{-2}s^{-1}$
particle	election	positron	
Crossing angle θ_x	11		mrad
Number of bunches	1281		
Bunch current	1.17	0.884	mA
Bunch spacing	2.4		m
Bunch trains	1		
Total RF coltage V_C	8.0	15.0	MV
Synchrotron tune V_s	-0.0249	-0.0225	
Betatron tune ν_x/ν_y	45.506/43.551	44.514/41.576	
beta's at IP β_x^*/β_y^*	59/0.58	58/0.7	cm
Estimated vertical beam size at IP σ_y^*	2.4	2.4	μm
beam-beam parameters ξ_x/ξ_y	0.104/0.0068	0.071/0.051	
Beam lifetime	125@1503	216@1132	min.@mA
Luminosity(Belle CsI)	11.305		$10^{33}/cm^2/sec$
Luminosity records per day / 7days / month	640/4240/12760		$/pb$
Energy	8.0	3.5	GeV
Beam Current	1.1	2.6	A

Table 3.1: Machine Parameters of the KEKB (Dec. 18 2003)

3.5 GeV/c. **T**ime **O**f **F**light detector (TOF), which is located in barrel region only, provides additional K/π separation in the momentum range less than 1.2 GeV/c, where the difference in flight-time between K and π can be resolved. **E**lectomagnetic **C**a**L**orimeter (ECL), which is used to detect photons and identify electrons by electromagnetic showers. These four detector are inside the magnet. The solecoidal superconducting magnet coil provides 1.5 T magnetic field parallel to the beam axis. Out side of the magnet, iron layers making up the magnet's flux return are interspersed with resistive plate chambers that form K_L and μ detection detector (KLM). Some of the otherwise uncovered forward and backward polar angle region is covered by the extreme forward calorimeter (EFC).

We will describe more explanation for each detector, giving a brief description of the physical layout, the main physics principle used in detection, and the performance of each. The readout electronics will in general not be discussed. The detail description of the Belle detector is in the refference [8].

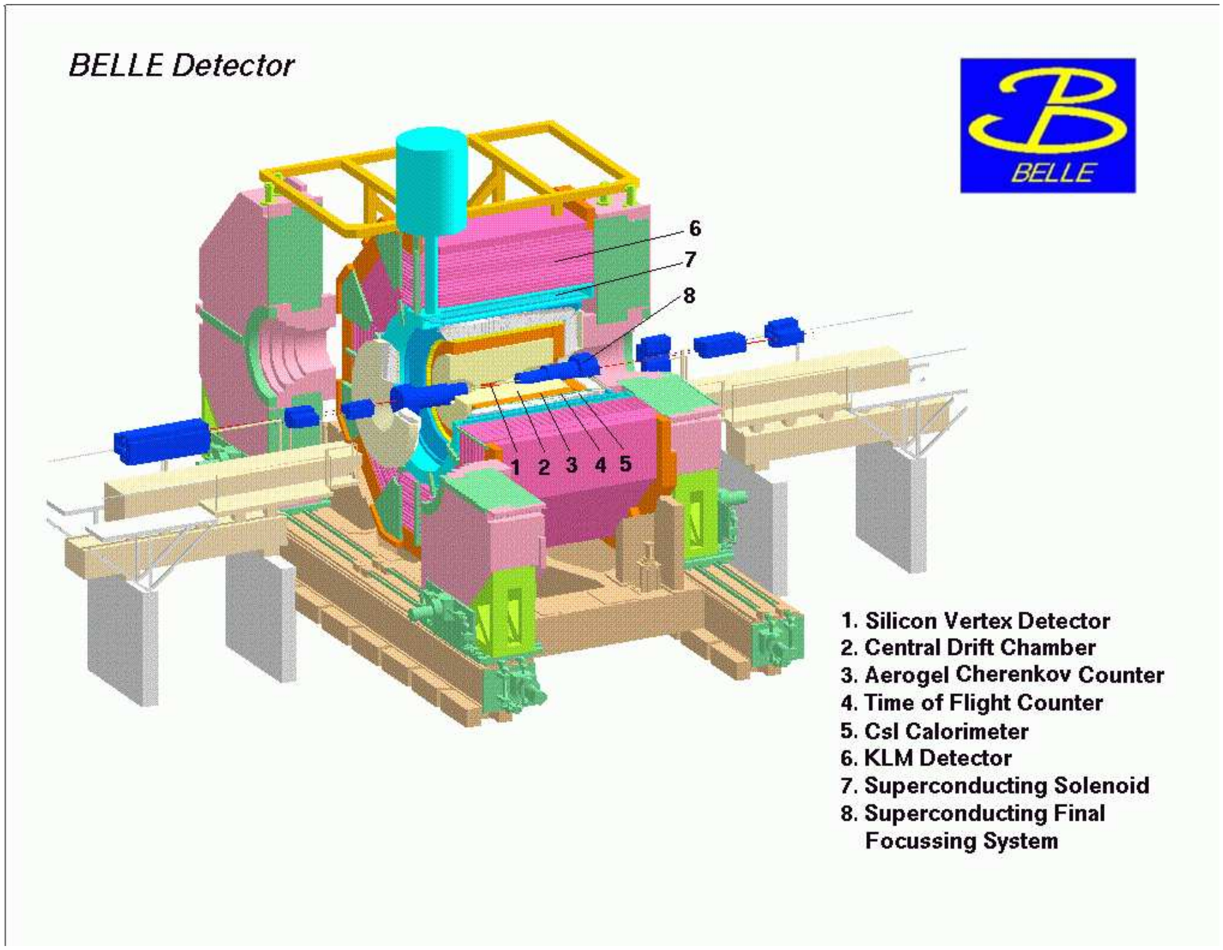

Figure 3.4: BELLE detector system

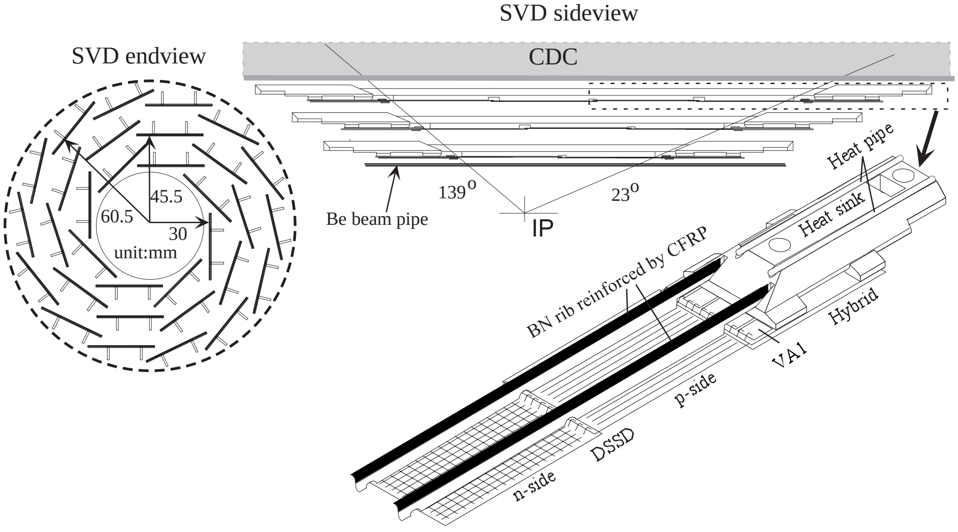

Figure 3.5: SVD

3.2.1 Beam pipe & SVD

SVD provide decay vertex information, trigger information, and helps tracking. SVD is very important detector in measurement of time dependent CP-asymmetries, which involve determining the Δz, which means vertex difference of B meson pairs, which resolution is on the order of 100 μm. SVD is also used to measure the decay vertices of other particles with comparable lifetimes, such as D mesons and τ leptons.

Due to their short-lifetime and low transverse momentum, B mesons from $\Upsilon(4S)$ decays at Belle typically only travel transverse distances of ≈ 30 μm, and decay inside the beam pipe. However the position of the decay vertices can be reconstructed from the B's charged decay products that move outside the beam pipe, and leave tracks in CDC, and hits in SVD. These tracks are extrapolated from CDC back-into SVD, where SVD hits are grouped into clusters, and associated with the different tracks. Since most B decay products of interest are in the momentum range of 1 GeV/c or lower, the vertex resolution is limited mainly by multiple coulomb scattering in any material that particles traverse before detection into SVD. For this reason, the thickness and density of beam pipe have been minimized, as well as the mass of SVD and its support structure. As the vertex resolution reduces with the distance to the first detection layer ($\sigma_z \propto r$), we want to close the first SVD layer as possible as to beam pipe. Consequently, the designs of Beam pipe and SVD are interrelated. The current beam pipe is a double-walled cylinder, with both the inner and outer walls made out of 0.5 mm beryllium. The inner and outer walls have radius of 20 and 23.5 mm, respectively. Beam pipe is cooled by flowing helium gas in the gap between the two walls. SVD detector is located around the beam pipe, shown in Figure 3.5. It consists of 102 double sided silicon strip detectors (DSSDs), distributed over three cylindrical layers, which surround the beam pipe at radial distances of 30, 35.5 and 60.6 mm, and cover the polar angle region $23° < \theta < 139°$. The DSSDs have sense strips on both sides. The strips on one side run in the z direction, while those on the other side are oriented in the r/ϕ direction. The former are called ϕ strips, and their pitch is 25 μm, but only every second one is read out, while the latter on one side are highly n doped, strips on the other side highly p doped. Abias voltage, typically 80 V, is applied to create a depletion region in the lower doped, 300 μm thick substrate between the strips. The particular DSSDs used, Hamamatsu S6936, wre originally developed for the DELPHI micro-vertex detector, and a more detail description of the DSSDs can be found in the NIM paper on that detector [9].

Charged particles traversing a DSSD ionize atoms in the depleted substrate, typically creating about 200000 electron-hole pairs. In the depletion region, electron and hole mobility is high, and the subsequent motion of the ionization charged can be read out by the induced image charge on the sense strips. Since this signal will appear only on a few z and ϕ strips, and the radius of the ladder is known, three-dimensional (3D) hits information is thus obtained. The (image) charge is collected by a charged-integrating amplifier. After integration and shaping, the signal is digitized and fed into a clustering algorithm. The probability that a CDC track (excluding K_s's) within the SVD acceptance is associated with SVD clusters in two layers in higher than 98 %. The momentum dependence of the impact parameter resolution is well described by $\theta_{xy} = 19 \oplus 50/(p\beta sin^{3/2}\theta)\mu m$ and $\theta = 36 \oplus 42(p\beta sin^{3/2}\theta)\mu m$, where $\oplus$ denotes addition in quadrature, and the first and second terms are due to detector resolution and multiple scattering, respectively. Additional details on the SVD's performance can be found in [10].

3.2.2 Central drift chamber (CDC)

CDC reconstructs and measure precise momentum of charged tracks. CDC also provides trigger information, and is take part of **PID** information by measuring dE/dx from ionization.

CDC geometry is shown in Figure 3.6. The cylindrical design provides coverage in the polar angle region $17° < \theta < 150°$. CDC has three cathode strip layers, and 50 cylindrical wire layers, each consisting of three to six sub layers with radial or stereo wires. The wires add up to 8400 drift cells. The inner-most and outer-most stereo layers, together with the cathode strips, provide fast z-trigger information. CDC is filled with a 50 % helium and 50 % ethane gas mixture, at a pressure slightly above one atmospheric pressure.

The cell structure of the CDC is shown in Figure 3.7. Sense wires of gold plated tungsten with 30 μm radius, and field wires of unplated aluminum with 126 μm radius, are used set up an electric field. A positive high voltage, $\approx$ 2.35 kV, is used for the sense wires, while the filed wires and endplates of the drift chamber are kept near ground potential. The voltage on individual sense wires varies somewhat, to keep the gas gain at the same value, roughly 10^4, for different cell sizes.

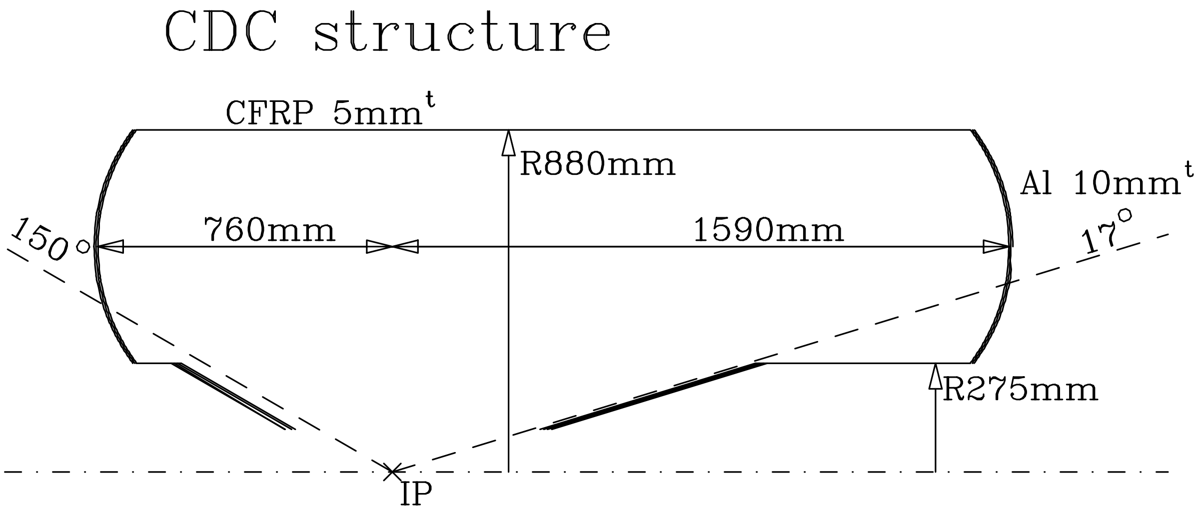

Figure 3.6: CDC

The helium-ethane mixture has low atomic number, which minimize3s multiple scattering. Charged tracks passing through the drift chamber ionize gas molecules along their path. The ionized electrons drift forwards the sense wires, at a velocity which saturates at $\approx\ 4\ cm/\mu s$, and depends relatively weakly on the electric field strength. Only when the electron come very close to the sense wires, does their energy become large enough to liberate fresh ions, creating an ionization avalanche with total charge proportional to the gas gain and the amount of primary ionization. The typical charge of this avalanche is thus large enough that when the liberated electrons subsequently drift toward the sense wire, the separation of positive ions and electrons produces a detectable image charge on the sense wires. Both the pulse time and the integrated charge of this signal is read out and used.

The timing ultimately provides position information. Since the drift velocity is roughly constant, the time interval between the event trigger and the sense wire signal, the "drift time" constrains the position of the original ionization seed to lie on a cylinder around the sense wire, with the radius of the cylinder proportional to the drift time. By combining the information from many sense wires, the trajectory in the $x-y$ plane can be reconstructed. Stereo wires, which run at a small angle with respect to the other wires in the chamber, provide additional z information. The curvature of the track's $x-y$ plane projection in the 1.5 T magnetic field, is used to measure the transverse momentum of the track, as explained in the section on the superconduction magnet, below.

The time integrated charge of the pulse can be used for *PID*. The most probable amount of ionization charge depends on the passing particles's velocity, $\beta = v/c$, as

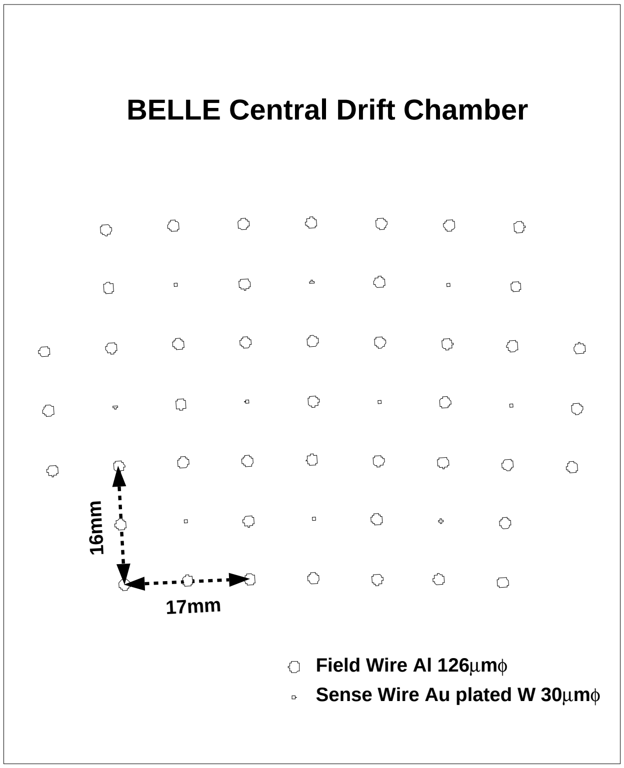

Figure 3.7: CDC cell structure

given by the Bethe-Bloch formula:

$$-dE/dx = \frac{4\pi N_0 z^2 e^4}{mv^2}\frac{Z}{A}\left[\ln\left(\frac{2mv^2}{I(1-\beta^2)}\right) - \beta^2\right] \tag{3.1}$$

where m is the electron mass, z and v are the charge and velocity of the particle, e is the electron charge, N_0 is Avogadro's number, Z and A are the atomic number and mass number of the atoms of the gas, x is the path length measured in kg/m^2, while I is an effective ionization potential, roughly 10 $Z\ eV$. For low velocities of the incident particle, dE/dx varies as $1v^2$, while in the ultrarelativistic regime, it increases logarithmically as $\ln\gamma$, where $\gamma = (1-\beta^2)^{1/2}$.

The dE/dx measurement is achieved by taking the mean of the ionization charge picked up by the various sense wires along the particle trajectory. Since the ionization charge depends on the particle velocity, and we measure momentum independently (from the trajectory's curvature), dE/dx information helps with PID in the low momentum region, where particles of different masses have a significant difference in velocity at the same momentum. Figure 3.8 shows a scatter plot of dE/dx versus particle momentum, measured in collision data. The different particle series clearly leave different distributions.

Using cosmic rays, the CDC transverse momentum resolution is measured to be $\approx 0.20p_t\% \oplus 0.29/\beta\%$, where p_t is the transverse momentum measured in GeV/c, the first term is due to detector resolution, and the second due is to multiple scattering. The dE/dx resolution is $6-8\%$, with the better value for μ pair and Bhabha data, the worse for $K_S^0 \to \pi^+\pi^-$. Spatial resolution of the tracking is about 130 μm. Additional details on the CDC and its performance can be found in [11].

3.2.3 Aerogel cherenkov counter system (ACC)

ACC is Belle's main means of π/K separation in the higher momentum ranges, which are not well covered by th TOF system, or dE/dx measurement in the CDC, as shown in Figure 3.16. The ACC consists of counter modules situated outside the CDC : 960 module in the barrel and 228 in the forward endcap, as shown in Figure 3.9 and 3.10.

The modules, shown in Figure 3.11, each consist of an aluminum box filled with five stacked aerogel tiles, where aerogel is a silicon based, noncrystaline solid, with very low density. One or two fine mesh photo-multipliers (FM-PMTs) are attached directly to the aerogel at the sides of the box to collect the Cherenkov light, emitted by particles traversing the aerogel.

In general, charged particles traversing a medium will emit a cone of Cherenkov radiation, if the particle's velocity, $\beta = v/c$, exceeds the velocity of light in the medium, $c\prime = c/n$. The half angle of the Cherenkov cone, θ_c, will in that case be given by

$$\cos\theta_c = \frac{1}{n\beta} = \frac{1}{n}\sqrt{1+\left(\frac{m}{p}\right)^2}. \tag{3.2}$$

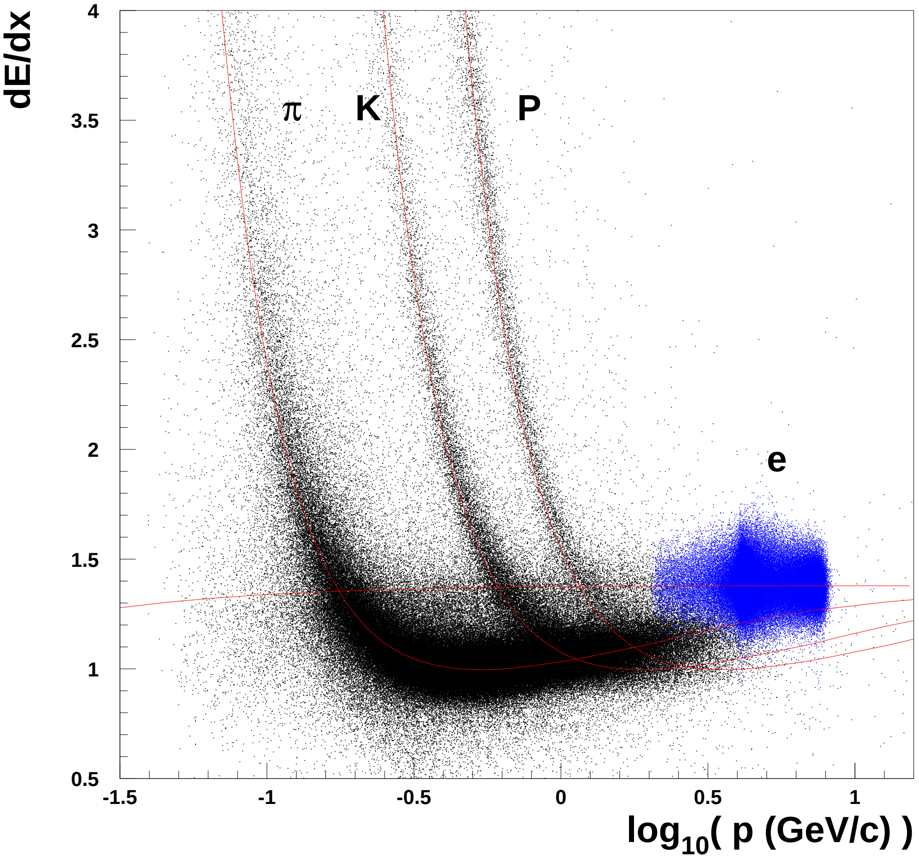

Figure 3.8: Measured mean of dE/dx versus momentum for different particle species. The curves show the expected mean energy loss.

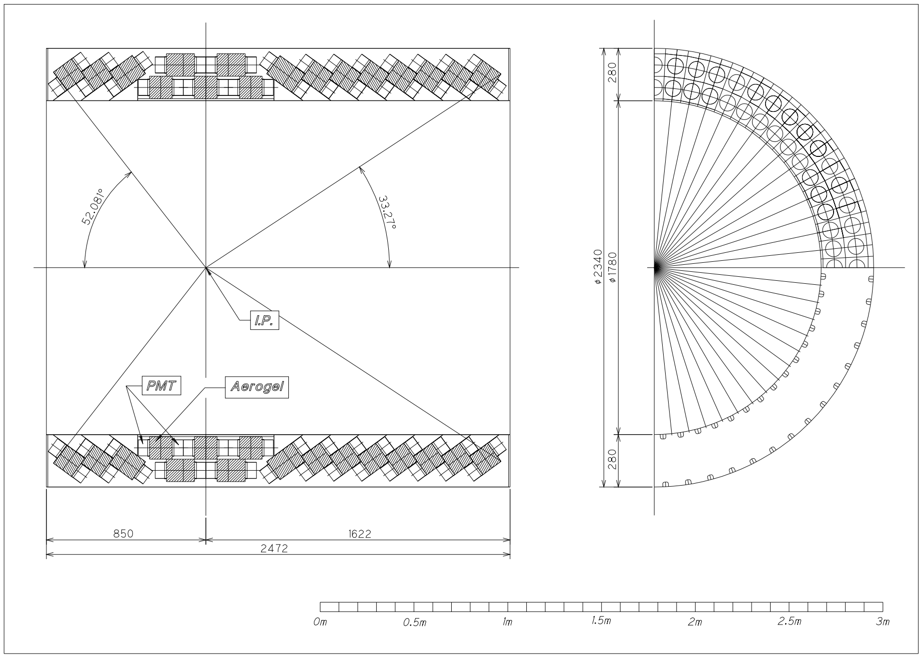

Figure 3.9: ACC Barrel part

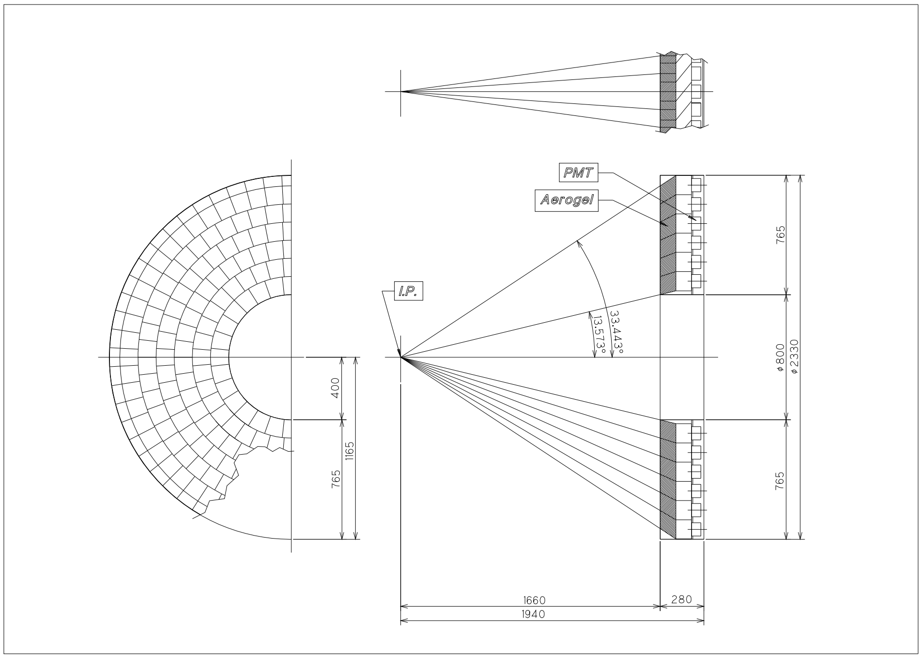

Figure 3.10: ACC Endcap part

a) Barrel ACC Module

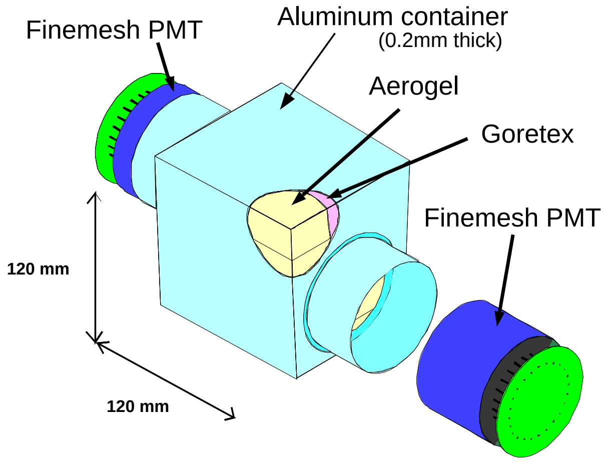

b) Endcap ACC Module

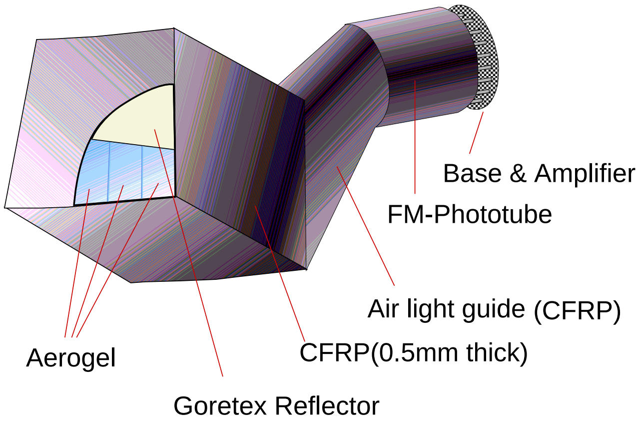

Figure 3.11: ACC modules

For particle of unit charge, the number of Cherenkov photons emitted per unit path length of the particle and per unit energy interval of the photons is approximately

$$\frac{d^2N}{dEdx} = 370 \sin^2 \theta_c / eV/cm. \tag{3.3}$$

The Belle ACC is a threshold device, which discriminates between particles of different masses, based on whether the ACC fires or not, but doesn't make use of cone-angle information. If the index of refraction of the Cherenkov device is chosen appropriately, then at a given momentum, the lighter particle will fire the counter, while the heavier particle will move too slowly Togo so. Including experimental limitations such as geometrical acceptance and quantum efficiency of the photo tubes, the Belle ACC is able to detect between 10 and 30 photons per particle above threshold (tested with muons), enough to provide good π/K separation up to 3.5 GeV/c.

One advantage of aerogel is that its index of refraction can be varied in the production process. Due to the asymmetric KEKB beams, final state particles emitted at small polar angle and to have larger momenta than those at large polar angles. Hence, as shown Figure 3.11, the refraction index of the aerogel used in the various ACC counters is varied with polar angle, to allow optimum separation of pions and kaons at all angles. The counters in the forward endcap have instead been optimized for flavor-tagging (see Section 5.1) by kaons. This involves identifying low-momentum kaons, typically below 1.5 GeV/c, resulting from cascade decay of B_d^0 mesons by the quark level transition $b \to c \to s$. More details regarding the ACC can be found in [12].

3.2.4 Time of flight system (TOF)

TOF provides π/K separation in the lower momentum region. It is also the subsystem that can deliver the most accurate timing of changed particles, and thus provides fast trigger information and timing signals to other subsystems.

The TOF system consists of 64 modules, each constraining two ϕ - adjacent TOF counters, separated by a 1.5 cm radial gap from a trigger scintillation counter (TSC), as shown in Figure 3.12. The TOF counters consist of 255 × 6 × 4 cm slabs of "Bicron BC408" plastic scintillator, and are read out on both ends with photo tubes, while the TSC is made out of Bicron BC412 and read out only on one end. The modules are located at a 1.2 m radius, outside the ACC in the detector barrel, as shown in Figure 3.15. The TSCs were added to the design to keep the fast trigger rate below the pile up limit of $70kHz$ in the presence of beam background. Due to the 1.5 T magnetic field in this region, the 1.5 cm gap between the TOF and TSC counters reduces backgrounds from electron-positron pairs created in the TSC, when the coincidence signal between the TOF and TSC counters is used.

A charged particle traversing a scintillation counter will excite molecules in its path, resulting in the subsequent emission of scintillation photons. In the case of

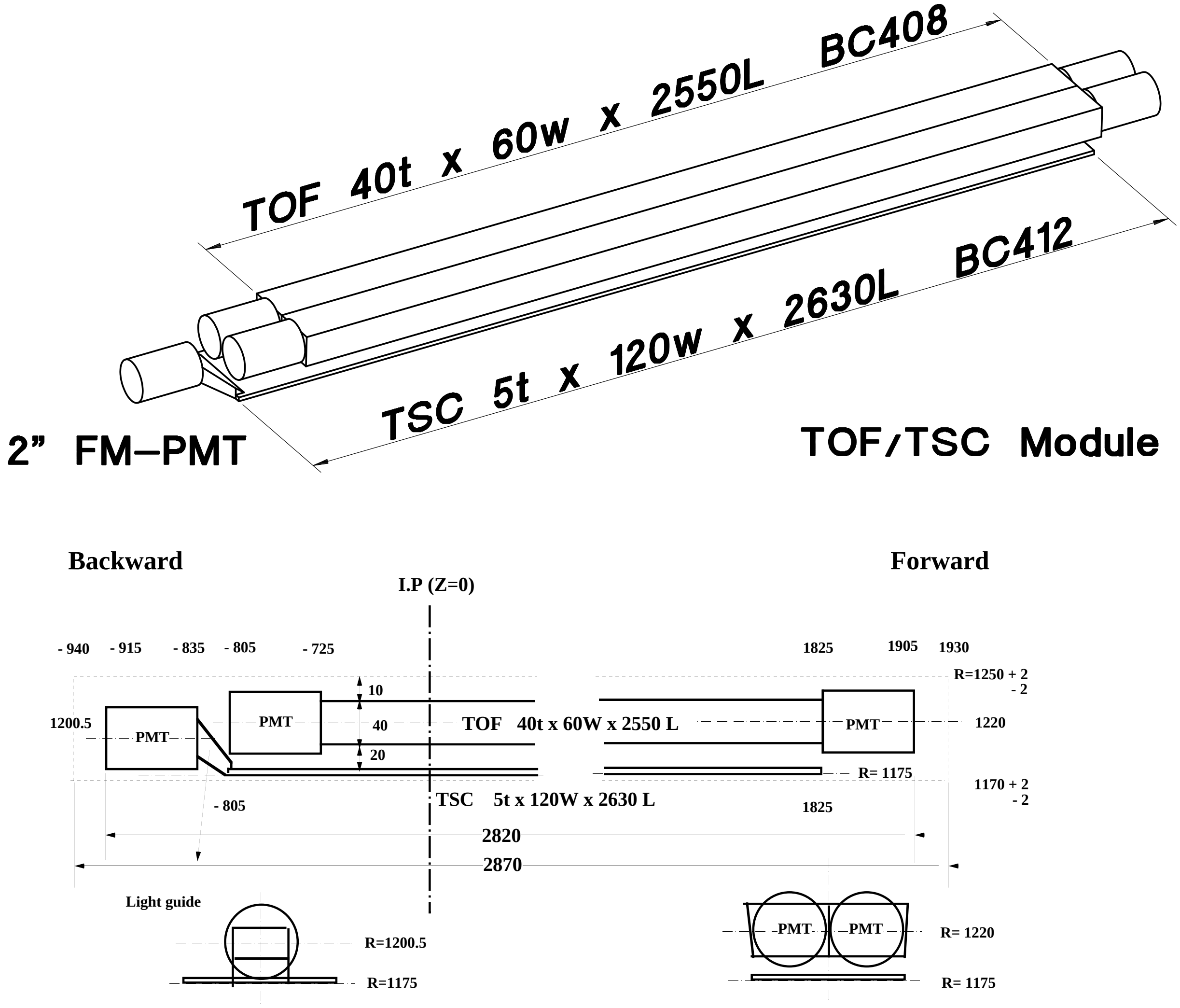

Figure 3.12: TOF/TSC

pure organic / plastic scintillator, the scintillation photons would be in the ultraviolet, where attenuation lengths are short, on the order of millimeters [13]. This situation is circumvented by combining the scintillator with fluorescent molecules, which frequency shift the scintillation radiation to the visible, where the material is more transparet. The visible photons from the flours then travel by internal reflection inside the scintillation counter, until they are read out with PMTs at the ends. Plastic scintillators are fast, with decay times on the order of nanoseconds, and even faster rise times.

In order to achieve good time resolution for the time - of - flight measurement, PMTs are mounted directly on the scintillator without intermediate light duides, which would have reduces the timing accuracy, due to dispersion and transit time variations of the detected photons. This puts the PMTs inside the 1.5 T magnetic field region. For this reason we use fine mesh PMTs, which are less sensitive to magnetic fields than standard PMTs. Since the timing accuracy increases with the number of photons detected ($\sigma_t \propto 1/\sqrt{N}$), it is also important to use scintillators with large attenuation length, compared to the maximum photo path length, as well as large-area PMTs, resulting in good photon-collection efficiency.

Figure 3.13 shows the time resolution obtained for muon tracks from μ - pair events, as a function of z. The time resolution of the forward PMT, backward PMT, and of the weighted average are shown. The weighted average time resolution is about 100 ps or better for all values of z.

Figure 3.14 and 3.14 demonstrates the TOF performance for hadronic events. Figure 3.14 plot shows the distribution of (the absolute value of) calculated mass, which is calculated using tracks' path length and momentum as measured by the CDC, and the measured time-of-flight. Only tacks with momentum below 1.3 GeV/c have been used. The measurements are shown as data points, while the Monte Carlo expectation, assuming a time resolution of 100 ps, has been superimposed as a solid histogram. Clear peaks for different hadron species can be seen, and the Monte Carlo agrees reasonably well with the data.

Figure 3.14 plot shows the TOF system's π/K separation power calculated using the equation on the figure, where μ_π and μ_K are the average flight time measured for π and K, respectively, at a given momentum, while the θ's are the uncertainties of these measurements. Thus the TOF achieves π/K separation $> 2\sigma$ for particle momenta up to 1.25 GeV/c.

3.2.5 K/π separation, PID

To separate Kaon and pion is very important for flavor-tagging in measurement of CP-violation, and also reconstruct and study of events which are $B \to \pi\pi$ ($\sin 2\phi_2$), $B \to KK/K\pi$. K/π separation at Belle [16] is designed to cover whole momentum region, based on energy loss in the CDC, time-of-flight by the TOF, and response of the ACC. We combine the information from these three subdetectors to realize more than 3σ separation between kaons and pions momentum from $0 \sim 3.5$ GeV/c,

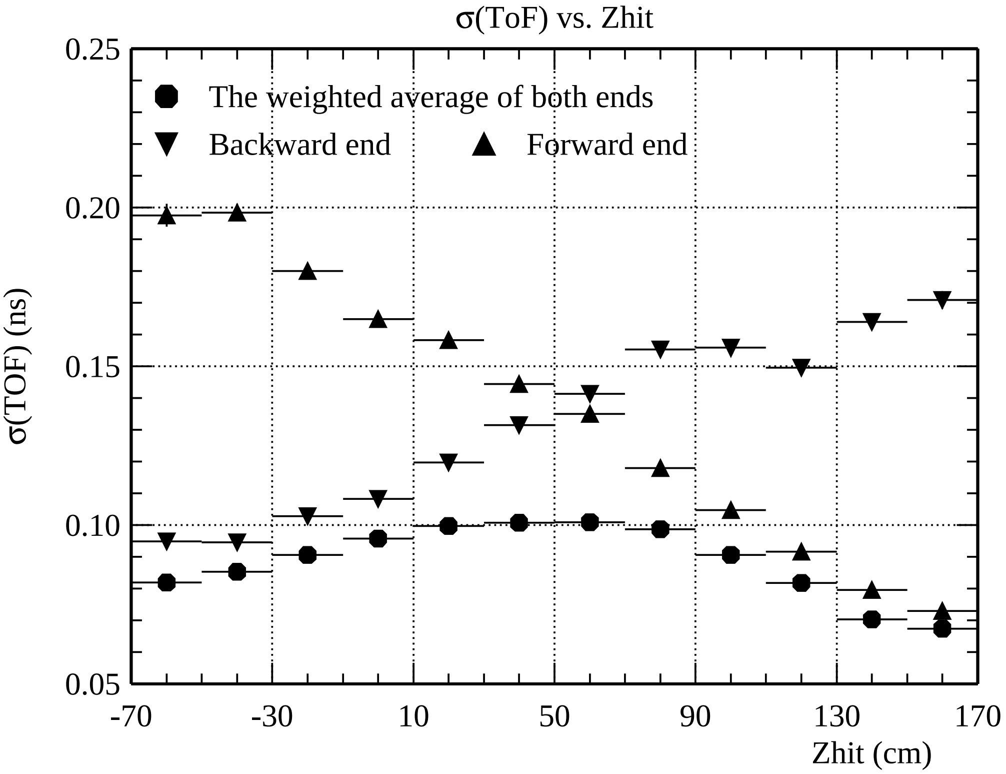

Figure 3.13: Time resolution for μ-pair events by TOF.

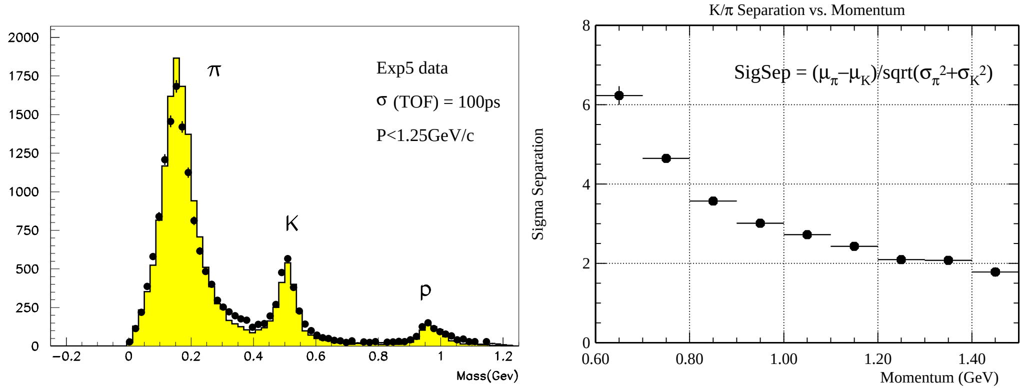

Figure 3.14: Distributions of hadron mass calculated from **TOF** and particles momemtun is less than 1.25 GeV/c.

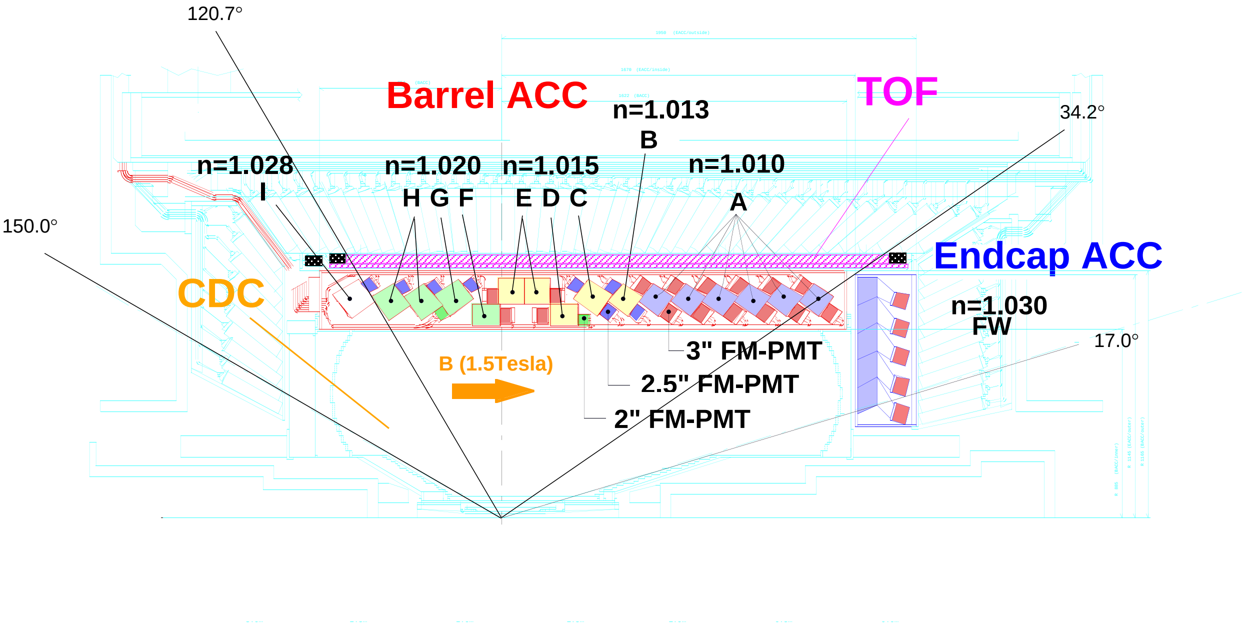

Figure 3.15: Configuration of ACC and TOF.

which is upper limit of particles momentum from B decay at Belle. Figure 3.16 shows momentum coverage of each detector. we estimate probability, which assumed kaon or pion in each detector, for each charged track. Then we calculate combined likelihood function which value is 1 (0) if particles likes kaon (pion) shown in Figure 3.17. The efficiency is about 85% with charged pion fake rate less than 10% shown in Figure 3.18.

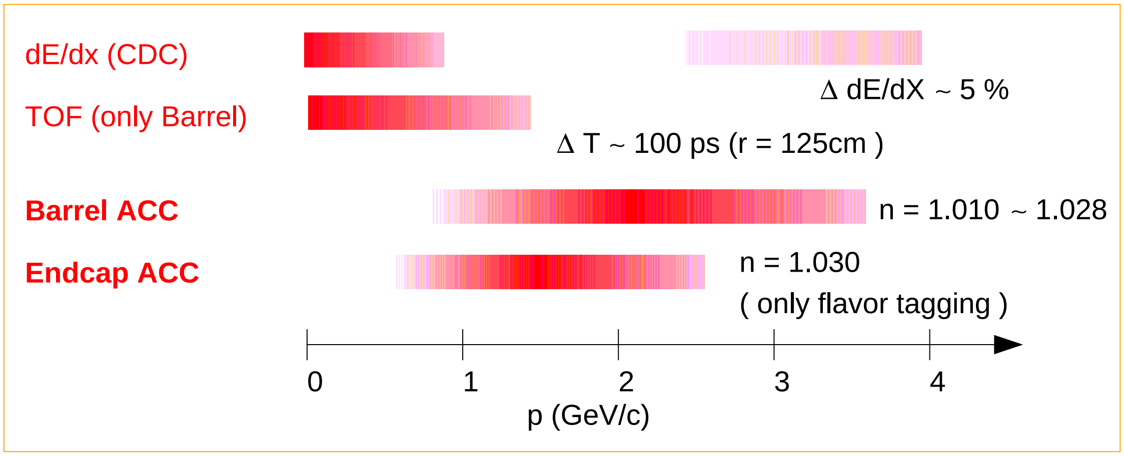

Figure 3.16: Figure of momentum coverage of each detector used for K/π separation.

3.2.6 Electromagnetic calorimeter (ECL)

ECL is designed mainly to detect photons and to identify electrons, but can also be used to detect K_L^0' s and minimum ionizing particles. The ECL consists of 8736 CsI(TI) crystals, arranged inside the detector barrel and endcaps as shown Figure 3.19, and covering the polar angle region $17° < \theta < 150°$.

Electrons and photons are detected in crystal calorimeters by electromagnetic showers. Electromagnetic showers are the result of repeated cascades of pair production and brehmstrahlung, producing an exponential increase in the number of particles, and corresponding decrease in particle energy until the energy is so low that ionization loss dominates, terminating the shower. Electrons and positrons in all parts of the shower have certain probability of exciting bands in the crystal lattice that correspond to visible energies, resulting in subsequent emission of visible photons, which are read out by photon detectors. The total light yield is proportional to the combined path-length of all electrons and positrons in the shown, which is proportional to the incident particles's energy. Electrons and photons typically deposit all their energy in the ECL. For heavier charged particles, on the other hand, brehmstrahlung is negligible, and they mainly leave energy by ionization, roughly

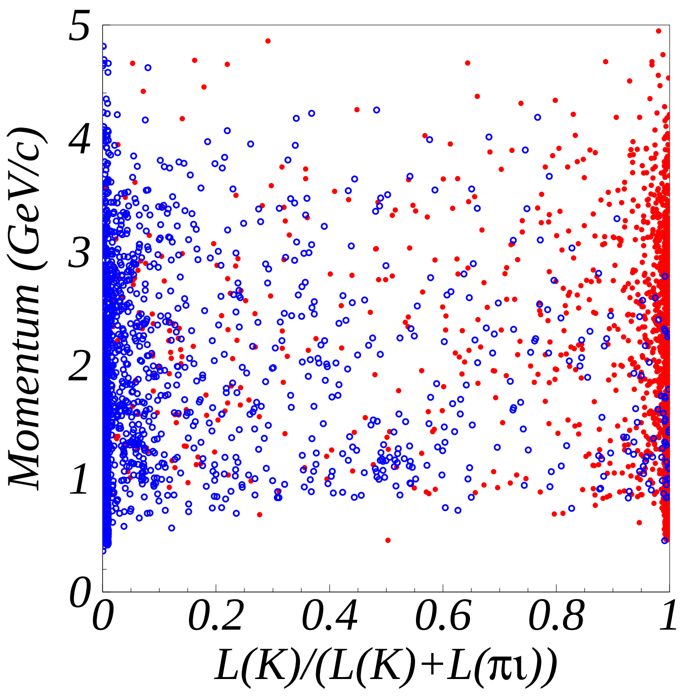

Figure 3.17: K/π separation 2D (momentum versus likelihood value) plot. Red plot is for Kaon's and blue one is for pion's likelihood value. we can separate K/π well.

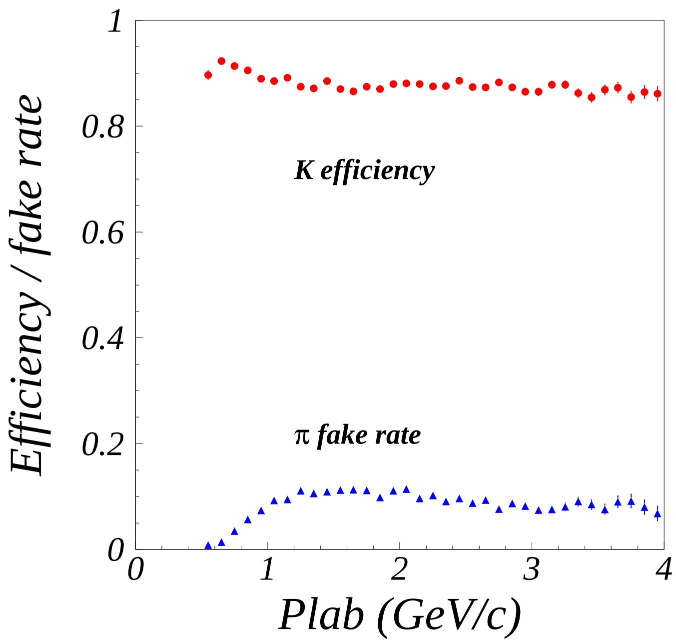

Figure 3.18: Kaon identification effiency and fake rate (miss identified for π) versus particles momentum.

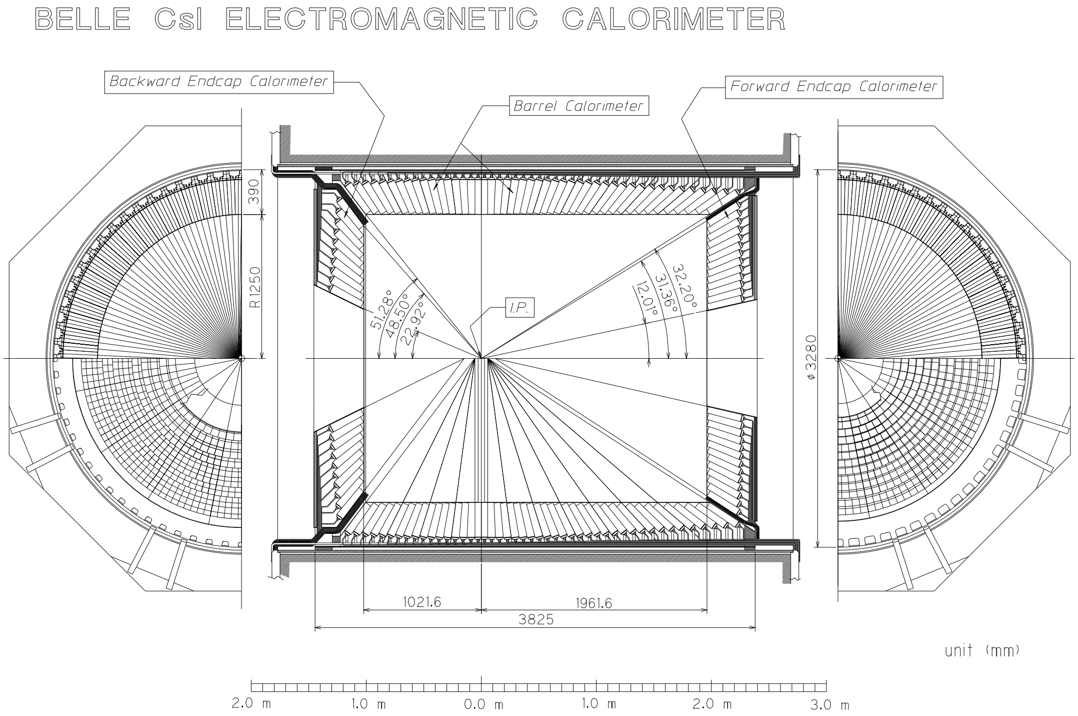

Figure 3.19: CsI Electromagnetic Calorimeter

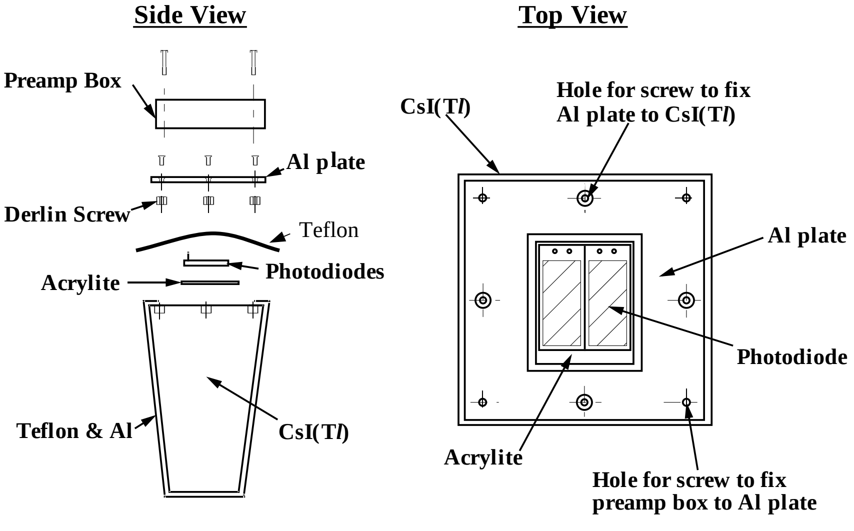

Figure 3.20: A single ECL counter

170 MeV for the 30-cm-log crystals. Neutral hadrons can be detected if they undergo inelastic strong interactions in the ECL, resulting in charged decay products, which can then be detected. These hadronic showers then to be less uniform in their shape than electromagnetic showers.

The individual crystals of the Belle EEL are oriented so that they point almost towards the interaction point, but with a small tilt, to ensure that photons cannot escape through th gaps between crystals. Each crystal has a trapezoidal shape, as shown in Figure 3.20. The exact dimensions of individual crystals vary with the polar angle, but their length is always 30 cm, which corresponds to 16.2 radiation lengths for electrons, and 0.8 nuclear interaction lengths for K_L^0's. All sides of a crystal, except the side where the readout is attached, are covered with a 200 μm of mylar. The Teflon serves as diffuse reflector, while the other layers provide optical and electrical isolation. The scintillation light from each crystal is collected using two photodiodes (Hamamatsu S2744-08), attached to the crystal by a 1 mm acrylate plate, and read out by charge sensitive preamplifiers.

After the commissioning of KEKB, the ECL energy measurement was calibrated counter by counter, using a large sample of Bhabha events, for which the electron energy is known as a function of the detection angle. The resulting energy resolution is shown Figure 3.21.

The details on the ECL and its performance can be found in [14].

3.2.7 Extreme forward calorimeter (EFC)

EFC consists of radiation hard Bismuth Germinate crystals. It is attached to the cryostat of the superconducting compensation solenoid magnets, which surround the beam pipe outside the interaction point in the forward and backward region. The EFC extends the coverage of the ECL to the polar angle regions 6.5° to 11.5° and 163.3° to 171.2°. The EFC is used as a beam and luminosity monitor, as well as an effective shield from backgrounds for the central drift chamber.

3.2.8 Superconducting magnet

Superconducting magnet, which encloses all of the abovementioned sub-detectors, provides a 1.5 T axial magnetic field. The superconduction magnet coil is supported by a surrounding aluminum cylinder of 3.4 m diameter, and is cooled with liquid helium.

The axial magnetic field causes charged particle to travel in a helix, with the $x-y$ projections of its trajectory being a circle of radius R, related to the field B by

$$R = \frac{cp_T}{qB} \tag{3.4}$$

where q is the charge of the particle, p_T is the particle's transverse momentum, and c is he speed of light, all in SI units. With units more useful in high energy physics,

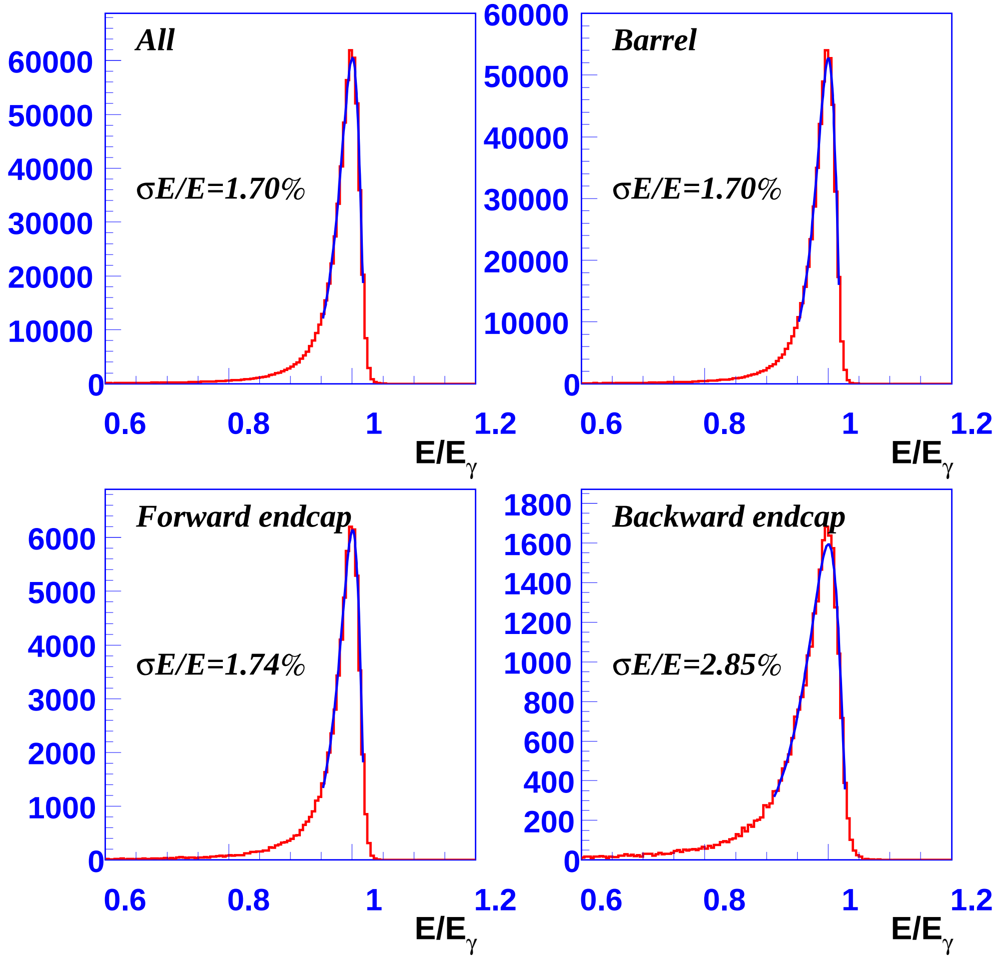

Figure 3.21: ECL energy resolution

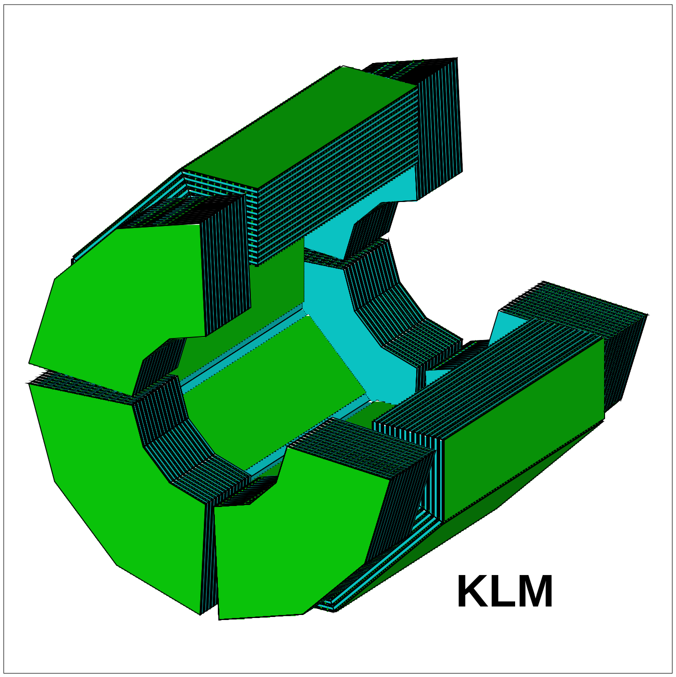

Figure 3.22: KLM

p_T measured in GeV/c, and q in multiples of the electron charge, this becomes

$$R = \frac{p_T}{0.3qB}. \tag{3.5}$$

Thus, we can determine a charged particle's momentum from the curvature of its trajectory in the drift chamber. Furthermore, we can tell the sign of the particle's charged from the direction that it curves.

3.2.9 K_L^0/μ detector (KLM)

As the name suggest, the KLM is used to identify K_L^0's and μ. Located outside the magnet coil in the barrel and both endcaps, it is the last sub-detector that particles encounter before leaving the detector. The KLM consists of 14 (Barrel) or 15 (EndCap) superlayers of Resistive Plate Chambers (RPC), sandwiched between 4.7 cm thick iron plates. The iron plates serve as the magnet's flux return, to induce hadronic interaction of K_L^0's, and to differentiate between charged hadrons and muons based on their penetration depth and deflection in the KLM. The KLM as a whole covers the polar angle region from $20° < \theta < 155°$, with the barrel detector covering $45° < \theta < 125°$.

The RPC used in the EndCap and Barrel differ somewhat in their detailed construction, but the operating principle is the same. We shall here describe the barrel detector. Each RPC superlayer contains two RPC layers, as shown in Figure

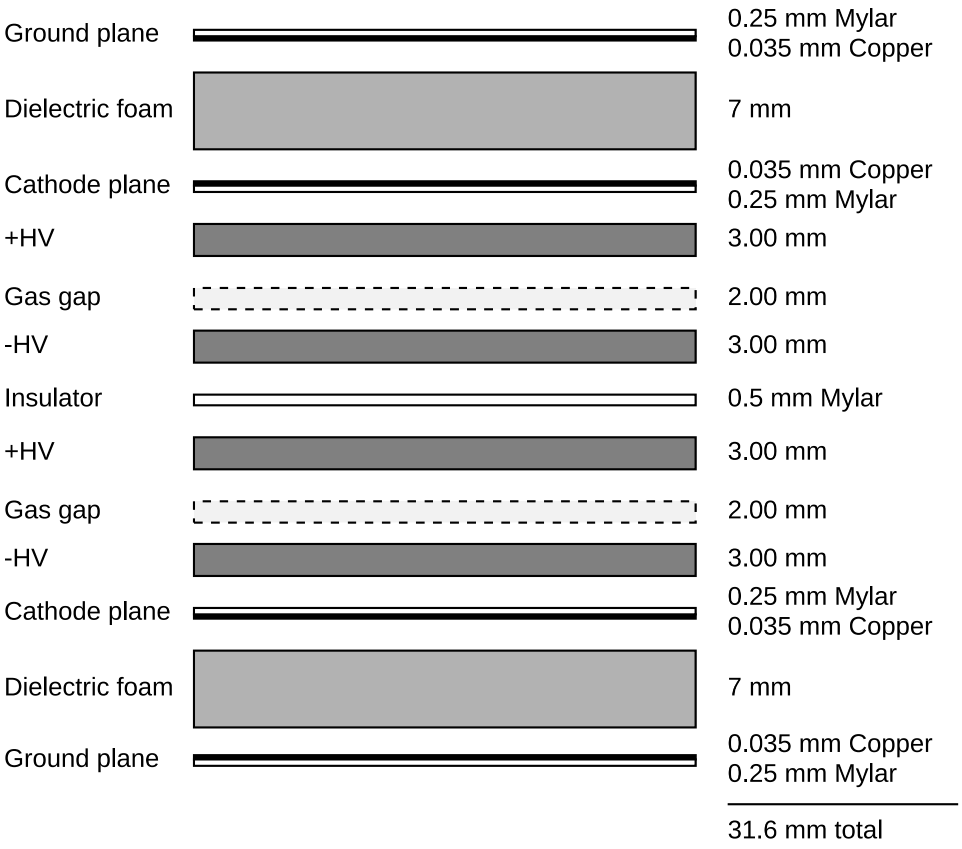

Figure 3.23: RPC super-layer module

3.23. Each single RPC layer consists of two glass plates, coated with conductive ink. In between the glass plates, their is a 1.9 mm gap, filled with an HFC/argon/butane gas mixture. A high voltage, typically 8000 V, is connected to conducting ink layers, which charged up the glass plates. Charged particles crossing the RPC leave a trail of ionization in the gas. This may result in a localized amount of surface charge on the glass plates discharging across the ionization trail. The image charge of this discharged is then picked up an dread out by $\approx$ 5 cm wide copper pickup strips, located outside the RPC. The pickup strips on one side run in the z direction, while the strips on the other side run in $r-\phi$ direction, so that 3D information is obtained. The high resistivity of the glass ensures that the discharged will be localize d to a small area in the glass plate. Even though this small area will be inactive until the charge is replenished from the conductive ink, the rest of detector area remains active during this time. Each single layer RPC typically has a detection efficiency $\approx$ 90% for charged tracks. Since two layers are read out together by one pair of pickup strips, however, we are effectively using the "logical or" of the two layers, resulting in average efficiencies above 98 %, shown Figure 3.24.

The RPC thus provided 3D information on the trajectory of charged tracks in the KLM detector. Using this information, charged tracks detected in the CDC are identified as μ based on their penetration depth into the KLM, and the deviation from their expected trajectory in the KLM. Muon identification efficiency above 1.5 GeV/c exceeds 90%, with a fake rate (from π and K) of less than 5%. The detail description of KLM is found in the refference [15].

The iron plates in the KLM provide a total of 3.9 interaction lengths for K_L^0's traveling normal to the detector planes. If a K_L^0 undergoes inelastic nuclear scattering in an iron layer, charged decay products can result in hits in the following RPC's. K_L^0's are thus identified as clusters of RPC hits without associated charged tracks in the drift chamber, as described further in Section 4.4.

3.2.10 Trigger & data acquisition (DAQ)

At KEKB's design luminosity, $10^{34}/cm^2/sec$, electron and positron beam bunches are spaced 60 cm apart, resulting in bunch crossings at the interaction point at a rate of about $500MHz$. During most bunch crossings' nothing happens, i.e. no e^+e^- collisions take pace. As can be seen from the cross sections given in table

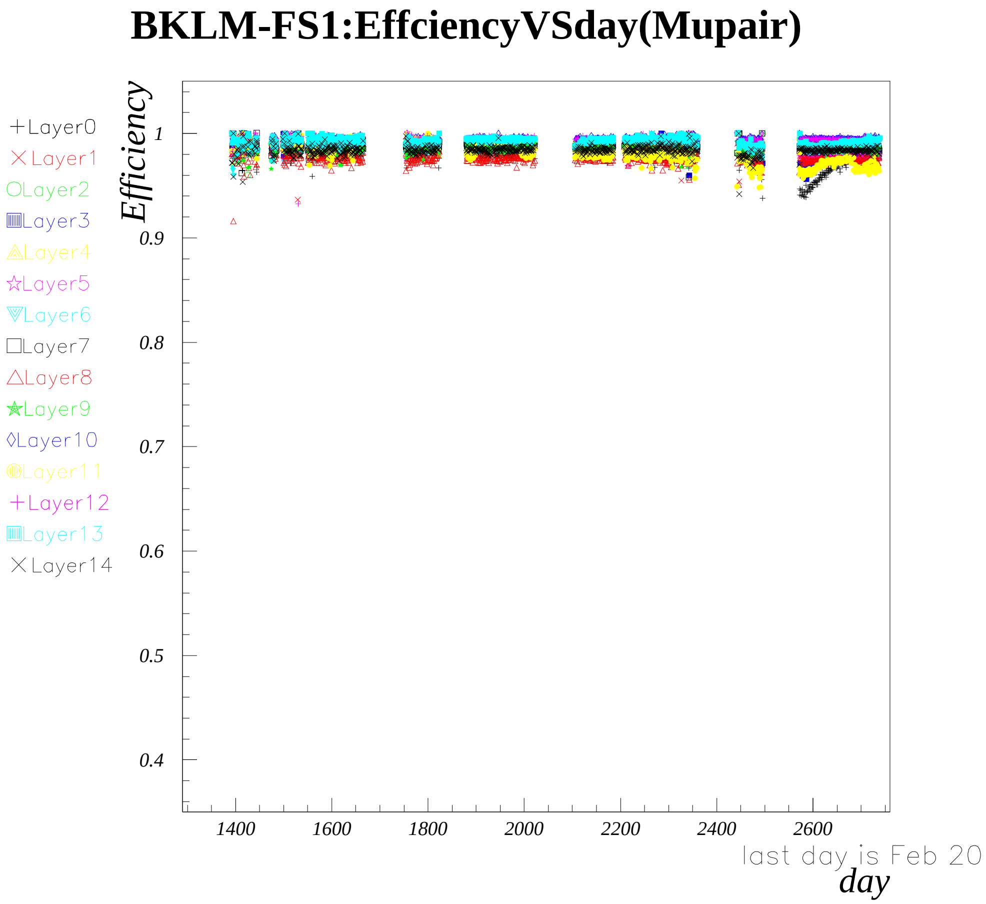

Figure 3.24: KLM-RPC super-layer efficiency VS days

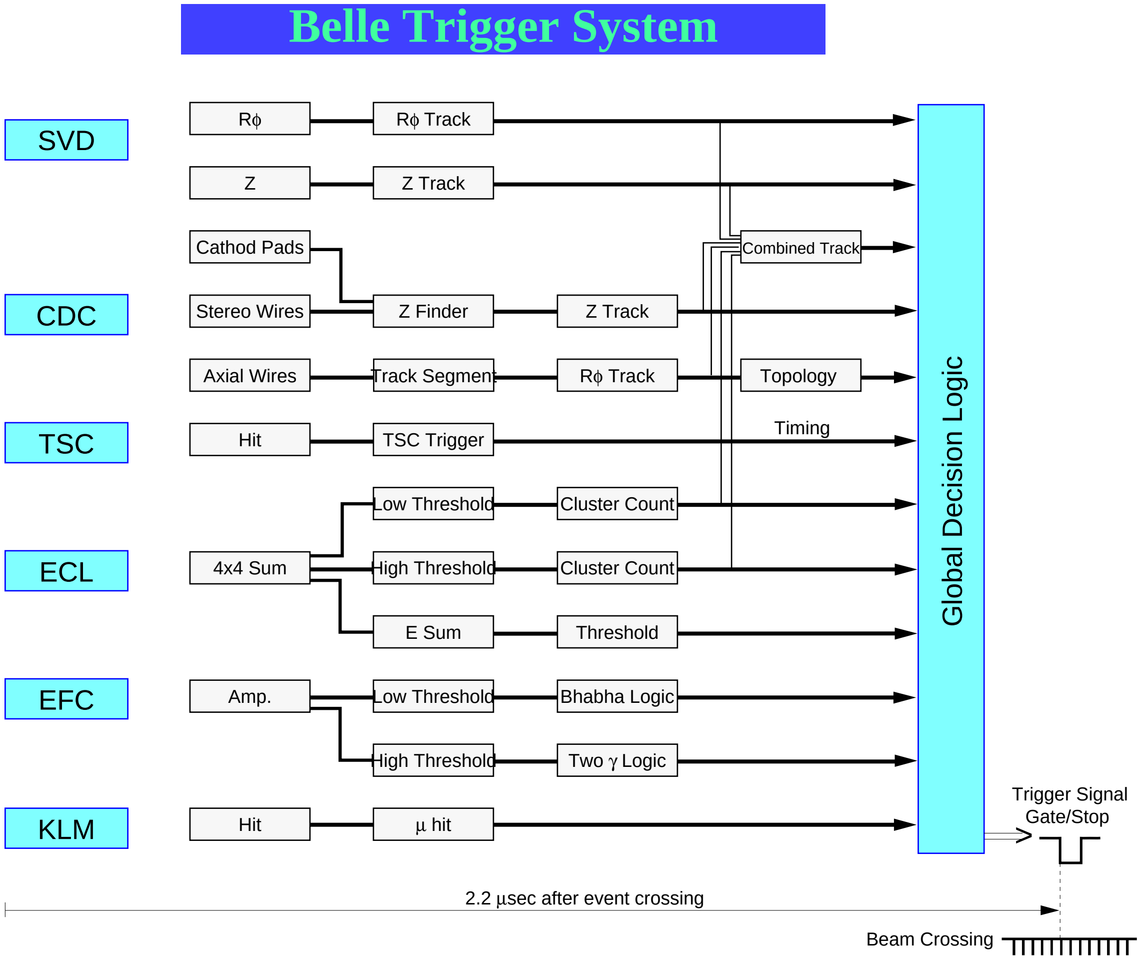

Figure 3.25: Trigger system

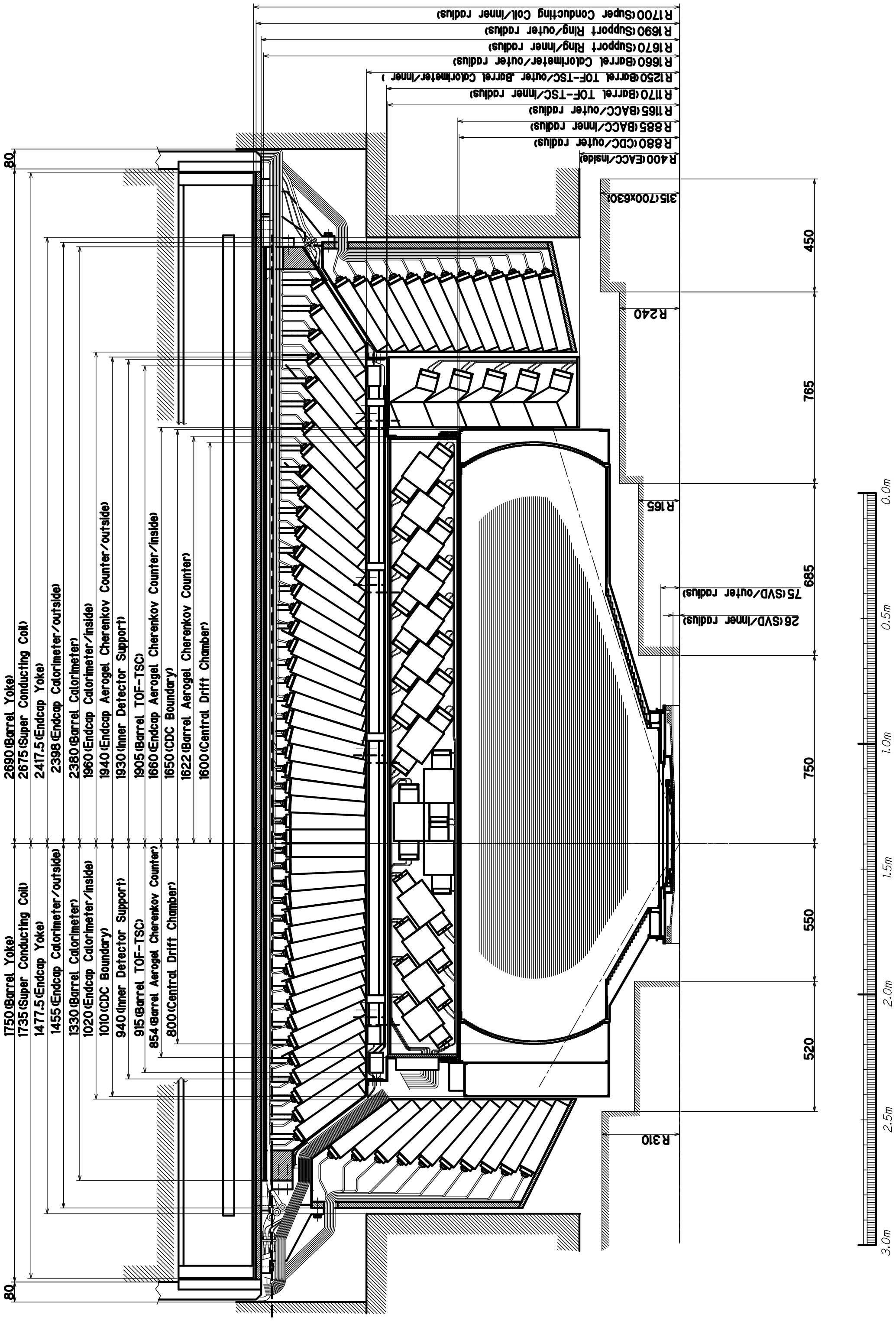

Figure 3.26: BELLE inner detector

Chapter 4

Event Reconstruction and Selection

In this chapter, we will explain how $B^0 \to J/\psi\ K_L^0$ candidates are reconstructed and selected from the large number of events collected at Belle. Figure 4.1 shows a flow chart of how to reconstruct and select $B^0 \to J/\psi\ K_L^0$ events, and to reject backgrounds. First we require "Hadronic event selection". Second we reconstruct good J/ψ from dilepton. Third we reconstruct K_L^0. But we know only the direction of K_L^0, a magnitude of K_L^0 is unknown. Then we reconstruct B using reconstructed J/ψ and K_L^0. Next we have to reject exclusive backgrounds, such as $B^0 \to J/\psi\ K_S^0$, $B^\pm \to J/\psi\ K^\pm$, $B \to J/\psi\ K^*$, $B^0 \to J/\psi\ \pi^0$ and etc by cut due to the event likelihood ratio, so purity of reconstructed B event comes to be higher. Finally, we correct the momentum of B due to beam energy fraction. These selections and correction are done only for $B^0 \to J/\psi\ K_L^0$ event. To measure $\sin 2\phi_1$, we need to measure the decay vertex position for each B decay.

We will see below how the present background fraction is the result of tuning individual cuts to minimize finally the uncertainty, when we use the selected candidate events to estimate $\sin 2\phi_1$. With the amount of data currently available, this uncertainty is dominated by its statistical component, which depends on the number of selected signal (S) and background events (N) as follows:

$$\sigma_{\sin 2\phi_1} \propto \frac{\sqrt{S+N}}{S} = \frac{1}{\mathbf{FOM}}.$$

Thus, we generally tune the various steps of the event selection to maximize the **F**igure **o**f **M**erit, FOM $= S/\sqrt{S+N}$. The purity could be increased further, thus this would result lower statistical sensitivity, due to increased rejection of signal events. We sometimes deviate from our main strategy of optimizing the FOM, when there is a way of significantly decreasing systematic uncertainties, while either keeping the FOM constant, or only lowering it slightly.

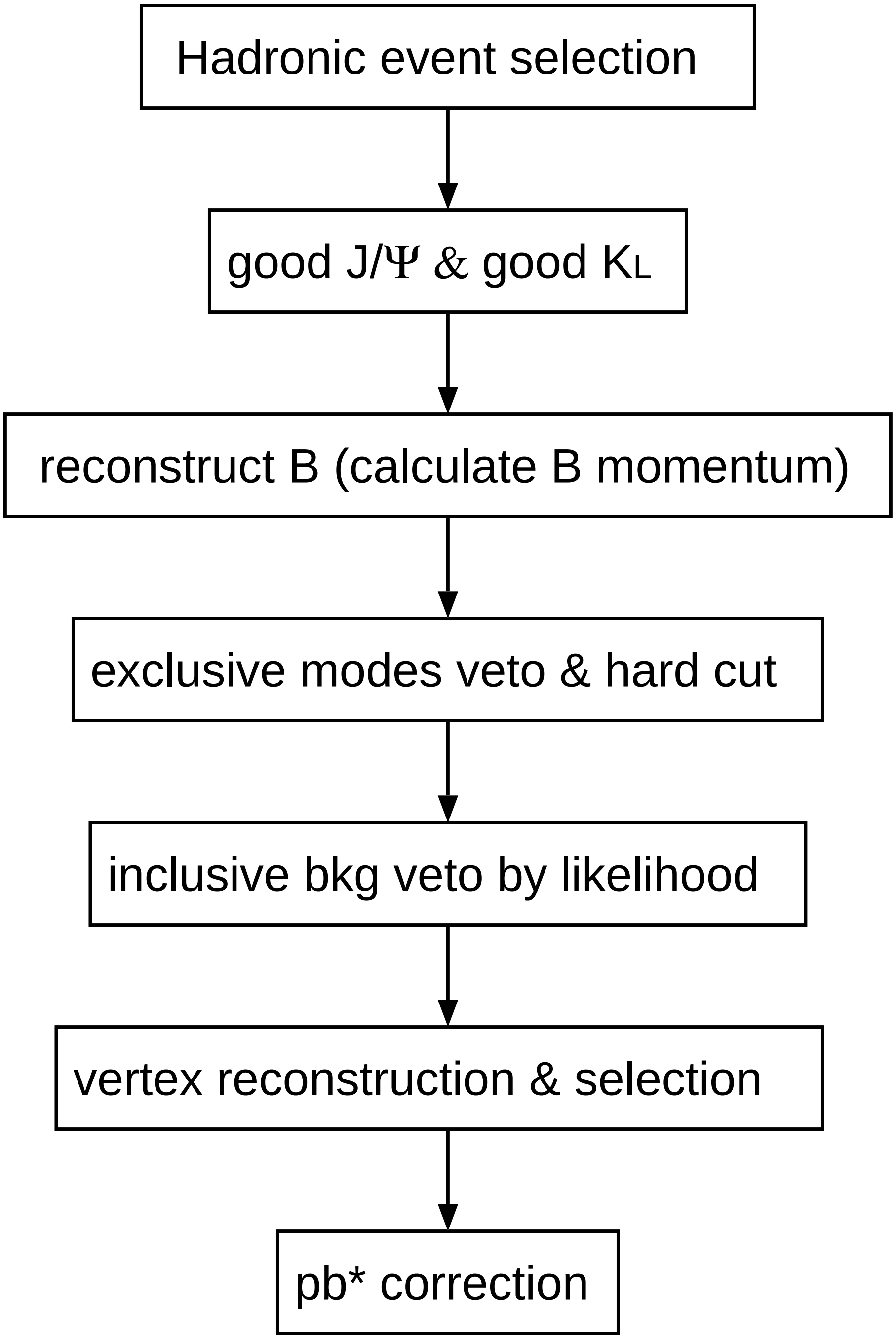

Figure 4.1: Reconstruction and selection flow chart of $B^0 \to J/\psi\ K_L^0$ level

4.1 Data set

The analysis presented in this thesis is based on the data taken from January 2000 and July 2003. The total integrated luminosity $140/fb$ has been accumulated in this period. The total number of $B\bar{B}$ pairs used for this analysis is approximately 1.5×10^8.

4.2 Hadronic event selection

To reject non-Hadronic events, we require the following hadronic selections,

1 Number of "good" tracks are greater than 3, where "good" tracks are defined by $|r| < 2.0$ cm and $|z| < 4.0$ cm at the closest approach to the beam axis, and transverse momentum, p_t, is greater than 0.1 GeV/c.

2 The absolute value of the momentum balance in the z-component in the $\Upsilon(4S)$ center-of-mass system (CMS) must be less than a half of the center-of-mass energy.

3 Event vertex should be within 1.5 (3.5) cm from the interaction point in $r(z)$ plane.

4 Total visible energy, sum of the energy of "good" tracks assumed pion and "good" gamma, in the CMS of $\Upsilon(4S)$. should be greater than 20% of the CMS energy

5 Sum of all gamma energy in the CMS of $\Upsilon(4S)$ should be in the range from 10% to 80% of the CMS energy.

4.3 Reconstruction of J/ψ

We reconstruct J/ψ from their decays into two leptons of the same flavor. The combined branching fraction of $J/\psi \to e^+e^-$ and $J/\psi \to \mu^+\mu^-$ is about 12%. J/ψ is too light to decay into two τ-leptons. We use opposite charged track pairs which both tracks are identified as leptons ($e^\pm$ or $\mu^\pm$). If the tracks do not come from the interaction region, we remove these candidates. In the $J/\psi \to e^+e^-$ decay, in order to include radiative e^+e^- events, we reconstruct the events by including the lorentz vector of γ within 0.05 radians of each e^+ or e^- direction.

We required the invariant mass of dileptons, $M_{l^+l^-}$, should be in the range $3.05 < M_{l^+l^-} < 3.13$ GeV/c^2 to identify as a good J/ψ candidate. This requirement is tighter than other analyses for exclusive CP-decay modes, for example $B^0 \to J/\psi\ K^0_S$, which contain J/ψ. Because for $B^0 \to J/\psi\ K^0_L$ case, the purity of events is worse than other CP-event due to worse reconstruction of K^0_L. Figure 4.2 shows invariant mass distribution of reconstructed J/ψ from $J/\psi \to e^+e^-$ and

$J/\psi \rightarrow \mu^+\mu^-$. We can see clear peak around $M_{l^+l^-} \approx 3.097\ GeV/c^2$, and low backgrounds in both decay.

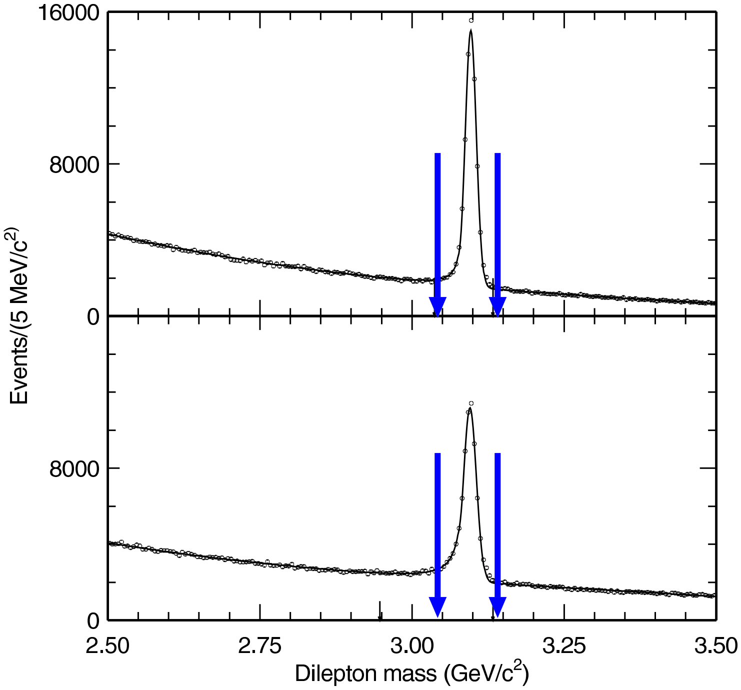

Figure 4.2: Invariant mass distribution of J/ψ. Upper (Lower) distribution is reconstructed from $\mu^+\mu^-(e^+e^-)$.

4.4 Reconstruction of K_L^0

We detect K_L^0 as hadronic showers in KLM and/or ECL. So, we have two categories of reconstruction of K_L^0. First one is reconstructed in KLM, so called "KLM candidate". Second one is reconstructed in ECL, so called "ECL candidate".

4.4.1 KLM candidate

How to reconstruct K_L^0 in KLM is as follows. We handle KLM hit information as hadron cluster. First we combine RPC superlayer hits within 5° opening angles of each other. If there is no hit, we define one cluster. Second we check that KLM is associated with ECL or not. If there is ECL cluster which energy is greater than 0.16 GeV within 15° opening angle, we define KLM cluster is associated with ECL cluster. If KLM cluster is not associated with ECL cluster, to reject noise hits in KLM, we require that the number of hit layers is greater than or equal 2. If KLM

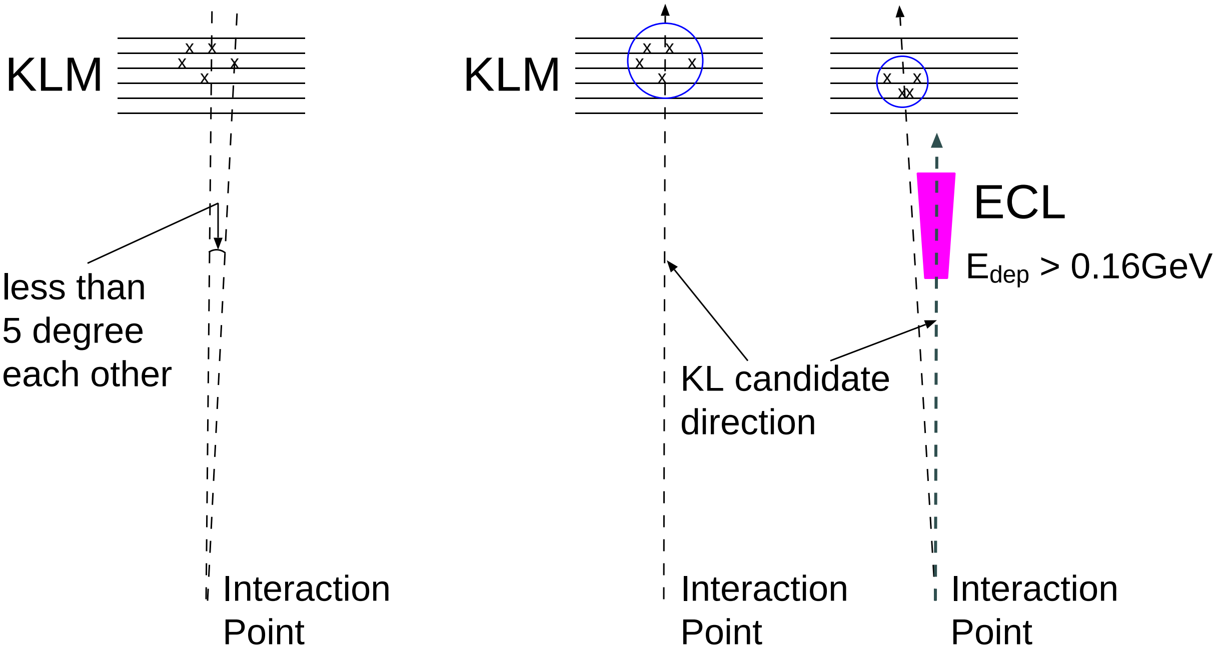

Figure 4.3: Left figure shows the image of K_L^0 cluster and right figure shows the definition of K_L^0 cluster in KLM.

cluster is associated with ECL cluster, we do not set any requirement to the number of hit layers.

Then we decide K_L^0 direction. If KLM is associated with ECL, we use ECL cluster direction. This is because angular resolution of ECL cluster is better than that of KLM. We call this type of reconstructed K_L^0 as "KLM+ECL candidate". If KLM is not associated with ECL cluster, we use KLM cluster direction. we call this type of reconstructed K_L^0 as "KLM-only candidate". Both "KLM+ECL candidates" and "KLM-only candidates", we call "KLM candidate". Figure 4.3 shows image of this clustering methods.

Finally, we check the KLM cluster is associated with charged track or not. If there is charged track with in 15° cone angle around K_L^0 direction, we consider that this K_L^0 cluster made from charged track. So we reject these clusters. Figure 4.4 shows the extrapolation of charged track into KLM.

4.4.2 ECL candidate

We write here how to reconstruct K_L^0 in ECL. The main backgrounds in K_L^0 candidates reconstructed by ECL-only candidates come from the interaction of γ and charged particle with ECL. In order to discriminate electromagnetic interactions caused by γ from hadronic interactions by K_L^0, we use the characteristic difference between electromagnetic and hadronic showers. In order to reject charged particles backgrounds, we check the matching of charged particle tracks to ECL clusters.

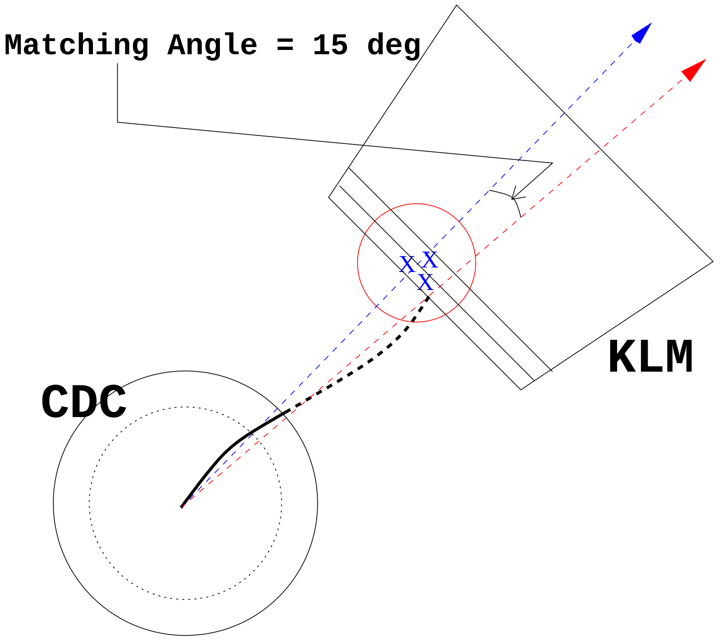

Figure 4.4: Image of extrapolation of charged track into KLM. Blue arrow is the direction of K_L^0 cluster and red arrow is direction of charged track in KLM. Black curve is a flight direction of extrapolated charged track.

ECL candidates are selected by following parameters,

1 Distance: distance between the ECL cluster and the point where the closest charged track hits the ECL detector.

2 Energy : total energy of the ECL cluster.

3 Energy ratio, e9/e25 : the ratio of energy (e9) in a 3×3 to that (e25) in a 5×5 ECL crystal array surrounding the shower sector, as shown in Figure 4.5. If ECL cluster is made from photon, ECL cluster shower is tighter than that of K_L^0 cluster. So, energy ratio e9/e25 is close to 1 for the gamma background.

4 Width : shower width of the ECL cluster. cluster shower width caused by K_L^0 is wider than that of by γ.

5 Mass : mass of ECL cluster. By subdividing the ECL cluster into sub-clusters and summing up their four vectors, we obtain a four vector with non-zero mass.

Figure 4.6 shows each distributions of discriminant variables for true K_L^0 clusters and fake K_L^0 clusters obtained by the Monte Carlo simulation. At first, we require the loose pre-selection criteria to these variables, shown in Table 4.1. We can remove obvious fake K_L^0 backgrounds by these selection cuts, but a few loss of true K_L^0.

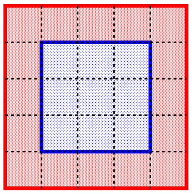

Figure 4.5: Image of ECL cluster array for 9 and 25 cells .

distance > 20 cm
energy > 0.2 GeV
e9/e25 < 0.99
width > 4 cm
mass > 0.013 GeV/c^2

Table 4.1: The loose pre-selection criteria for ECL candidate.

In order to increase the purity of K_L^0 reconstruction, we use the five cluster properties to assign K_L^0-likelihood ratio for each ECL cluster. We choose to optimize its performance for the $B^0 \to J/\psi\ K_L^0$ analysis by creating **P**robability **D**ensity **F**unction (PDF) from charmonium inclusive B decay Monte Carlo. We take the product of the PDF for signal and background, as shown in Equation (4.1). Then we take a likelihood ratio as a discriminant variable, as shown in Equation (4.2).

$$\textbf{Likelihood} : L = \prod_i \textbf{PDF}_i \tag{4.1}$$

$$\textbf{Likelihood Ratio} = L^{true}_{K_L^0} / (L^{true}_{K_L^0} + L^{fake}_{K_L^0}) \tag{4.2}$$

We obtain K_L^0-likelihood ratio value between 0 and 1. Figure 4.7 shows the Likelihood Ratio distribution for true K_L^0 and fake K_L^0, signal noise ratio (S/N), and FOM distributions. If Likelihood Ratio is greater than 0.5, we define that ECL cluster is made from K_L^0, and we use as K_L^0 candidate when we reconstruct $B^0 \to J/\psi\ K_L^0$.

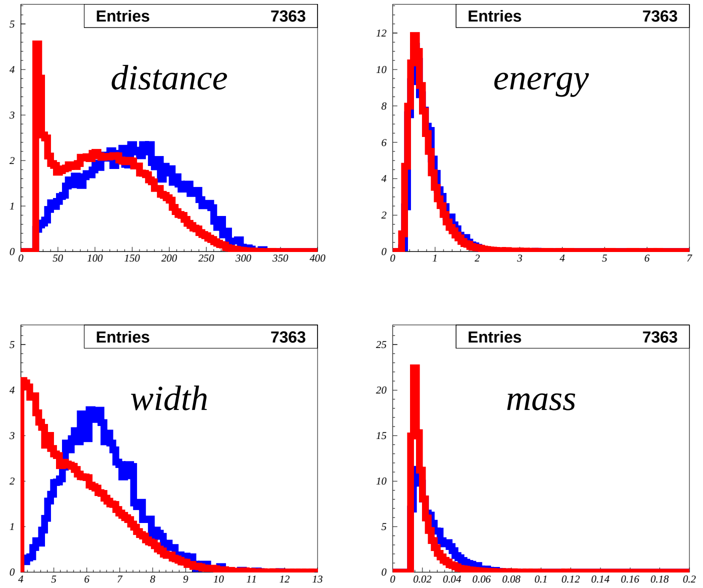

Figure 4.6: PDF distributions for ECL cluster. Blue (Red) histograms shows signal (background) events in Monte Carlo

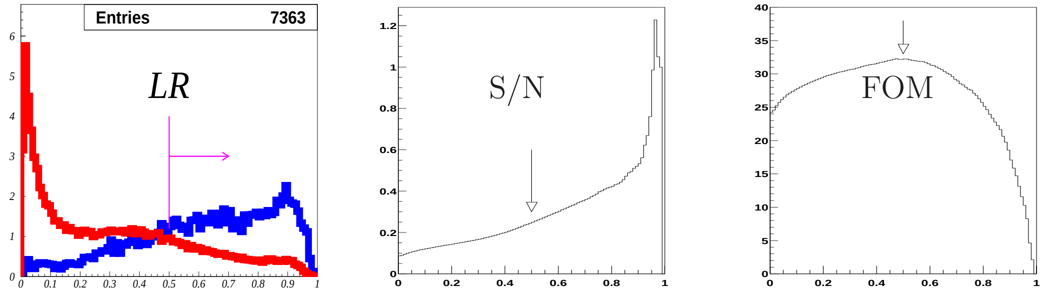

Figure 4.7: Left distributions are likelihood ratio of true K_L^0 (blue) and fake K_L^0 (red). Middle distributions are S/N and right distribution is FOM vs likelihood ratio cut value. Arrow position is a cut value of LR=0.5.

4.5 Reconstruction of $B^0 \to J/\psi\ K_L^0$

We have two K_L^0 categories "KLM" and "ECL" candidate. First, we use "KLM" candidates, because the purity of "KLM" candidate is higher than that of "ECL" candidate, and also the background source is different between these two candidate. Therefor, we try to reconstruct $B^0 \to J/\psi\ K_L^0$ with "KLM" candidates. If "KLM" candidate does not pass the selection criteria, as describes below, we try to reconstruct $B^0 \to J/\psi\ K_L^0$ with "ECL" candidates.

We know only the direction of $K_L^0(\widehat{\boldsymbol{P}}_{K_L^0})$ from our detector, but we can calculate the momentum ($|\boldsymbol{P_{K_L^0}}|$) and the energy ($E_{K_L^0}$) of K_L^0. In $B^0 \to J/\psi\ K_L^0$ decay, the following kinematical equation is given without any assumption:

$$\begin{aligned} E_{B^0} &= E_{J/\psi} + E_{K_L^0} \\ \boldsymbol{P_{B^0}} &= \boldsymbol{P_{J/\psi}} + \boldsymbol{P_{K_L^0}} \\ \boldsymbol{P_{K_L^0}} &= |\boldsymbol{P_{K_L^0}}|\widehat{\boldsymbol{P}}_{K_L^0} \end{aligned}$$

then we get,

$$m_{B^0}{}^2 = \left(E_{J/\psi} + \sqrt{|\boldsymbol{P_{K_L^0}}|^2 + m_{K_L^0}^2}\right)^2 - |\boldsymbol{P_{J/\psi}} + \boldsymbol{P_{K_L^0}}|^2 \tag{4.3}$$

where m_{B^0} and $m_{K_L^0}$ are the mass of B^0 and K_L^0, and both are known as 5.279 GeV and 0.497 GeV, respectively. So we can calculate the magnitude of K_L^0 momentum in laboratory frame. After that, we obtain the momentum of B, p_B^*, in the **C**enter-of-**M**ass **S**ystem (CMS). Figure 4.8 shows the p_B^* distributions for each candidate in signal Monte Carlo. We can see clear peak around 0.335110 GeV/c (nominal p_B^* value).

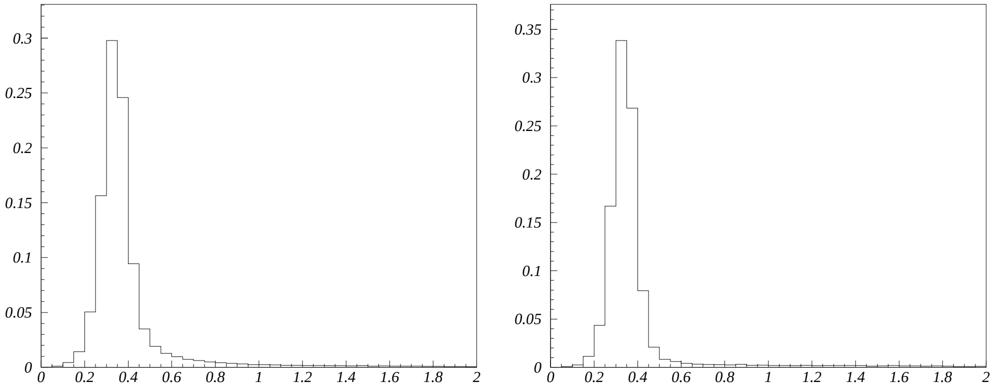

Figure 4.8: p_B^* distributions in Monte Carlo. Left (Right) distribution is KLM (ECL) candidate.

4.6 Selection of $B^0 \to J/\psi\ K_L^0$

Now we reconstruct $B^0 \to J/\psi\ K_L^0$ event by using the reconstructed J/ψ and K_L^0. But many backgrounds still remains. In this section, we try to reject many types of backgrounds shown in following subsection.

4.6.1 Exclusive mode veto

We reject the events if we can reconstruct the following modes with reconstructed J/ψ, which we required the invariant mass of dileptons to be in the range $2.95 < M_{e^+e^-} < 3.13\ GeV/c^2$ and $3.05 < M_{\mu^+\mu^-} < 3.13\ GeV/c^2$. In this case, we require looser selection to J/ψ's mass than the case of $B^0 \to J/\psi\ K_L^0$ reconstruction. This is because the accuracy of K_L^0 momentum is worse than that of $K^\pm$, K_S^0 and pion. So the purity of $B^0 \to J/\psi\ K_L^0$ event depends on the amount of background in J/ψ. The backgrounds are as follows,

1 $B^0 \to J/\psi\ K_S^0 (K_S^0 \to \pi^+\pi^-)$.

2 $B^\pm \to J/\psi\ K^\pm$.

3 $B^0 \to J/\psi\ \pi^0$.

4 $B^0 \to J/\psi\ K^{*0}(K_S^0\pi^0)$.

5 $B^\pm \to J/\psi\ K^{*0}(K^\pm\pi^\mp)$.

6 $B^\pm \to J/\psi\ K^{*\pm}(K^\pm\pi^0, K^\pm\pi^0)$.

For these mode, we can fully reconstruct events. We use two variables reflecting the known values of the B meson's energy and momentum. We define these variables named ΔE and M_{bc} (beam constrained mass) as following,

$$\begin{aligned} \Delta E &= E_B^* - E_{beam}^* \\ M_{bc} &= \sqrt{{E_{beam}^*}^2 - {p_B^*}^2} \end{aligned}$$

where E_B^* is the energy of reconstructed B meson in the CMS and E_{beam}^* is the beam energy in the CMS and p_B^* is the reconstructed B momentum in the CMS. If we can reconstruct any of these modes in the range $|\Delta E| < 50\ MeV$ and $5.27 < M_{bc} < 5.29\ GeV/c^2$, we consider that the event is not $J/\psi\ K_L^0$ event, other exclusive event. We reject these events from the $B^0 \to J/\psi\ K_L^0$ candidates. Figure 4.9 shows M_{bc} distribution from experimental data. The cut $|\Delta E| < 50\ MeV$ has been applied.

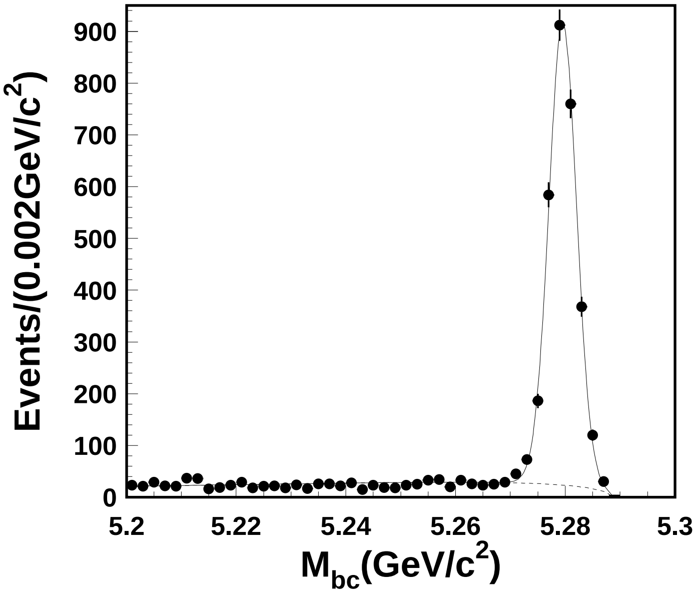

Figure 4.9: M_{bc} distribution within the ΔE region.

4.6.2 Hard cut

We can estimate the direction of K_L^0 from the four-momentum of J/ψ and beam energy assuming $B^0 \to J/\psi\ K_L^0$ decay of B meson which the energy is a half of the four-momentum of the $\Upsilon(4s)$. We reject the event which the calculated K_L^0 direction due to the cluster is too far from the expected direction. Figure 4.10 shows the distribution of $\cos\theta_{expectedK_L^0,calcutedK_L^0}$, between the expected K_L^0 and the calculated K_L^0 direction. We require following condition,

$$\cos\theta_{expectedK_L^0,calcutedK_L^0} > 0.8.$$

4.6.3 Inclusive background veto by LR

In order to suppress the background from inclusive charmonium B decay, we calculate likelihood ratio for $B^0 \to J/\psi\ K_L^0$ from the following PDFs, No.1 to No.6.

1 $p^*_{J\psi}$: Momentum of J/ψ in the CMS. $B^0 \to J/\psi\ K_L^0$ decay is two-body decay, and other inclusive backgrounds are multi-body decay. Therefore momentum of J/ψ is higher than that of other inclusive backgrounds. $p^*_{J\psi}$ is not monochromatic due to the motion of B in the CMS.

2 $\cos\theta_{K_L^0,\pi^\pm}$: cosine of the angle between the K_L^0 and closest charged track assumed π which momentum is greater than 0.7 GeV/c. When we reconstruct

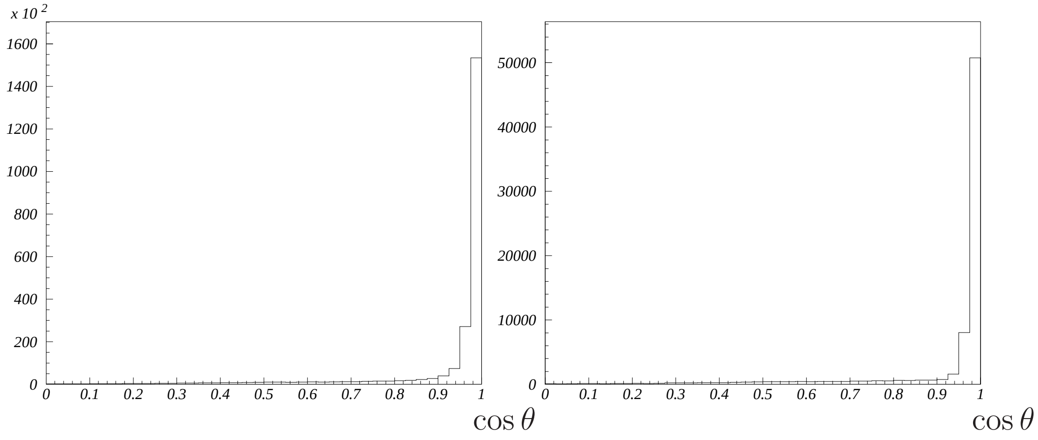

Figure 4.10: $\cos\theta_{expectedK_L^0,calcutedK_L^0}$ distribution for KLM (left) and ECL (right) candidates in $B^0 \to J/\psi\ K_L^0$ Monte Carlo.

K_L^0, we reject charged tracks association. But still remains charged tracks backgrounds. In order to reject these backgrounds we include this parameter when we calculate likelihood.

3 N_{trk} : Number of charged tracks with $p_t > 0.1\ GeV/c$, $|dr| < 2\ cm$, and $|dz| < 4\ cm$, where dr and dz represent the distance of closest approach to the interaction point. In $B^0 \to J/\psi\ K_L^0$ decay, one track is K_L^0 in one side of B ($B^0 \to J/\psi\ K_L^0$ event has only two charged tracks) and other side of B decays generic. So the event multiplicity may be less than other generic B decay.

4 $\cos\theta_B^*$: Polar angle of reconstructed B meson momentum in the CMS. Considering $B^0 \to J/\psi\ K_L^0$ helicity,

$$B^0 = \frac{1}{2}(0^-)\ ,\ J/\psi = 0^-(1^{--})\ ,\ K_L^0 = \frac{1}{2}(0^-)$$

In $e^+e^- \to \Upsilon(4S) \to B\bar{B}$ transition, $\Upsilon(4S)$'s spin is 1, B's spin is 0. In CMS, $\cos\theta_B^*$ should be polarized. If we reconstruct background as $B^0 \to J/\psi\ K_L^0$, reconstructed $\cos\theta_B^*$ helicity should be flat.

5 $p_B^*(3)$: Calculated momentum of reconstructed $B^\pm \to J/\psi\ K^{*\pm}(K^{*\pm} \to K_L^0\pi^\pm)$ assumption. This PDF is used if $p_B^*(3) < 0.8\ GeV/c$, $0.852\ GeV/c^2 < M_{recK^{*\pm}} < 0.930\ GeV/c^2$, and $p^*_{used\pi^\pm} > 0.35\ GeV/c$ If we reconstruct $B^0 \to J/\psi\ K_L^0$ events as $B^\pm \to J/\psi\ K^{*\pm}$, the momentum of B is higher than that of $B^0 \to J/\psi\ K_L^0$. On the other hand, the momentum of B with true $B^\pm \to J/\psi\ K^{*\pm}$ event should be nominal peak value.

6 $E_{ecl}/E_{calcK_L^0}$: Ratio of the energy deposit in the ECL to the calculated K_L^0 energy, if K_L^0 is associated in ECL for "KLM+ECL" and "ECL-only" candidates, and $B^0 \to J/\psi\ K_L^0$ decay is assumed.

Figure 4.11 shows each PDF. The procedure for constructing this $B^0 \to J/\psi\ K_L^0$-likelihood ratio is very similar to the procedure for constructing the K_L^0-likelihood ratio, which is described in Section 4.4.2. Before we calculate PDFs ,we require the following pre-selection to remove obvious background.

$$\boxed{\begin{array}{c} 1.2 < p^*_{J/\psi} < 2.0 \\ 2 < N_{trk} < 13 \\ 0 < E_{ecl}/E_{calcK_L^0} < 1 \end{array}}$$

Then we calculate the likelihood ratio for $B^0 \to J/\psi\ K_L^0$ by the same method as obtaining the K_L^0-likelihood ratio. Figure 4.12 shows the likelihood ratio and FOM distributions for KLM and ECL candidate.

We require the likelihood ratio to be greater than 0.4.

4.7 p^*_B correction due to instability of beam energy

KEKB beam energy would be stable in time, which means the center-of-mass energy in the e^+e^- collision ($\sqrt{s}$) equals $\Upsilon(4S)$ rest energy. However, in generally two beam energies fluctuate a little bit. So, $\sqrt{s}$ is different event by event. In order to correct this instability, we expect the B meson momentum, p^*_B, in $\Upsilon(4S)$ center-of-mass system from beam information event by event as the following equation,

$$p^*_{B(expected)} = \sqrt{E_{beam} - m^2_{B^0}}.$$

We already know the calculated B meson's momentum, $p^*_{B(calculated)}$, in CMS from reconstruction using experimental Data and we can define exact B meson's momentum in CMS, $p^*_{B(MC)}$, from Monte Carlo study. In Monte Carlo we define beam energy as nominal values which is stable in event by event. Using $E_{LER} = 3.5000\ GeV$ for the low energy ring, $E_{HER} = 7.9965\ GeV$ for the high energy ring and $\theta_{crossingangle} = 22\ mrad$ for the crossing angle in Monte Carlo, the value of $p^*_{B(MC)}$ is a constant to be $0.335110\ GeV/c$. We use $m_{B^0} = 5.2794\ GeV/c^2$ when we calculate $p^*_{B(calculated)}$, $p^*_{B(expected)}$ and $p^*_{B(MC)}$.

Finally we correct p^*_B by the following equation,

$$p^*_{B(corrected)} = p^*_{B(calculated)} - p^*_{B(expected)} + p^*_{B(MC)}.$$

Figure 4.13 shows B meson's momentum distributions for KLM and ECL candidate after correction of beam instability.

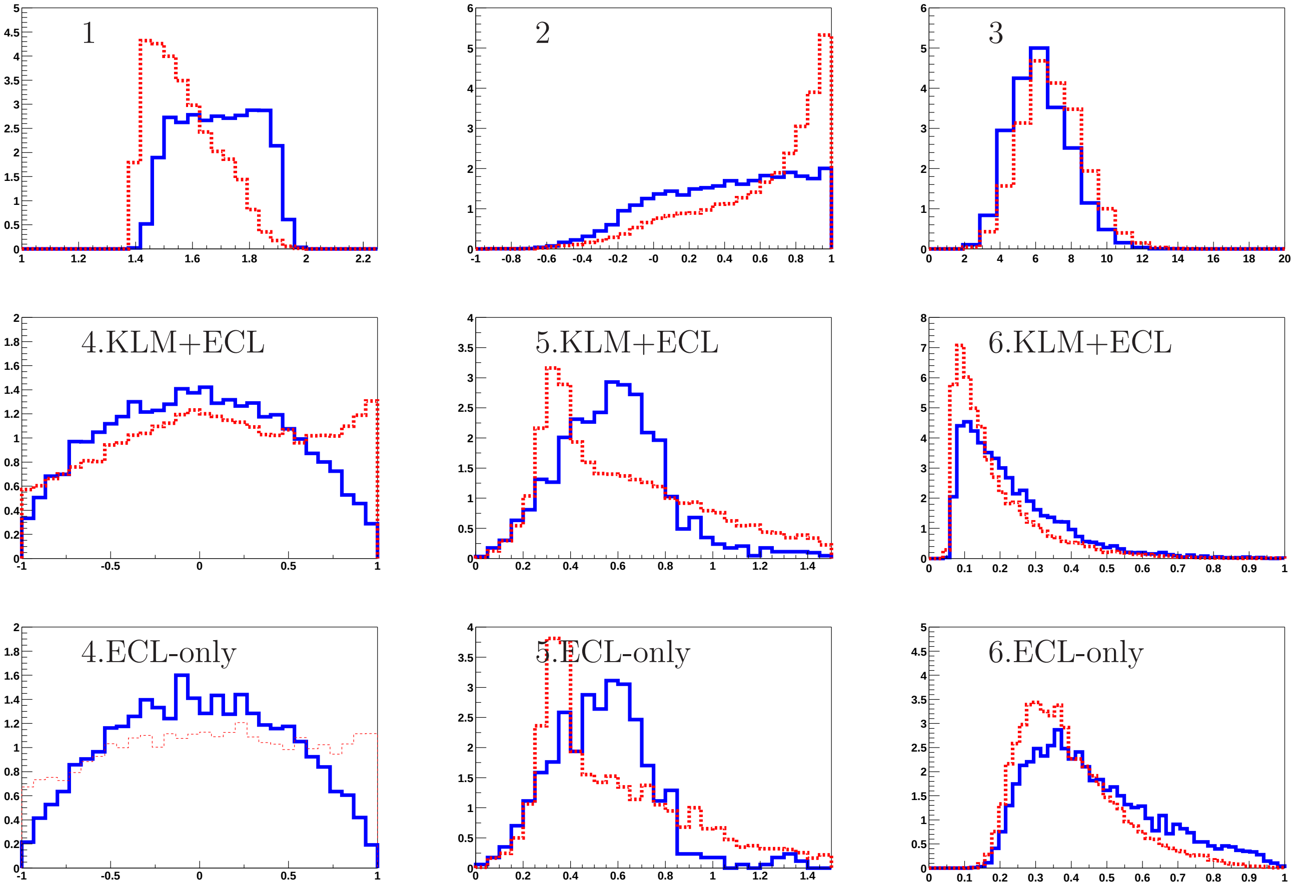

Figure 4.11: PDF distributions for $B^0 \to J/\psi\ K_L^0$ likelihood ratio, blue (red) histogram are signal (background) in Monte Carlo. No.1, No.2, No.3, No.4, No.5 and No.6 histograms are $p^*_{J\psi}$, $\cos\theta_{K_L^0,\pi^\pm}$, N_{trk}, $\cos\theta^*_B$, $p^*_B(3)$ and $E_{ecl}/E_{calcK_L^0}$, respectively.

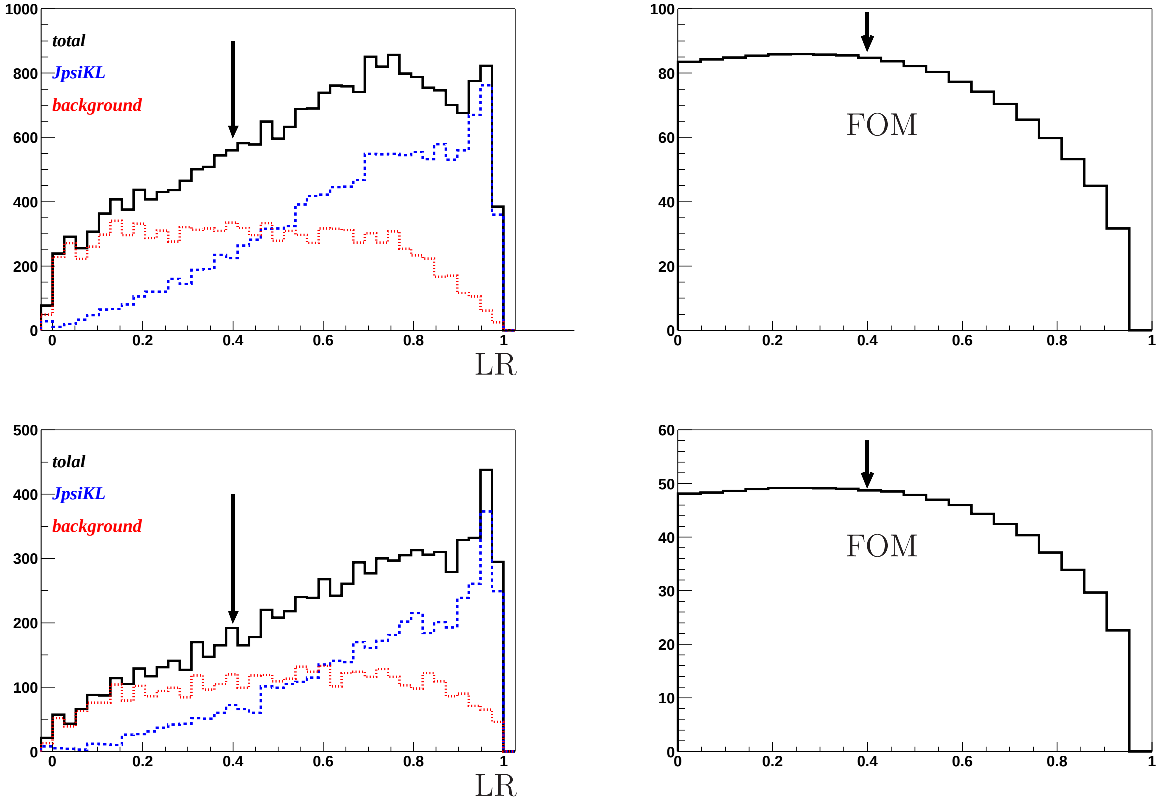

Figure 4.12: The likelihood ratio distributions (left) and FOM distributions (right). Upper (Lower) histograms are for KLM (ECL) candidates.

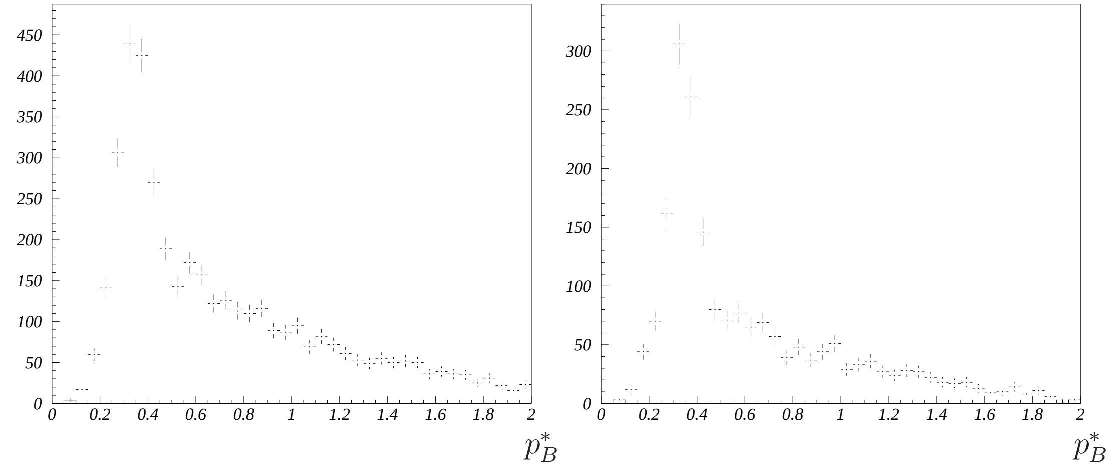

Figure 4.13: p_b^* distribution after likelihood ratio cut and beam correction. Left (Right) is for KLM (ECL) candidates.

4.8 Vertexing

After all selection cuts, including p_B^* correction, we measure decay vertex points. There are two vertex points. One is B meson's vertex point which is reconstructed as $B^0 \to J/\psi\ K_L^0$, and the other B meson's vertex point. We define B_{cp} as "CP-side" B meson which is reconstructed as $B^0 \to J/\psi\ K_L^0$, and B_{tag} as "tag-side" for the other B meson.

4.8.1 Vertexing algorithm

When we measure vertex point of B_{cp}, we use leptons from $J/\psi \to e^+e^-$ or $J/\psi \to \mu^+\mu^-$ decay. The decay vertex of J/ψ is identical to the vertex of the B meson. Because the lifetime of J/ψ is shorter than that of B meson. The efficiency of B_{cp} vertex reconstruction is measure about 95% using $B^+ \to J/\psi\ K^+$ and $B \to J/\psi\ K^{*0}(K^{*0} \to K^+\pi^-)$ event in experimental data. The resolution of B_{cp} vertex is estimated to be about 75 μm using Monte Carlo.

We measure the vertex point of B_{tag} by a extrapolation fit from well-reconstructed charged tracks in the tag-side. Tracks of $K_S^0 \to \pi^+\pi^-$ decay products are excluded. Because these tracks may give a bias to the vertex point being the flight length from the interaction point even if K_S^0 flight length is short. We also remove the tracks which χ^2 in the vertex fitting becomes large. When we select the events with reduces χ^2 of $\xi < 100$, the efficiency of B_{tag} vertex reconstruction is measure about 93% using the same sample of B_{cp}.

The B_{cp} and B_{tag} vertex points are required to be consisted with the profile of the interaction point.

4.8.2 Response function

We measure the decay time difference Δt between B_{cp} and B_{tag}. B meson pair is produced almost at rest in the $\Upsilon(4S)$ center of mass system. So Δt is determined from the distance between vertex points,

$$\Delta t \simeq \frac{\Delta z}{\gamma\beta c} = \frac{z_{cp} - z_{tag}}{\gamma\beta c}$$

where z_{cp} and z_{tag} are the z positions of the B_{cp} and B_{tag} decay vertices, respectively. The obtained is smeared by the fluctuation of beam energy depending on the experimental run conditions. We treat this smearing as resolution function, $R_{sig}(\Delta t)$, described later.

After vertex reconstruction and selection, p_B^* distribution for KLM and ECL candidates are shown in Figure 4.14. We can see a clear peak around nominal $p_B^* \approx 0.335\ GeV/c$ and tail backgrounds. We do not know the number of $B^0 \to J/\psi\ K_L^0$ signal events and background events at this time. Next we try to fit these histograms to know these number of events.

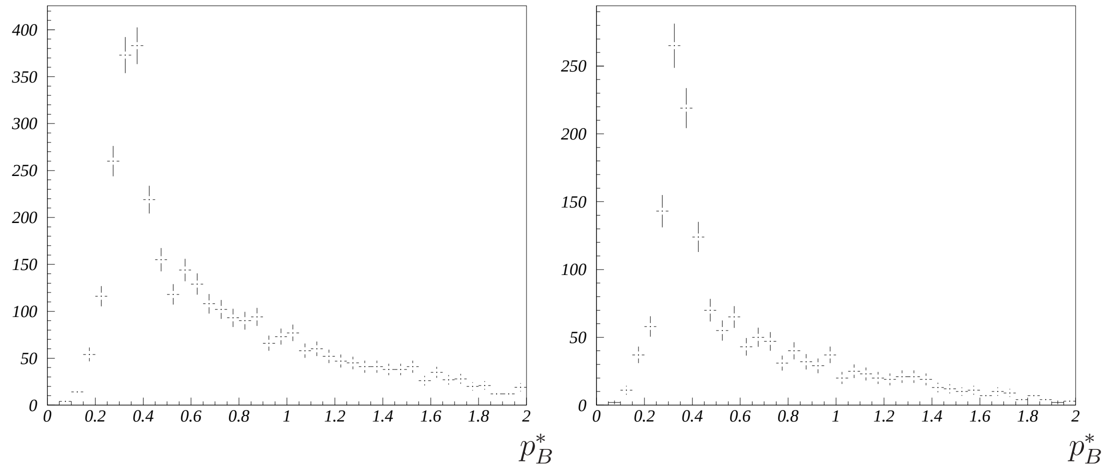

Figure 4.14: p_b^* distribution after vertexing. Left (Right) histogram is for KLM (ECL) candidate.

4.9 Background estimation

After all selection, we estimate the $B^0 \to J/\psi\ K_L^0$ signal purity, f_{sig}. We try a binned likelihood fit to p_B^* distribution for the reconstructed $B^0 \to J/\psi\ K_L^0$ candidates. In this fit, the events are categorize the four components as follows,

1 $B^0 \to J/\psi\ K_L^0$ signal events.

2 $B \to J/\psi\ X$ background events which includes real K_L^0 at final state.

3 $B \to J/\psi\ X$ background events which does not include real K_L^0 at final state.

4 Combinatorial J/ψ background events.

First three components are for the event which include real J/ψ in B decay, and fourth component is for the event which does not include real J/ψ. This means the J/ψ is reconstructed incorrectly. The leptons are misidentified and the invariant mass of two leptons is accidentally within the J/ψ mass region, and then this event pass the $B^0 \to J/\psi\ K_L^0$ event selection cuts. We call these events as fake J/ψ backgrounds.

For fitting to the p_B^* distribution, we float the parameters of the first to the third components, and also float $B^0 \to J/\psi\ K_L^0$'s p_B^* peak position. But we fix the fourth component. How to determine the p_B^* shape for each component and to fix the fake J/ψ backgrounds are described in the following subsections.

4.9.1 Fake J/ψ backgrounds

The p_B^* distribution shape and the normalization factor for the fake J/ψ backgrounds are estimated from experimental data. In order to estimate the number of fake J/ψ backgrounds, we use J/ψ mass sideband date. Figure 4.15 shows the invariant mass distributions for the reconstructed J/ψ after all selection, except J/ψ mass selection.

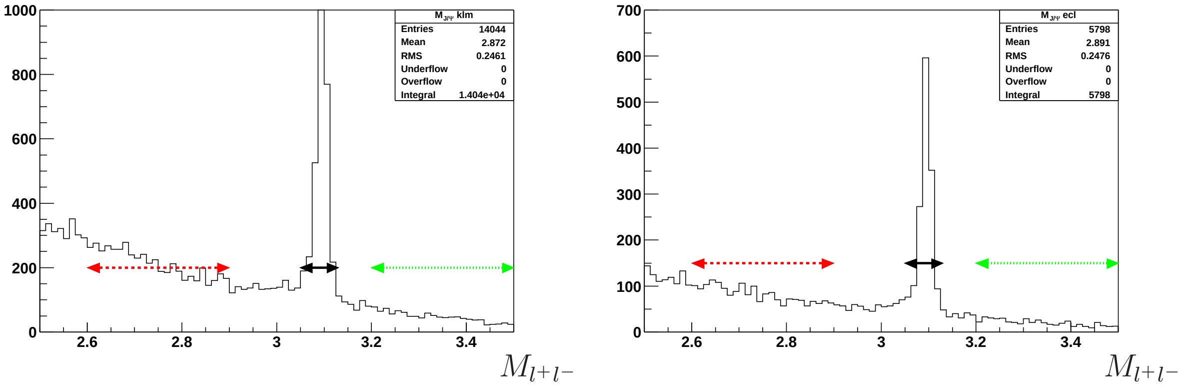

Figure 4.15: Invariant mass distributions for J/ψ. Black arrow region shows signal region, and red (green) arrow region shows J/ψ mass sideband "lower" ("higher") region.

Normalization of fake J/ψ backgrounds

In order to estimate the normalization factor of fake J/ψ backgrounds, we fit the Gaussian to the reconstructed J/ψ invariant mass distribution. Figure 4.16 shows J/ψ invariant mass fit result. When we fit J/ψ invariant mass, we use sum of two functions which are crystal-ball function for real J/ψ event and linear function for combinatoric background. The normalization factor for each KLM and ECL candidate are defined by the ratio of the number of fake J/ψ events to the sum of fake and real J/ψ events in signal J/ψ mass region, $3.05 < M_{l^+l^-} < 3.13\ GeV/c^2$.

p_B^* shape of fake J/ψ backgrounds

In order to estimate the p_B^* shape of fake J/ψ backgrounds, we use the reconstructed J/ψ mass sideband data which the experimental data are reconstructed after all selection except J/ψ mass selection. The definition of J/ψ mass sideband region is $2.6 < M_{l^+l^-} < 2.9\ GeV/c^2$ or $3.2 < M_{l^+l^-} < 3.5\ GeV/c^2$. When we calculate the p_B^* shape of fake J/ψ backgrounds from the sum of events in lower and higher $M_{l^+l^-}$ sideband region. Figure 4.17 shows the p_B^* distribution of sum of $M_{l^+l^-}$ sideband date for the KLM and ECL candidates.

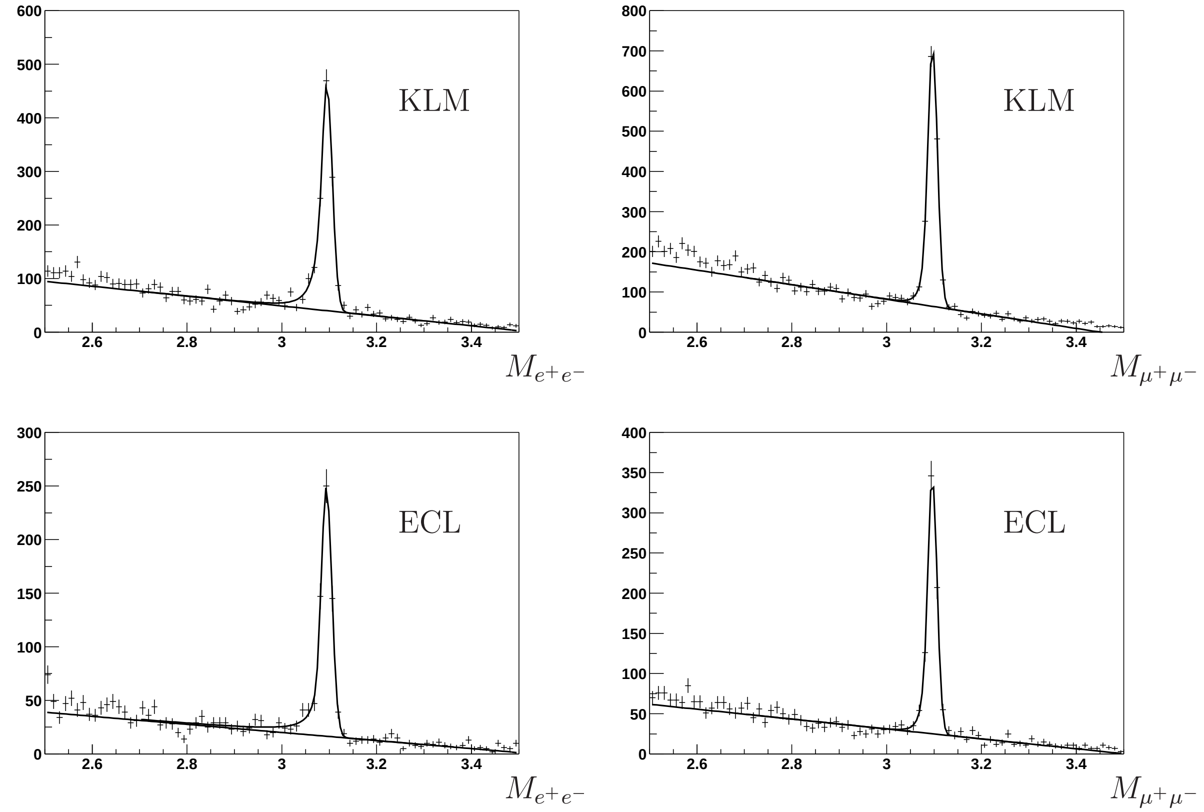

Figure 4.16: J/ψ mass fit result. Upper and Lower histograms are for KLM (ECL) candidates, and left (right) is for $J/\psi \to e^+e^-$ ($J/\psi \to \mu^+\mu^-$) decay mode.

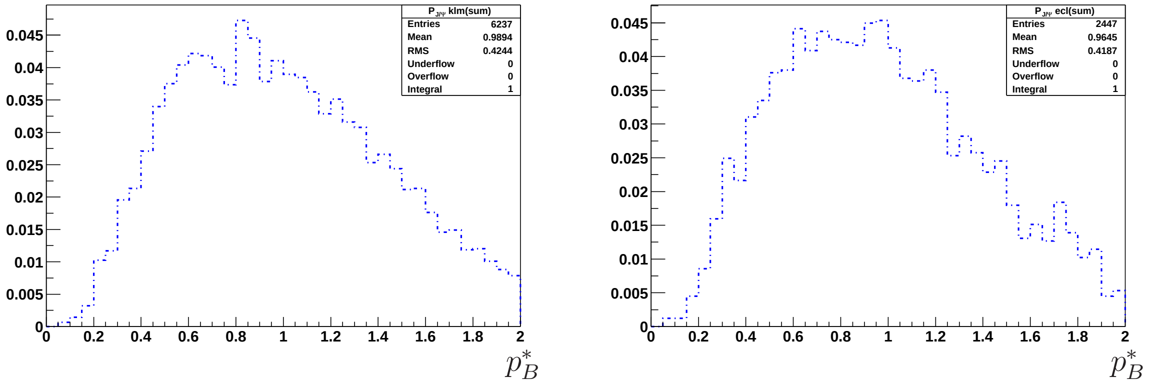

Figure 4.17: p^*_B shape for J/ψ mass sideband data. Left (Right) histogram is for KLM (ECL) candidates.

Sideband data check

We estimate p_B^* shape by using J/ψ mass sideband data. It is necessary to investigate credibility that the p_B^* shape for J/ψ mass sideband data is the same as that of signal region. In order to check it, we use generic B decay Monte Carlo and continuum Monte Carlo for backgrounds. The generic B decay Monte Carlo is both B meson decay into generic modes, involving CP-eigenstate. The continuum Monte Carlo is $e^+e^- \to q\bar{q}$, where q is u, d, s and c quark. We use $e^+e^- \to c\bar{c}$ Monte Carlo for continuum background. Because u, d, s quarks is too light to reconstruct J/ψ, we can not reconstruct $B^0 \to J/\psi\ K_L^0$ event in $e^+e^- \to u\bar{u}, d\bar{d}, s\bar{s}$ backgrounds. So, the number of these event is too smaller than generic B decay and $e^+e^- \to c\bar{c}$ background events. Hence we ignore these backgrounds. We also reject the event whose reconstructed J/ψ is reconstructed correctly. Figure 4.18 shows reconstructed J/ψ mass distributions. In the figure, real J/ψ events from B decay Monte Carlo are excluded to test p_B^* shape of background. In order to increase statistics for signal yield, we expand the signal region as defined with $2.9 < M_{l^+l^-} < 3.2\ GeV/c^2$. The definition of lower-side and higher-side are the same as that of normalization section.

In order to check sideband data consistency, we examine the p_B^* shapes from J/ψ mass lower and higher side for each of Monte Carlo and experimental data. We also compare the sum of p_B^* shapes from J/ψ mass lower and higher sideband with p_B^* shape of backgrounds within signal region.

When we check the consistency or difference, we use chi-square test and Kolmogorov-Smirnov test (K-S test). In the case of chi-square test, we define χ^2 as,

$$\chi^2 = \sum_i \frac{R_i - S_i}{R_i + S_i}$$

where R_i and S_i are i-th bin's data of R and S histograms, respectively. In K-S test case, by using accumulation frequency function, $S_N(x)$, we define amount of K-S statistics as,

$$D = \max_{-\infty < x < +\infty} |S_{N_1}(x) - S_{N_2}(x)|$$

where $S_{N_1}(x)$ and $S_{N_2}(x)$ are the accumulation frequency function for each data sample. The following function form is used for calculation of significant establishment.

$$Q_{KS}(\lambda) = 2 \sum_{j=1} \infty (-)^{j-1} e^{-2j^2\lambda^2}.$$

This is a monotonically increasing function and a limit value is the following,

$$Q_{KS}(0) = 1, Q_{KS}(\infty) = 0.$$

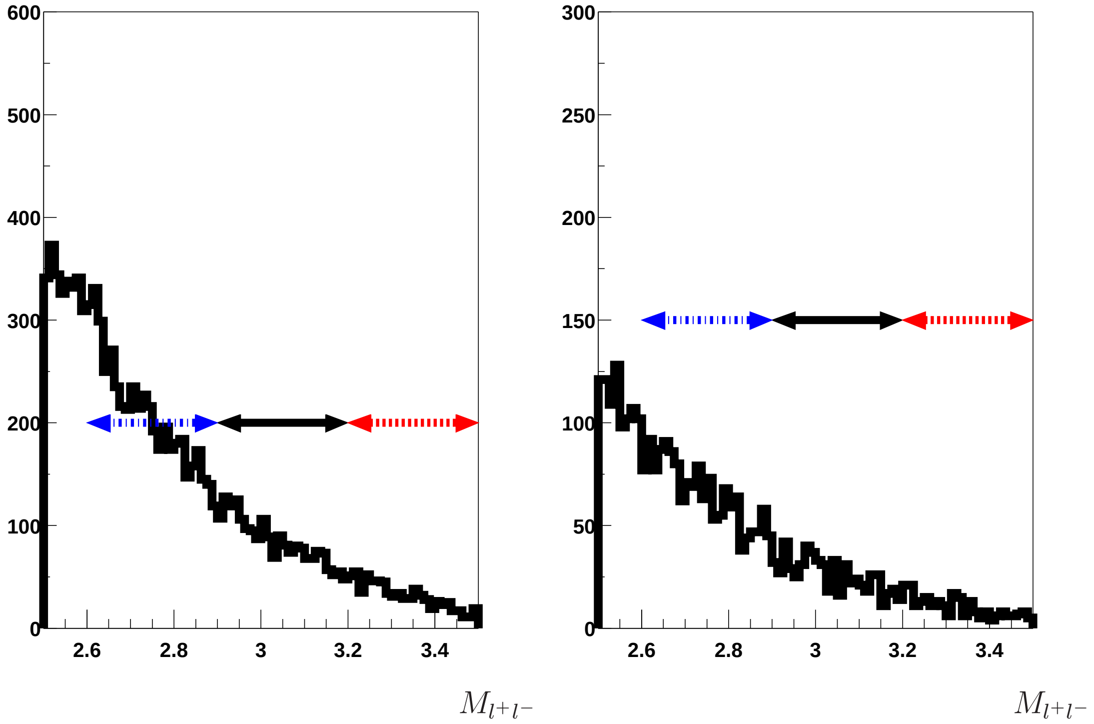

Figure 4.18: Reconstructed J/ψ mass distribution in Monte Carlo. Black arrow shows signal region, blue arrow lower-side region and red arrow higher-side region. Left (Right) distribution is for KLM (ECL) candidate.

We define the probability when we could observe D as the following equation,

$$Probability(D > observed) = Q_{KS}\left(\sqrt{\frac{N_1 N_2}{N_1 + N_2}} D\right).$$

First we check the difference of p_B^* shape between J/ψ mass lower and higher side in Monte Carlo. Figure 4.19 shows the p_B^* distributions and $P(x)$ distributions for each region. These turns out that two distributions have the same form in the shape. The results of this tests are shown in Table 4.2. There is no difference between two regions in Monte Carlo.

	KLM candidate	ECL candidate
χ^2/ndf	$38.703/39 = 0.992384$	$27.75/39 = 0.711539$
Probability(D)	$P(0.05) = 1$	$P(0.05) = 1$

Table 4.2: χ^2 and K-S test result of the difference between lower and higher side in Monte Carlo.

Second we check the difference between the sum of lower and higher sideband p_B^* shape and the p_B^* shape within signal region in Monte Carlo. Figure 4.20 shows the p_B^* distributions and $P(x)$ distributions for each region. From these distributions, it is also turned out that two distributions are same in the shape. The results of this tests are shown in Table 4.3. There is no difference between the background in signal region and the background sum in two sideband regions.

	KLM candidate	ECL candidate
χ^2/ndf	$31.9277/39 = 0.81866$	$29.8519/39 = 0.765433$
Probability(D)	$P(0.025) = 1$	$P(0.025) = 1$

Table 4.3: χ^2 and K-S test result of the difference between the background in signal region and the background sum in lower- and higher-sideband in Monte Carlo.

From Monte Carlo study, we can conclude that there is no difference in each region. Hence we can use the sum of J/ψ mass sideband data as combinatoric background for the signal region. Next we check this thing using experimental data. Figure 4.21 shows the reconstructed J/ψ mass distributions. We can see a clear peak at J/ψ mass position. The definition of lower-sideband and higher-sideband is the same as that of Monte Carlo study. We can not reject any event because we do not know the B meson decay type in real.

Third, we check the p_B^* shapes from J/ψ mass lower and higher sideband events in experimental data. Figure 4.22 shows the p_B^* distributions and $P(x)$ distributions for each region. These also turns out that two distributions have the same form

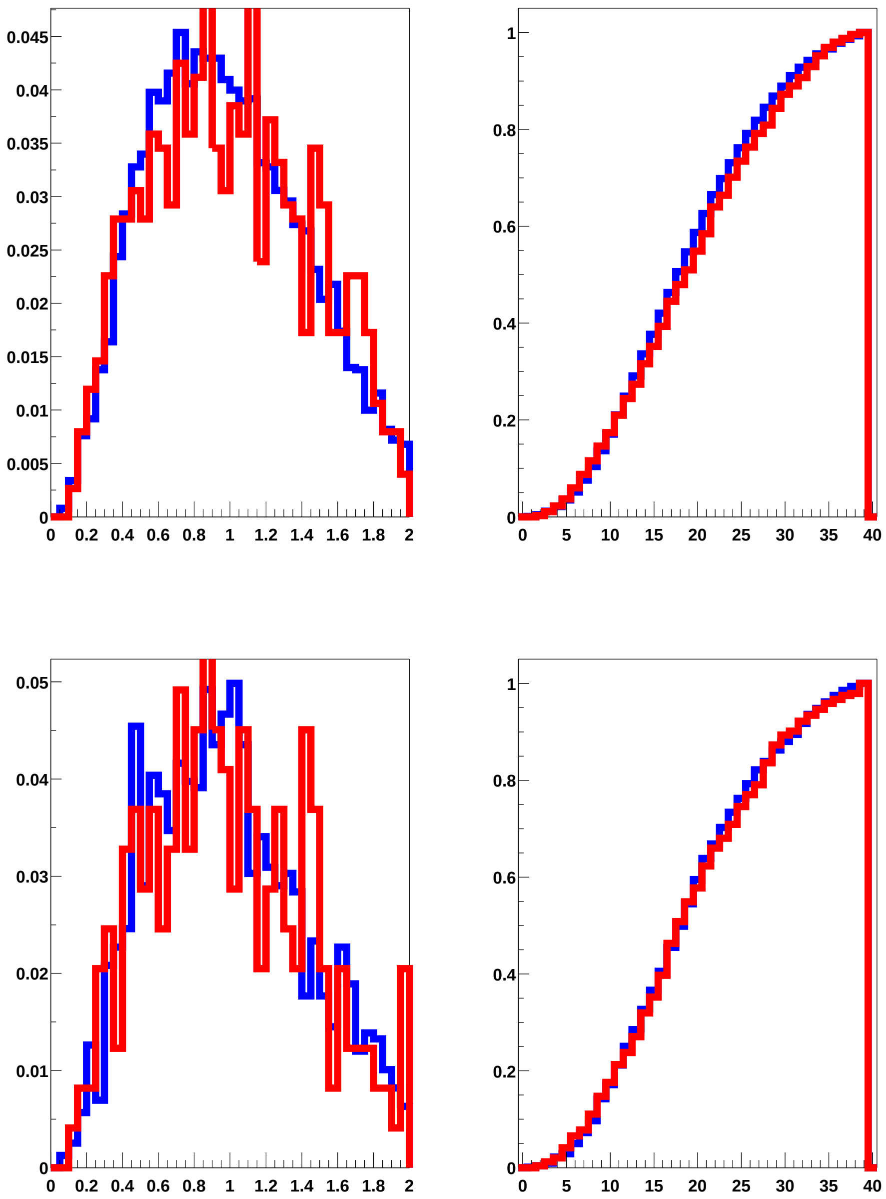

Figure 4.19: Reconstructed B meson's momentum distributions (left) in CMS and probability distribution (right) due to accumulation frequency function for K-S test in Monte Carlo. Upper (Lower) distributions are for KLM (ECL) candidate. Blue and red histograms are for the lower side and the higher side region, respectively

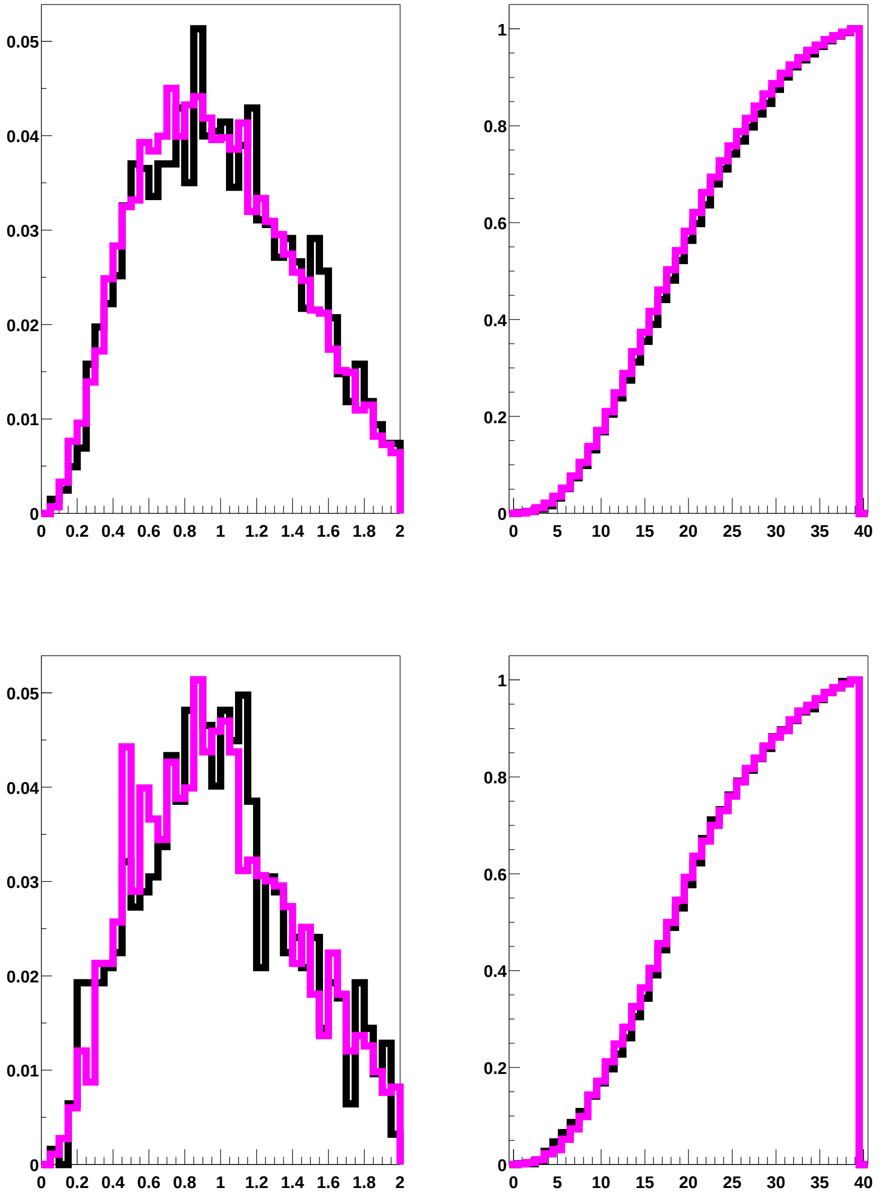

Figure 4.20: Reconstructed B meson's momentum distribution (left) in CMS and probability distribution due to accumulation frequency function for K-S test (right) in Monte Carlo. Upper (Lower) distributions are for KLM (ECL) candidate. Black and purple histograms are for the signal region and the sum of lower and higher sideband regions.

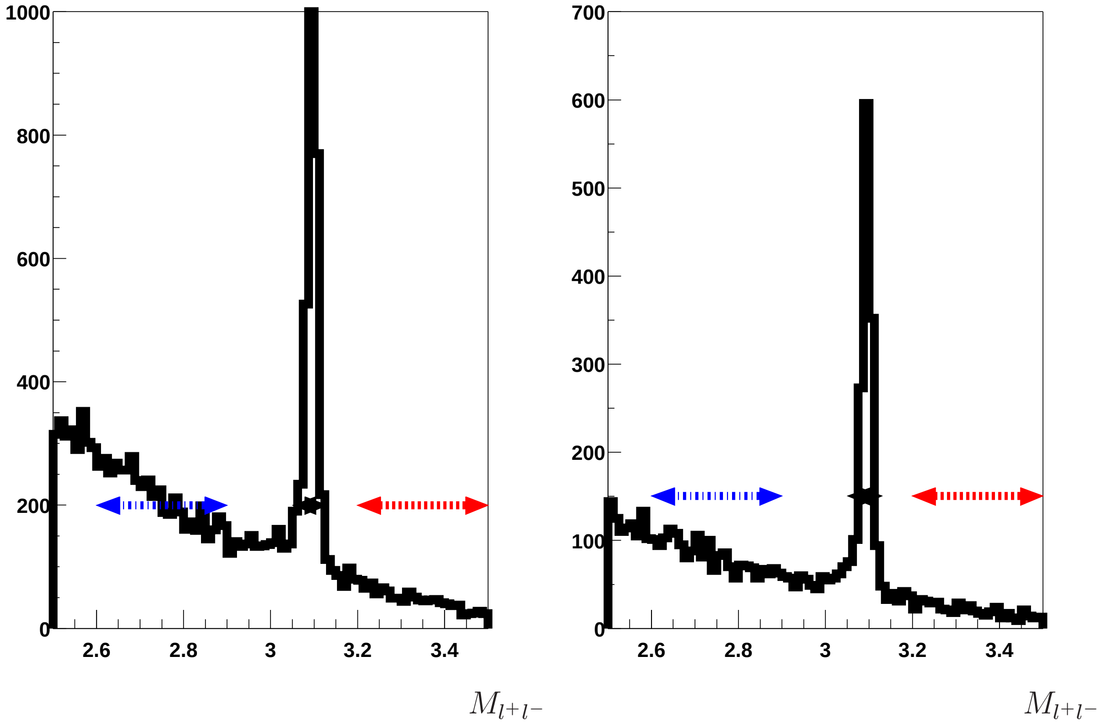

Figure 4.21: Reconstructed J/ψ mass distribution in experimental data. Black, blue, and red arrows show signal region, lower-sideband and red higher-sideband region. Left (Right) distribution is for KLM (ECL) candidate.

	KLM candidate	ECL candidate
χ^2/ndf	$24.7907/39 = 0.63566$	$41.5993/39 = 1.06665$
Probability(D)	$P(0.05) = 1$	$P(0.05) = 1$

Table 4.4: χ^2 and K-S test result of the difference between the lower side and the higher side in experimental data.

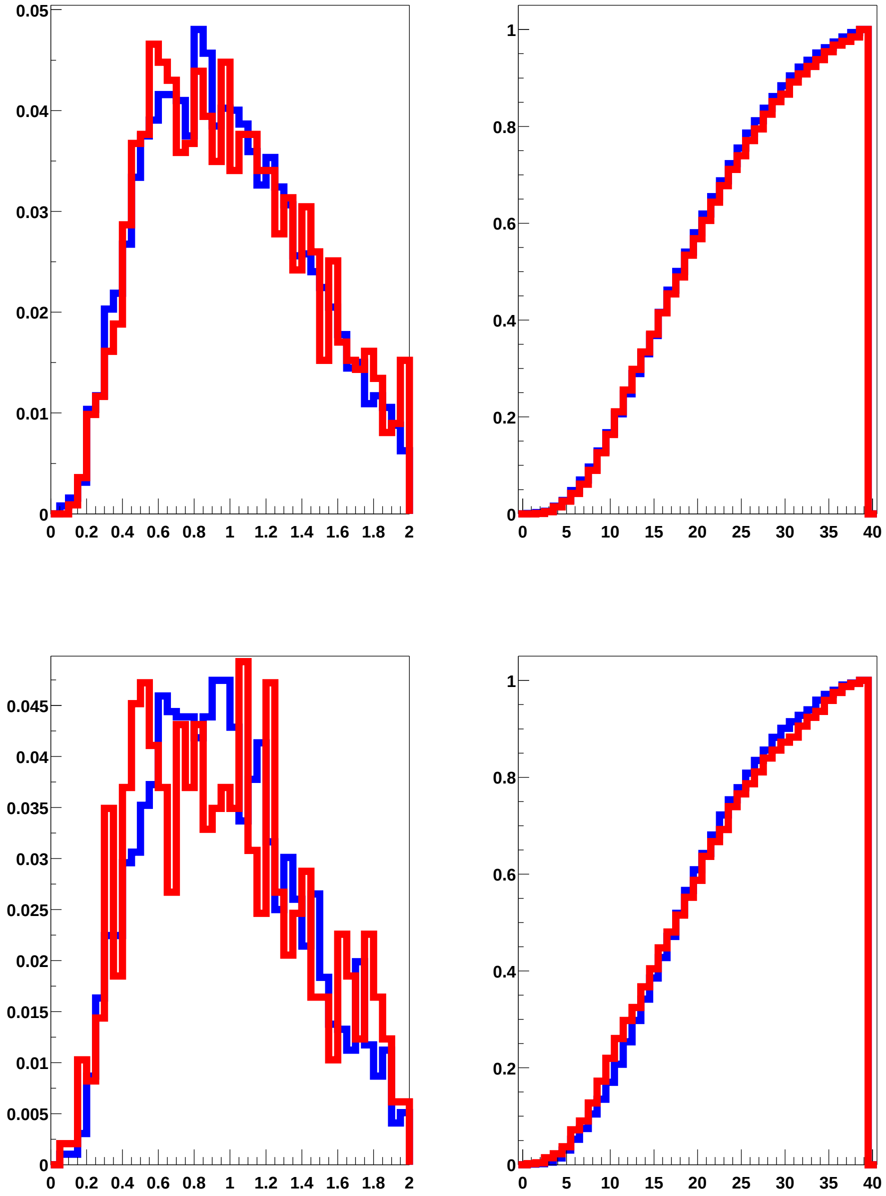

Figure 4.22: Reconstructed B meson's momentum distributions (left) in CMS and probability distributions (right) due to accumulation frequency function for K-S test in experimental data. Upper (Lower) distributions are for KLM (ECL) candidate. Blue and red histograms are for the lower side and higher side region, respectively.

in the shape. And the Results of this tests are shown in Table 4.4. There is no difference between the backgrounds in two regions.

Finally, we check the difference of p_B^* shapes for the sum of J/ψ mass sideband data between experimental data and Monte Carlo. Figure 4.23 shows the p_B^* distributions and $P(x)$ distributions for each sample. These also turns out that two distributions have the same form in the shape. The results of this tests are shown in Table 4.5. We can consider that there is no difference between experimental data and Monte Calro.

	KLM candidate	ECL candidate
χ^2/ndf	$33.4427/39 = 0.857504$	$36.7739/39 = 0.942921$
Probability(D)	$P(0.025) = 1$	$P(0.025) = 1$

Table 4.5: χ^2 and K-S test result in experimental data and Monte Carlo.

In the study of J/ψ mass sideband data from Monte Carlo and experimental data, we can conclude that there is no difference between Monte Carlo and experimental data in each region. Hence we can use the sum of J/ψ mass sideband data as combinatoric background for signal region from experimental data. Now, we know the normalization factor and p_B^* shape for fake J/ψ background from experimental data.

4.9.2 Real J/ψ backgrounds and signal $B^0 \to J/\psi\ K_L^0$ event

As the true K_L^0 efficiency is unknown, we need to define separately the shape of p_B^* for background which contains K_L^0 in final state or not. If any K_L^0 exists in final state, it is a $B \to J/\psi\ K_L^0\ X$ event. In this case, any of charged particle(s) or gamma(s) is missed for the event reconstruction. The p_B^* distribution for these events is wider and has larger tail than that of $B^0 \to J/\psi\ K_L^0$, but there may be a sharp peak around $p_B^* = 0.335\ GeV/c$ which is the nominal peak position for $B^0 \to J/\psi\ K_L^0$ events. On the other hand, if any K_L^0 does not exist in the final state, it means the reconstructed K_L^0 is the fake K_L^0 and only J/ψ is correct. In this case, there is not a sharp peak around $p_B^* = 0.335\ GeV/c$. Because we reconstruct the event assuming $B^0 \to J/\psi\ K_L^0$.

We obtain the p_B^* shapes with real J/ψ events from charmonium inclusive Monte Carlo. We also obtain the p_B^* shape for signal $B^0 \to J/\psi\ K_L^0$ event from Monte Carlo which one-side B meson decays into $B^0 \to J/\psi\ K_L^0$ and the other B meson decays into generic modes, selected from charmonium inclusive Monte Carlo. Figure 4.24 shows the p_B^* distributions for these three categories.

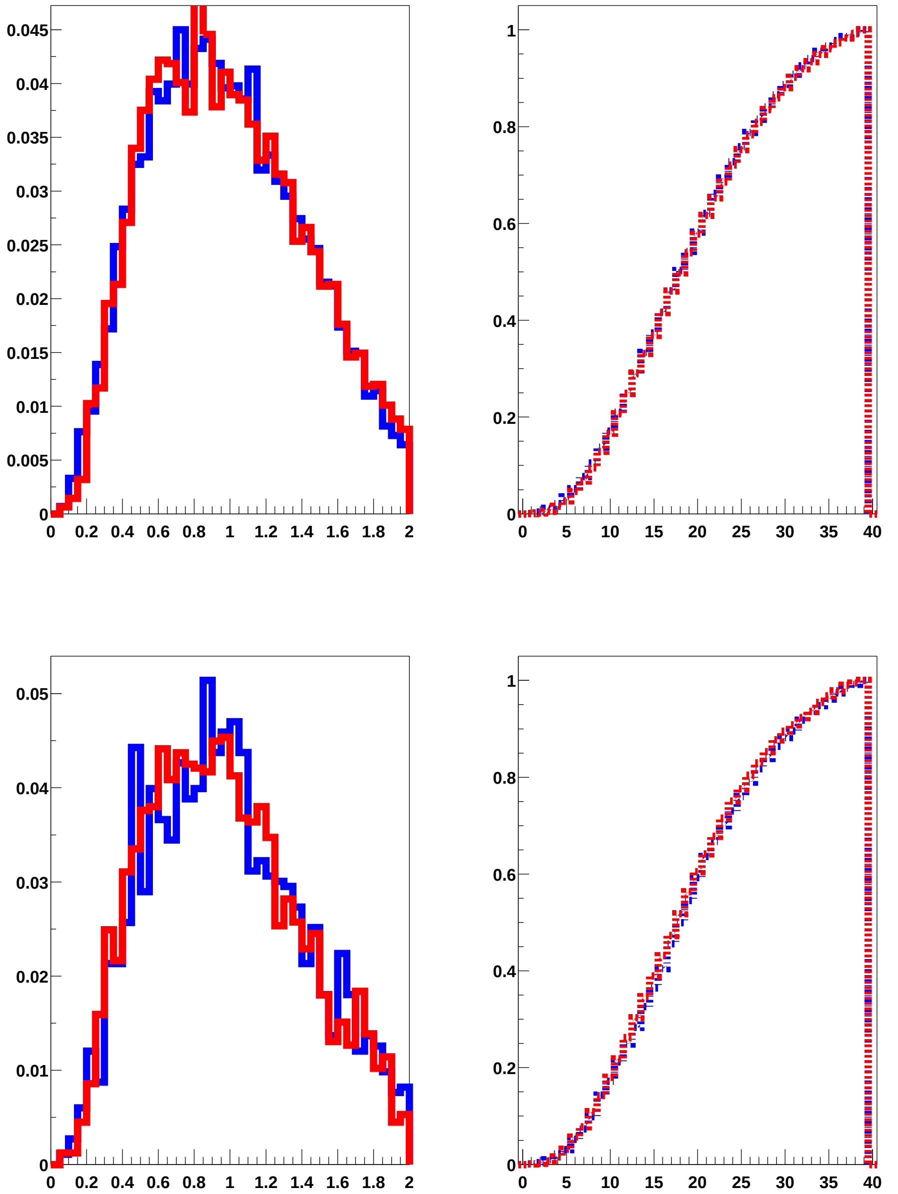

Figure 4.23: Reconstructed B meson's momentum distribution (left) in CMS and probability distributuin (right) due to accumulation frequency function for K-S test. Upper (Lower) distributions are for KLM (ECL) candidates. Blue and red histograms show the sum of lower and higher side regions obtained from experimental data and the Monte Carlo, respectively.

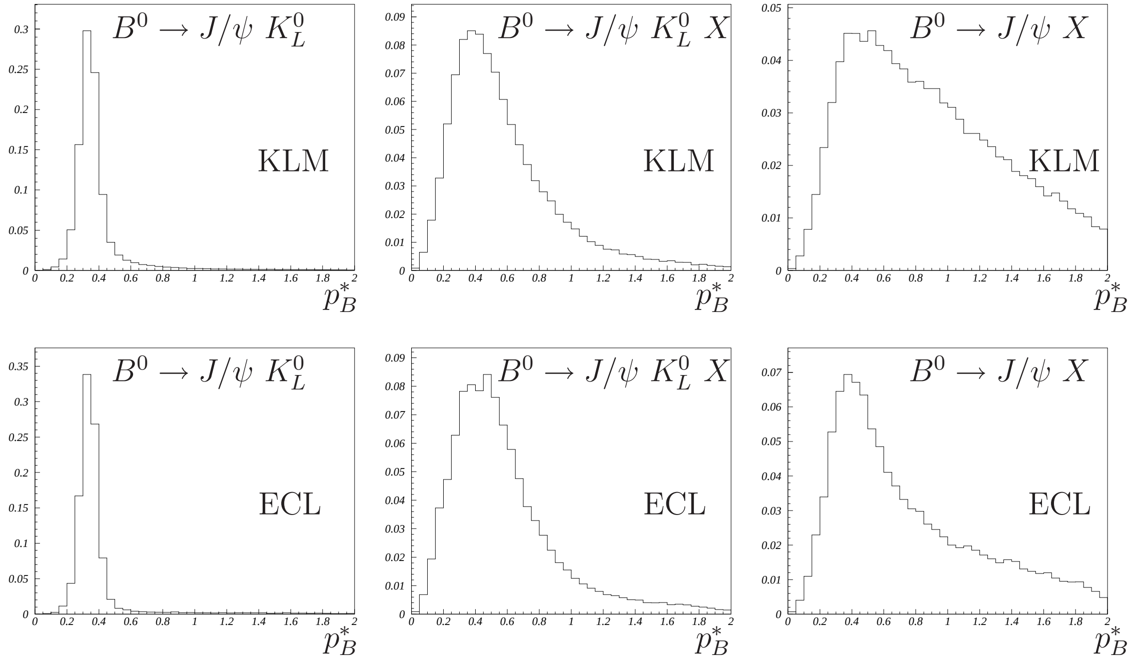

Figure 4.24: p_B^* distribution in Monte Carlo. Left, Middle, and Right histograms are $B^0 \to J/\psi\ K_L^0$ signal events, background events including real K_L^0, and background events not-including real K_L^0, respectively. Upper (Lower) distributions are for KLM (ECL) candidates.

Inclusive Monte Carlo check with true K_L^0

We consider the reconstructed K_L^0 is true K_L^0. The decay rate of $B^0 \to J/\psi\ K_L^0\ X$ and $B^0 \to J/\psi\ K_S^0\ X$ would be same, because CP-violation in the K-system is small. Thus we can reconstruct K_S^0 as K_L^0 because K_S^0 is modeled in the same way for K_L^0. We know more information in the case of K_S^0 than K_L^0. This allows us to positively identify K_S^0, as well as distinguish between $B^0 \to J/\psi\ K_S^0$ and $B^0 \to J/\psi\ K_S^0\ X$ in experimental data.

The p_B^* distribution would contain the same $B \to J/\psi\ K^0\ X$ background modes that we get in the $B^0 \to J/\psi\ K_L^0$ reconstruction. The backgrounds with true K_L^0 or K_S^0 can be expected to be the same in the two reconstruction, because the source and rate of fake K_L^0 and K_S^0 are different. If we want to get the same p_B^* distribution from $B^0 \to J/\psi\ K_S^0$ as $B^0 \to J/\psi\ K_L^0$, we need to apply the same event selection. The charged tracks from K_S^0 need to be intentionally ignored throughout the reconstruction, the number of charged tracks and $p_B^*(3)$ veto. The exclusive mode veto need to turn off, because these are not symmetric to K_S^0 and K_L^0. K_L^0 which detected fully/partially in the ECL can not be used, because the inclusive mode veto makes a use of the ECL energy. These would be no way to model for K_S^0. Figure 4.25 shows p_B^* of applying $B^0 \to J/\psi\ K_L^0$ selection without inclusive likelihood veto, and $B^0 \to J/\psi\ K_S^0$ case to mirror $B^0 \to J/\psi\ K_L^0$ from charmonium Monte Carlo sample. We can remove the fake $K^0(K_L^0$ and $K_S^0)$ and separate the signal event from the background event using generator information. The difference of p_B^* resolution in signal event ($B^0 \to J/\psi\ K_L^0$ and $B^0 \to J/\psi\ K_S^0$) is mainly due to the detector angular resolution of CDC and KLM. The remaining difference is due to a different momentum dependence in the detection efficiencies of K_L^0 and K_S^0. The background fraction in the K_S^0 case is larger, because the K_S^0 detection is extended to lower momentum than that of the K_L^0. Figure 4.26 shows the K_L^0 detection efficiency as a function of K_L^0 momentum.

In the $B^0 \to J/\psi\ K_L^0$ case, we can not separate the signal from the background and separate the true K_L^0 from the fake K_L^0 in experimental data. However, in $B^0 \to J/\psi\ K_S^0$ case, we can reject the fake K_S^0 in experimental data using K_S^0's energy. If we require $|\Delta E| < 50\ MeV$ and $5.27 < M_{bc} < 5.29\ GeV/c^2$ for the signal. After separating signal and background in Monte Carlo and experimental data, the p_B^* distributions from Monte Carlo and experimental data can be compared as shown in Figure 4.27.

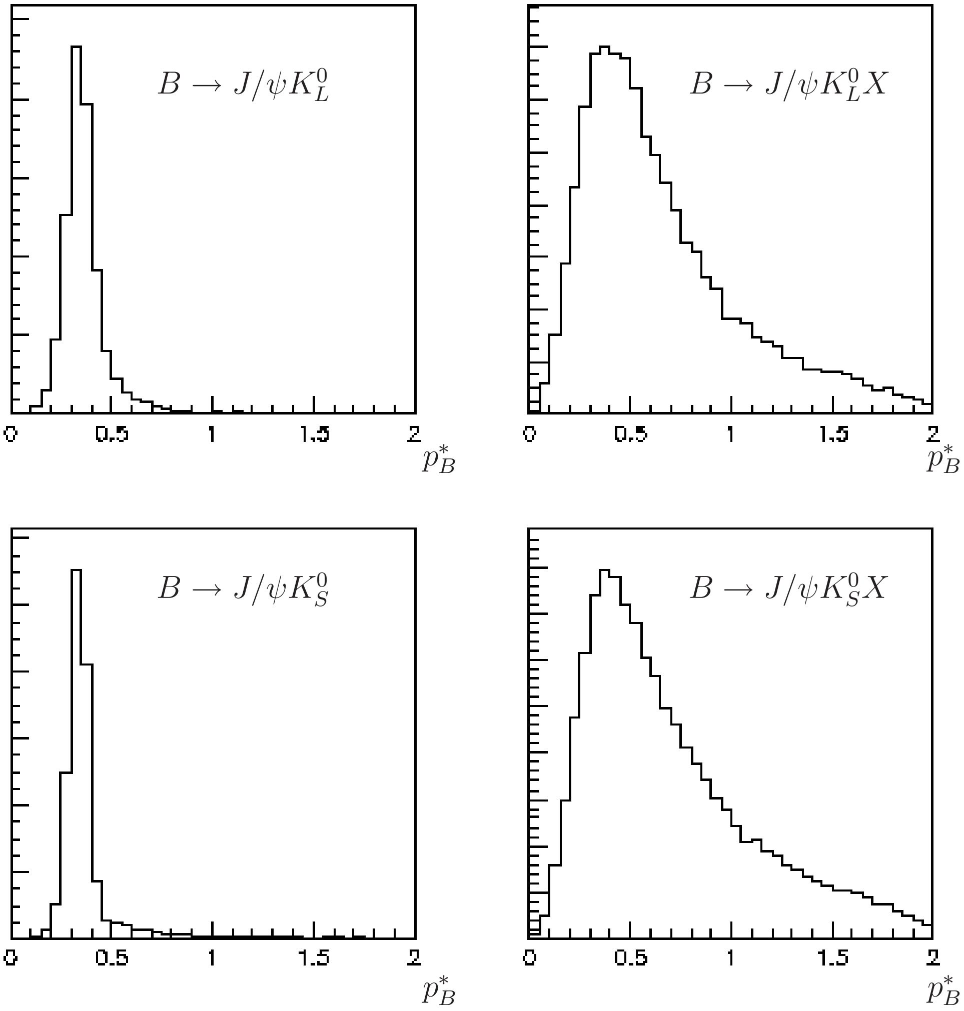

Figure 4.25: Comparison of p_B^* distribution between $B^0 \to J/\psi\ K_L^0$ (upper) and $B^0 \to J/\psi\ K_S^0$ (lower) candidate from charmonium inclusive Monte Carlo. Fake K_L^0 and K_S^0 events are removed using generator information. In order to model K_L^0, we do not use K_S^0's energy information.

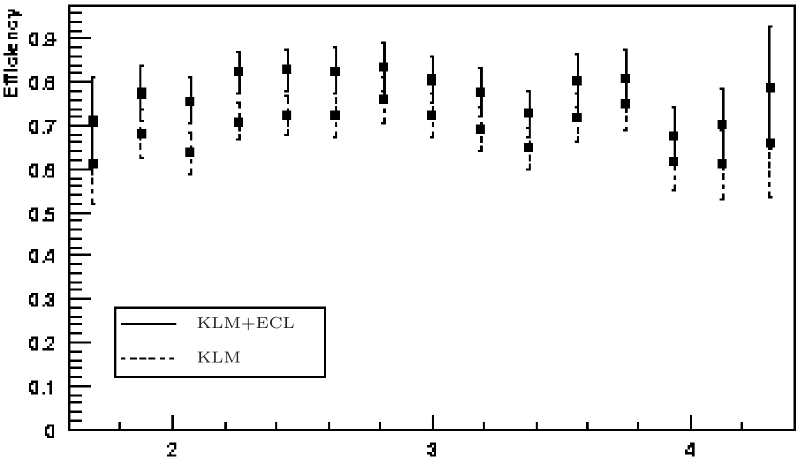

Monte Carlo

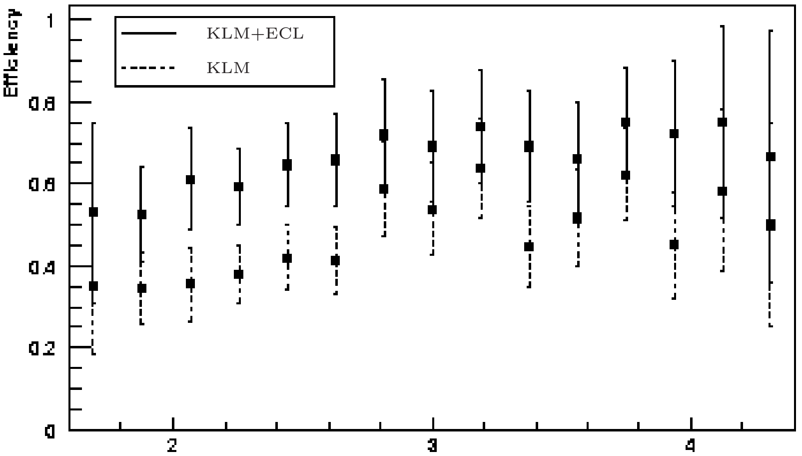

Experiment data

Figure 4.26: K^0_L detection efficiency versus K^0_L momentum, estimated from $e^+e^- \rightarrow \phi\gamma$ ($\phi \rightarrow K^0_L K^0_S$) in Monte Carlo and experiment data. In each plot, the Howe data points show the efficiency for events where the K^0_L left hits in the KLM detector, which includes events with hits in both the KLM and ECL. The upper data points includes called ECL-only events, where the K^0_L only left hits in the ECL. Note that in the momentum range below 2.7 GeV/c, which covers both signal and background in the $B^0 \rightarrow J/\psi\ K^0_L$ case, the KLM momentum dependence has the same tendency.

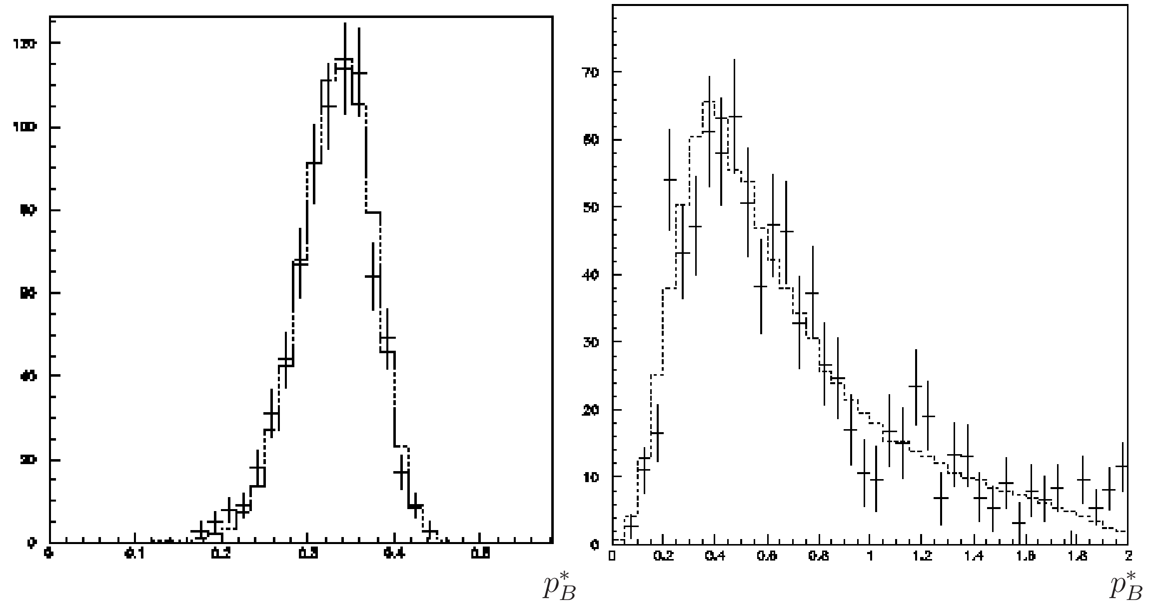

Figure 4.27: Comparison of p_B^* distribution between charmonium inclusive Monte Carlo (histogram) and experimental data (point with error). Left (Right) distribution is $B^0 \rightarrow J/\psi\ K_S^0$ signal (background) events. In order to mimic the $B^0 \rightarrow J/\psi\ K_L^0$ reconstruction, p_B^* of $B^0 \rightarrow J/\psi\ K_S^0$ is calculated without using K_S^0's energy information.

Inclusive Monte Carlo check with fake K_L^0

Next, we consider the case of the fake K_L^0 ($B^0 \to J/\psi\ K_L^0$) reconstructed. We can not get K_L^0's energy information. Hence we can not determine the fraction of fake K_L^0 ($B^0 \to J/\psi\ K_L^0$) although we can do for the fake J/ψ case (see Section 4.9.1). In order to estimate the fake K_L^0 ($B^0 \to J/\psi\ K_L^0$) background, we apply a method that we rotate the direction of K_L^0 candidates to the opposite direction of 180° around the beam axis before we reconstruct $B^0 \to J/\psi\ K_L^0$ event and calculate p_B^*. We just want to know only the shape of p_B^* distribution, not both the shape and the magnitude, but we need to know both for the fake J/ψcase. By rotating the K_L^0 direction, we can suppress the $B^0 \to J/\psi\ K_L^0$ candidates with the true K_L^0. The canditates are almost with the fake K_L^0 event. Thus, the background with the fake K_L^0 in Monte Carlo is compared to the background in experimental data. Figure 4.28 shows the p_B^* distributions from charmonium inclusive Monte Carlo and experimental data, with/without rotating K_L^0's direction.

When we measure the signal purity by fitting to p_B^* distribution (Section 4.10), we float the fake K_L^0's background normalization in order to take account of bias from the difference between Monte Carlo simulation and experiment data. Figure 4.29 and 4.30 shows the p_B^* distributions for $B^0 \to J/\psi\ K_L^0$ candidates from charmonium inclusive Monte Carlo and experimental data, when K_L^0 direction is rotated by 180°. The p_B^* shape from charmonium inclusive Monte Carlo matches the p_B^* shape from experimental data very well. An in-depth description can be found in [21].

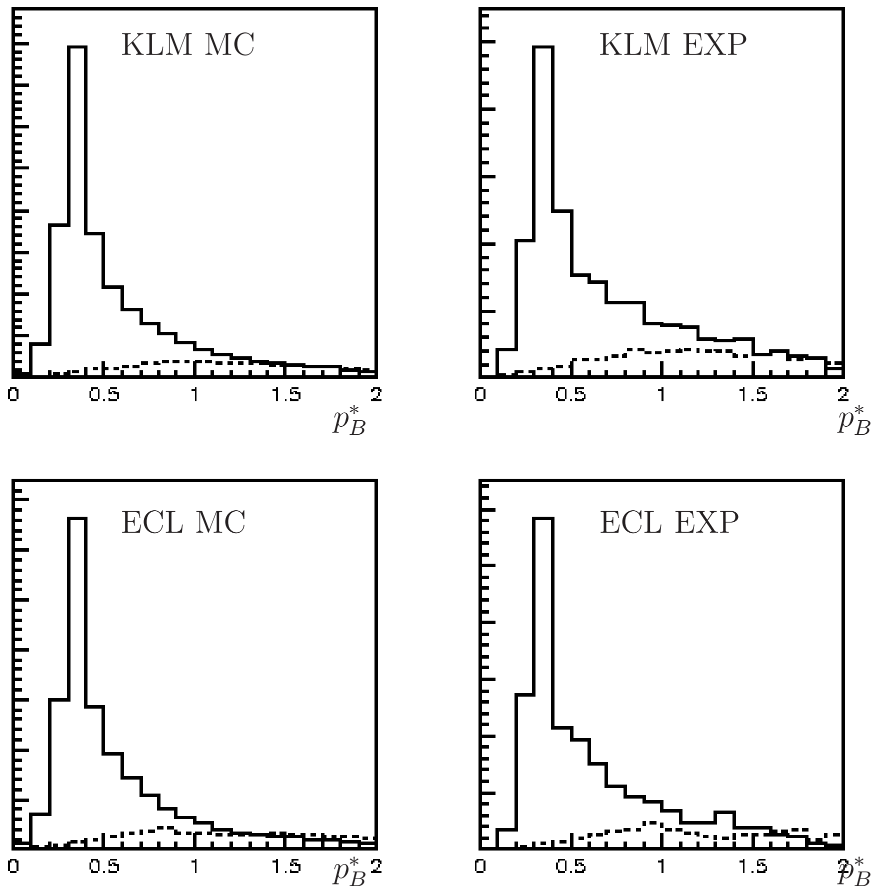

Figure 4.28: p_B^* distributions of $B^0 \to J/\psi\ K_L^0$ from charmonium Monte Carlo (left) and experimental data (right). Upper (Lower) histograms are candidates with KLM (ECL). The solid line histograms are result by nominal reconstruction and broken line histograms are result by reconstruction using rotated K_L^0.

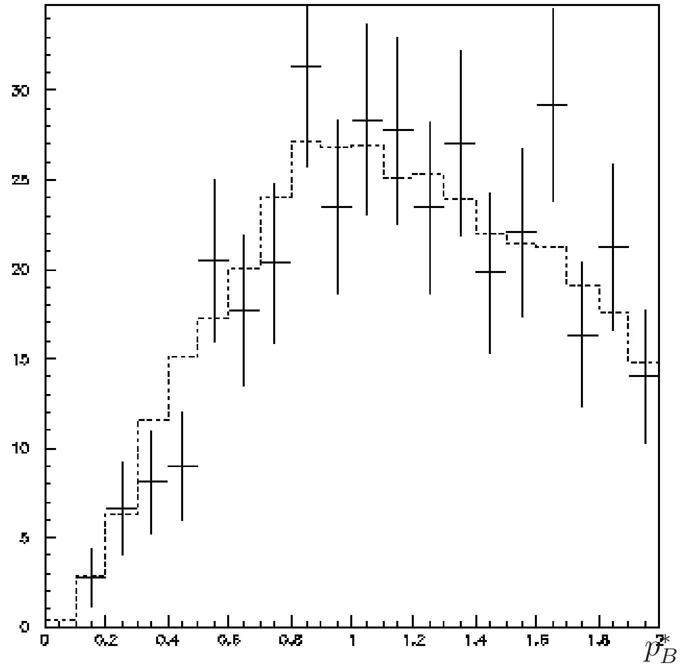

Figure 4.29: p_B^* distribution for $B^0 \to J/\psi\ K_L^0$ candidate with KLM form charmonium inclusive Monte Carlo (broken line histogram) and experimental data (points with errors). The direction of K_L^0 is rotated 180° around the beam axis before $B^0 \to J/\psi\ K_L^0$ reconstruction. This method suppresses real K_L^0's. The agreement between Monte Carlo and experimental data confirms that fake K_L^0 backgrounds are properly modeled in Monte Carlo.

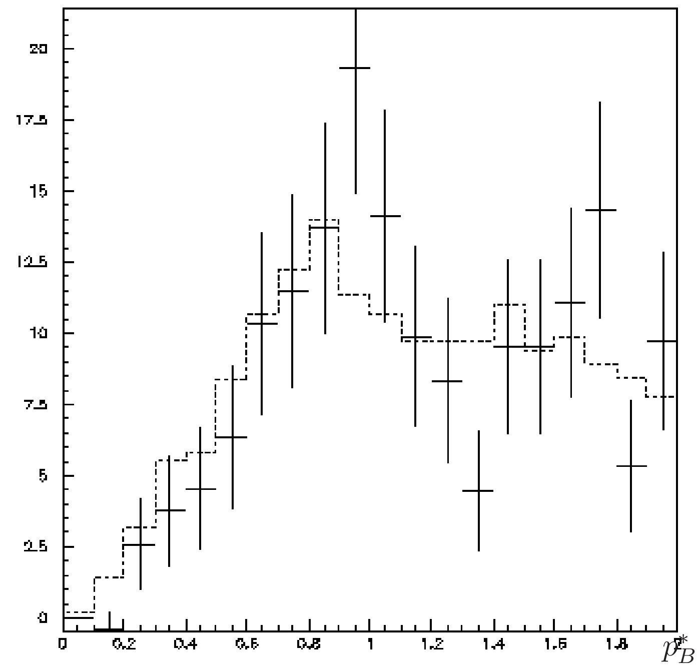

Figure 4.30: p_B^* distribution for $B^0 \to J/\psi\ K_L^0$ candidate with ECL form charmonium inclusive Monte Carlo (broken line histogram) and experimental data (points with errors). The direction of K_L^0 is rotated 180° around the beam axis before $B^0 \to J/\psi\ K_L^0$ reconstruction. This method suppresses real K_L^0's. The agreement between Monte Carlo and experimental data confirms that fake K_L^0 backgrounds are properly modeled in Monte Carlo.

4.10 p_B^* fit

Now, we have four component distributions for p_B^* fit, and we know the number of fake J/ψ events for each KLM and ECL candidate. For the fitting, we float the number of $B^0 \to J/\psi\ K_L^0$ events, backgrounds with true K_L^0 and backgrounds without K_L^0. The number of fake J/ψ is fixed. Fit result for KLM candidate is shown in Figure 4.31, and fit result for ECL candidate is shown in Figure 4.32. For the sum of KLM and ECL candidates, the fit result using $140/fb$ experimental data is shown in Figure 4.33.

We have 884.9 $B^0 \to J/\psi\ K_L^0$ events with purity about 61% for KLM candidates and 572.8 $B^0 \to J/\psi\ K_L^0$ events with purity about 66% for ECL candidate. The number of each component for all p_B^* region, $0 < p_B^* < 2.0\ GeV/c$, and signal p_B^* region, $0.2 < p_B^* < 0.45\ GeV/c$, are shown in Table 4.6.

	KLM cand $pb* < 2.0$	$0.2 < pb* < 0.45$
$J/\psi K_L^0$	1047.3 ± 60.36	884.86 ± 51.00
bkg w/ K_L^0	832.95 ± 118.3	310.09 ± 44.04
bkg w/o K_L^0	886.81 ± 98.34	164.42 ± 18.23
combinatoric	1075.8 ± 34.35	96.77 ± 3.089
purity($S/\sum N$)	0.27 ± 0.02	0.60 ± 0.03

	ECL cand $pb* < 2.0$	$0.2 < pb* < 0.45$
$J/\psi K_L^0$	639.18 ± 37.38	572.75 ± 33.495
bkg w/ K_L^0	488.74 ± 93.02	169.71 ± 32.30
bkg w/o K_L^0	266.61 ± 94.11	76.69 ± 27.07
combinatoric	446.78 ± 30.02	45.74 ± 3.073
purity($S/\sum N$)	0.35 ± 0.02	0.66 ± 0.04

Table 4.6: Fit result of $J/\psi K_L^0$ events

Figure 4.34 shows a typical $B^0 \to J/\psi\ K_L^0$ event at Belle detector. We can see dilepton which are J/ψ's daughters and K_L^0 cluster in KLM. Other tracks are B meson's decay products in the tag side.

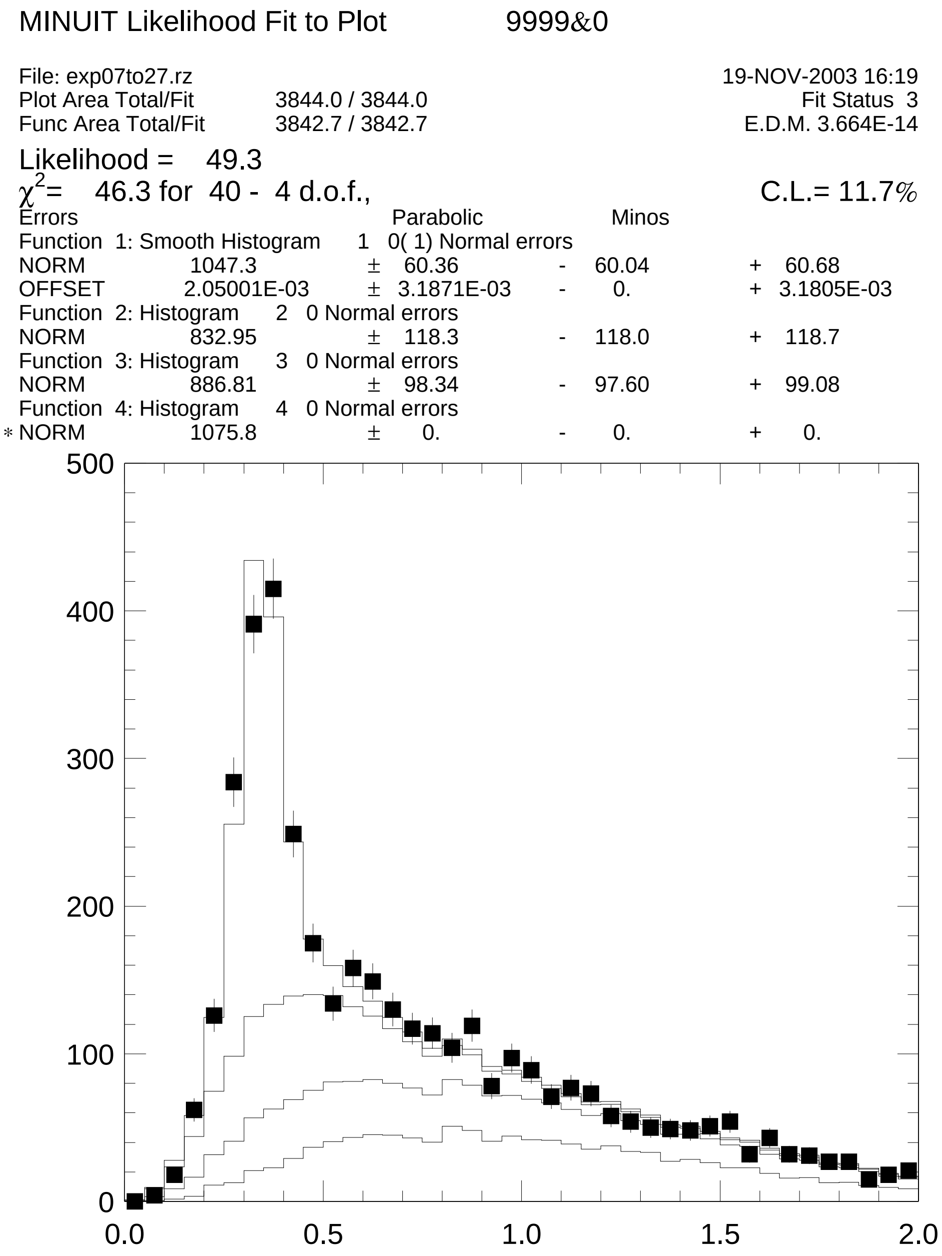

```
MINUIT Likelihood Fit to Plot           9999&0

File: exp07to27.rz                                           19-NOV-2003 16:19
Plot Area Total/Fit        3844.0 / 3844.0                        Fit Status  3
Func Area Total/Fit        3842.7 / 3842.7                    E.D.M. 3.664E-14
Likelihood =    49.3
χ2=    46.3 for  40 -  4 d.o.f.,                                 C.L.= 11.7%
Errors                                 Parabolic              Minos
Function  1: Smooth Histogram     1   0( 1) Normal errors
NORM              1047.3              ±    60.36         -   60.04          +   60.68
OFFSET          2.05001E-03           ±  3.1871E-03      -     0.           +  3.1805E-03
Function  2: Histogram     2   0 Normal errors
NORM              832.95              ±    118.3         -   118.0          +   118.7
Function  3: Histogram     3   0 Normal errors
NORM              886.81              ±    98.34         -   97.60          +   99.08
Function  4: Histogram     4   0 Normal errors
* NORM            1075.8              ±       0.         -     0.           +     0.
```

Figure 4.31: p_B^* fit result for KLM candidate after all selection

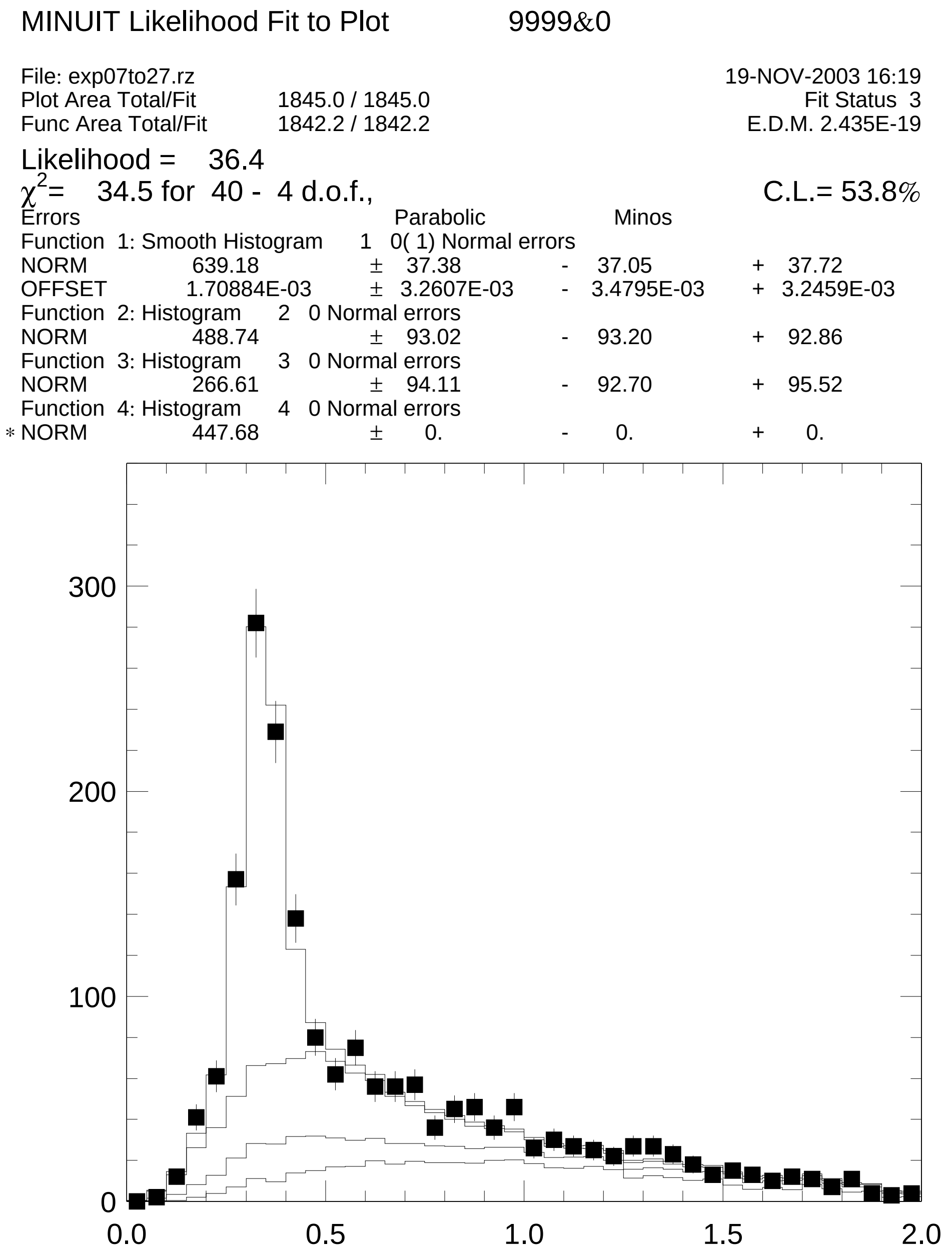

```
MINUIT Likelihood Fit to Plot              9999&0

File: exp07to27.rz                                              19-NOV-2003 16:19
Plot Area Total/Fit          1845.0 / 1845.0                          Fit Status  3
Func Area Total/Fit          1842.2 / 1842.2                       E.D.M. 2.435E-19
Likelihood =    36.4
χ2=    34.5 for  40 -  4 d.o.f.,                                     C.L.= 53.8%
Errors                                       Parabolic              Minos
Function  1: Smooth Histogram      1   0( 1) Normal errors
NORM              639.18             ±   37.38        -    37.05         +   37.72
OFFSET          1.70884E-03          ±  3.2607E-03    -   3.4795E-03     +  3.2459E-03
Function  2: Histogram     2   0 Normal errors
NORM              488.74             ±   93.02        -    93.20         +   92.86
Function  3: Histogram     3   0 Normal errors
NORM              266.61             ±   94.11        -    92.70         +   95.52
Function  4: Histogram     4   0 Normal errors
* NORM            447.68             ±      0.        -      0.          +     0.
```

Figure 4.32: p_B^* fit result for ECL candidate after all selection

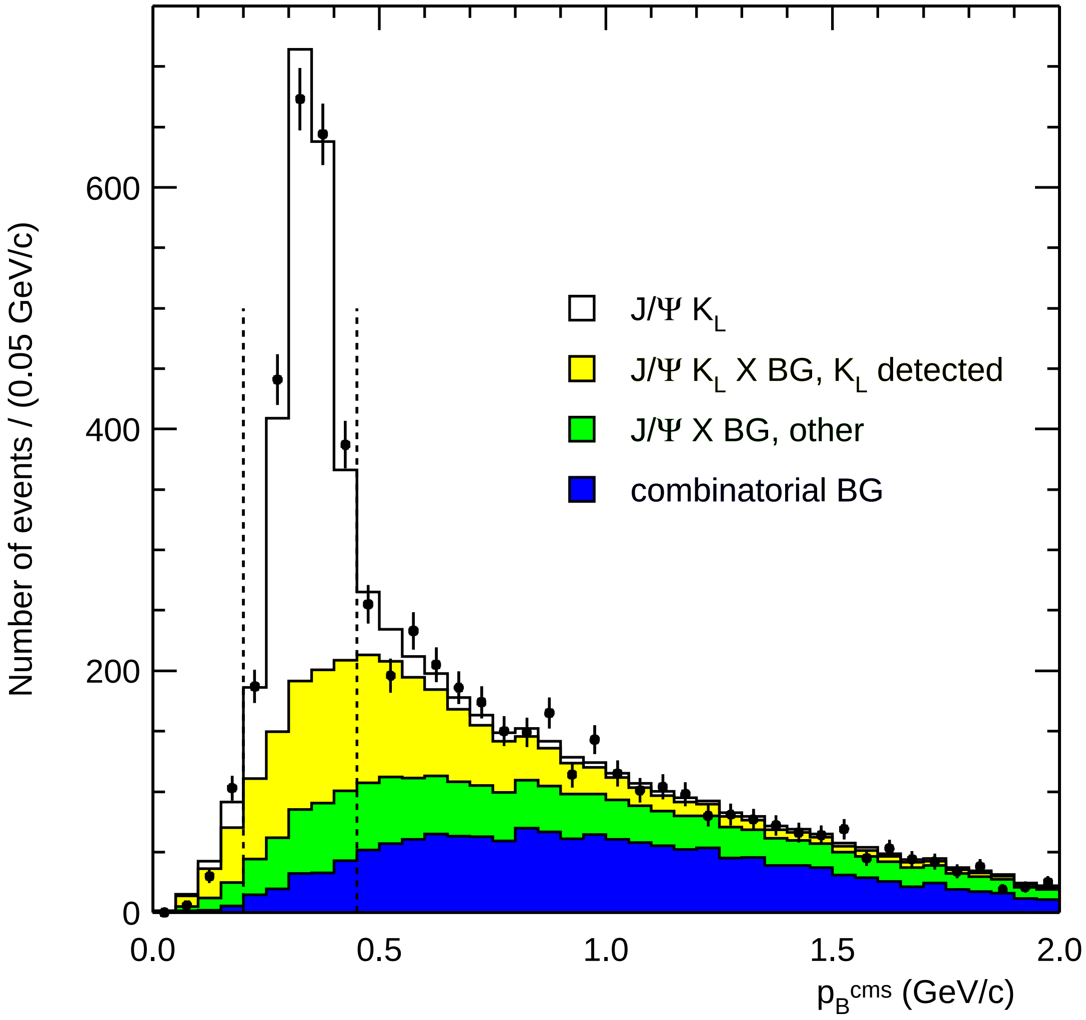

Figure 4.33: p_B^* fit result for sum of KLM and ECL candidates after all selection

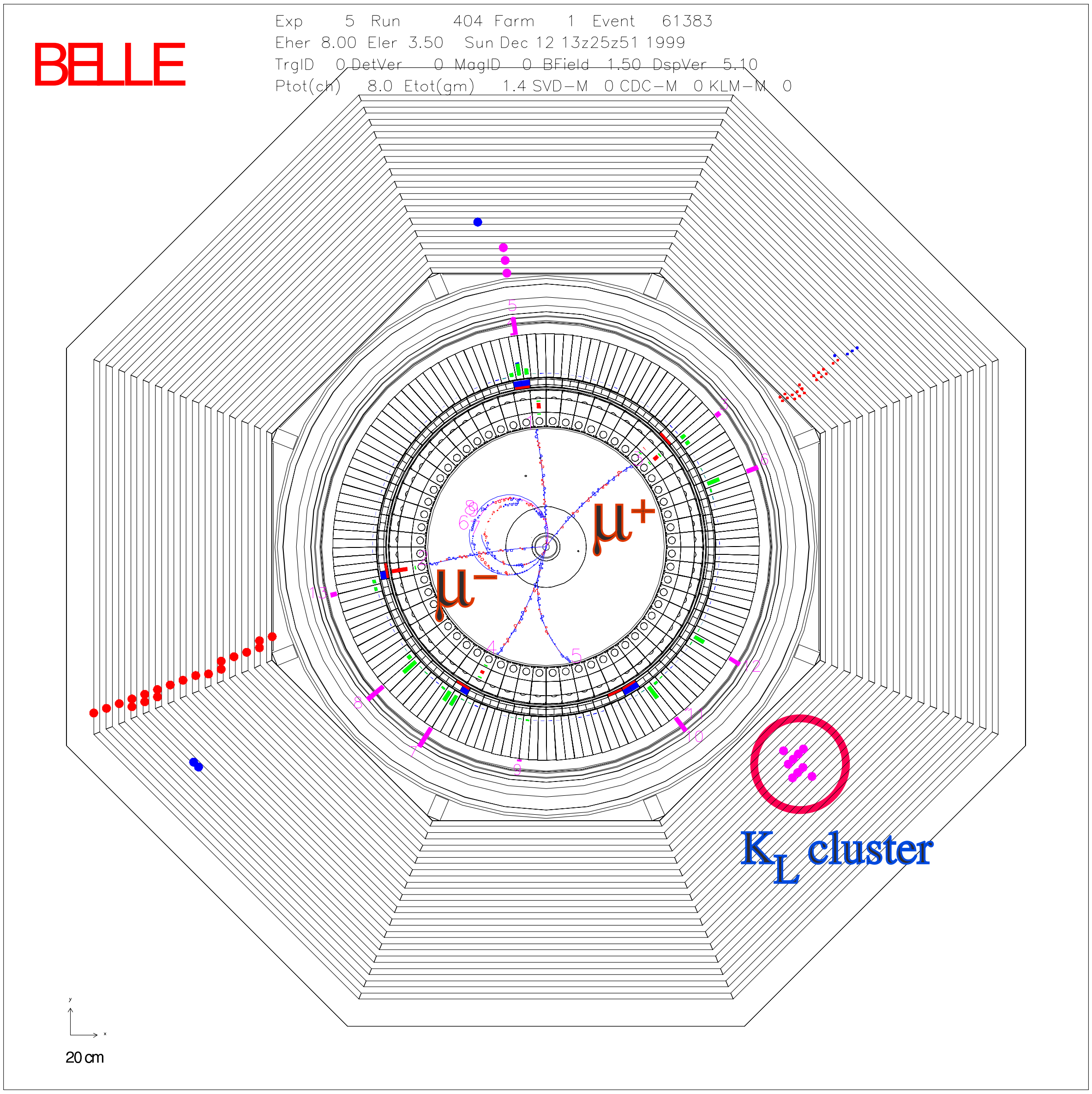

Figure 4.34: Typical $B^0 \to J/\psi\ K_L^0$ event display

Chapter 5

Measurement of $\sin 2\phi_1$

In this chapter we describe how to measure the CP-asymmetry parameter of $\sin 2\phi_1$. To observe $\sin 2\phi_1$, we need to identify the flavor of Bmeson and to introduce a probabibility density function.

5.1 Flavor tagging

As both B^0 and $\bar{B}^0$ can decay into a CP-eigenstate of $J/\psi\ K_L^0$, we can not distinguish the flavor of B^0 or $\bar{B}^0$ from the decay product. Now we call B_{cp} for the reconstructed $B(J/\psi K_L^0)$, and B_{tag} for the other B, $e^+e^- \to \Upsilon(4S) \to B_{cp}B_{tag}$. To observe the CP-asymmetry, we need to identify the reconstructed B flavor and to measure the decay time difference Δt between B_{cp} and B_{tag}. First we identify the flavor of not-reconstructed B, B_{tag}, using remaining tracks when we reconstruct $B^0 \to J/\psi\ K_L^0$. This is the same method which has been used for the previous $\sin 2\phi_1$ measurement [17].

5.1.1 Flavor tagging algorithm

In order to get a good tagging efficiency, we use all informations for tag-side tracks. We check for type of flavor from specific B decays, so called "track-level". Then we combined the informations of "track-level" and decide final flavor of B_{tag} value, so called "event-level". A schematic view of the algorithm is shown in Figure 5.1.

Some types of B decays are correlated with the flavor of B. Figure 5.2, 5.3 and 5.4 shows types of such as flavor specific B meson decay. To determine the B meson flavor, we use the following flavor specific B decays, so called "track-level",

1 High momentum leptons from $b \to c\ \mathbf{l}^-\nu$, shown in Figure 5.2.

2 Lower momentum leptons from cascade decay $b \to c \to s\ \mathbf{l}^+\nu$, shown in Figure 5.3.

3 Charged K and Λ from $b \to\ c \to\ \mathbf{s}$, shown in Figure 5.4.

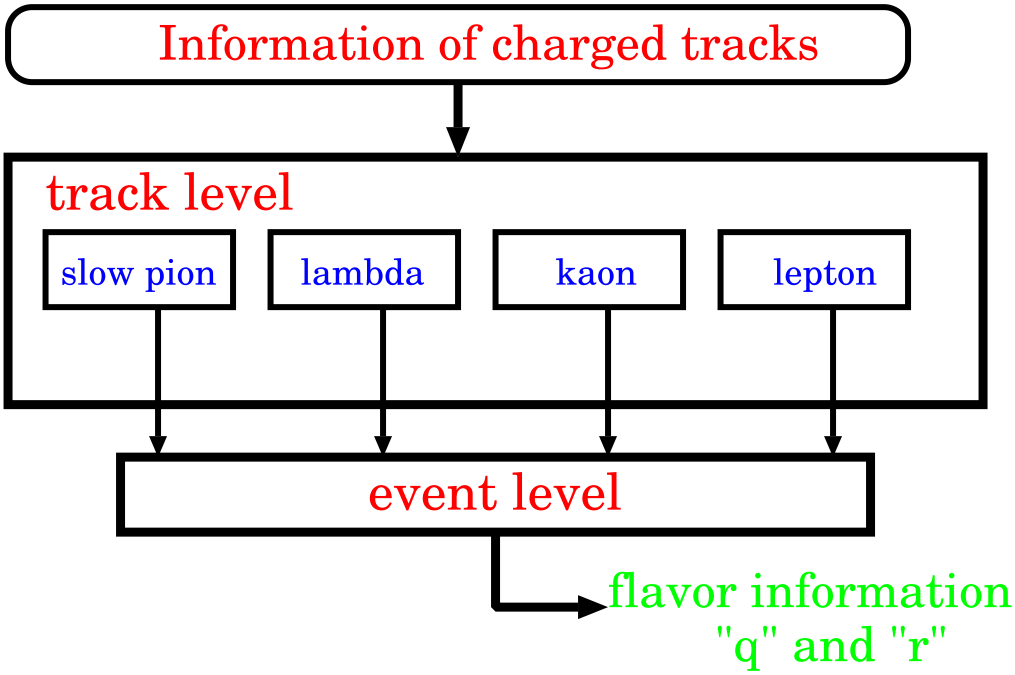

Figure 5.1: Schematic overview of the flavor tagging algorithm. “q” is the most likely flavor of B_{tag}, $+1$ or -1. “r” is the reliability of the flavor, $0 \sim 1$.

4 High momentum πs from $B^0 \to D^{(*)-} + (\pi^+, \rho^+, a_1^+, etc.)$.

5 Low momentum πs from $D^{*-} \to \bar{D}^0 + \pi^-$.

We use two parameters, q and r, to represent the tagging information. The q is the flavor having the discrete value $+1$ or -1 when the tag-side B meson is likely to be a B^0 or $\bar{B}^0$. The r gives the purity of flavor tagging as flavor-tagging dilution parameter with $r = 0 \sim 1$, $r = 0$ for no flavor discrimination and $r = 1$ for an unambiguous flavor assignment. It is used only to sort data into six intervals of r, according to estimated flavor purity. We determine directly from data the average wrong-tag probabilities, $w_l \equiv (w_l^+ + w_l^-)/2$ $(l = 1, 6)$, and differences between B^0 and $\bar{B}^0$ decays, $\Delta w \equiv w_l^+ - w_l^-$, where $w_l^\pm$ is the wrong-tag probability for the B^0 and $\bar{B}^0$ decay in each r interval.

5.1.2 Wrong tag fraction

We determine “wrong-tag fraction”, w_l, for each r bin from experimental data. To obtain w_l, we reconstruct the specific B decays of $B^0 \to D^{*-}l^+\nu, D^{(*)-}\pi^+, D^{*-}\rho^+$ and $\bar{B}^0 \to D^{*+}l^-\nu, D^{(*)+}\pi^-, D^{*+}\rho^-$. In these decay, we know B meson’s flavor from the decay products. Then we use flavor tagging algorithm on software for obtaining the other B meson’s flavor. Now, we have two flavor, flavor from B meson decay and

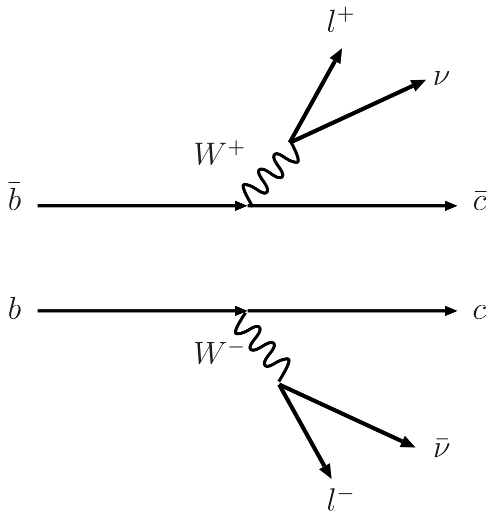

Figure 5.2: Semileptonic B decay, $b \rightarrow c\ \mathbf{l^+}\nu$, $\bar{b} \rightarrow \bar{c}\ \mathbf{l^-}\bar{\nu}$

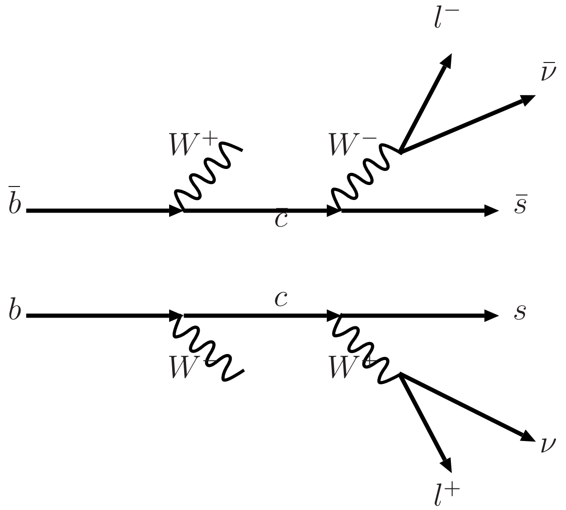

Figure 5.3: B meson cascade decay, $b \rightarrow c \rightarrow s\ \mathbf{l^-}\nu$, $\bar{b} \rightarrow \bar{c} \rightarrow \bar{s}\ \mathbf{l^+}\bar{\nu}$

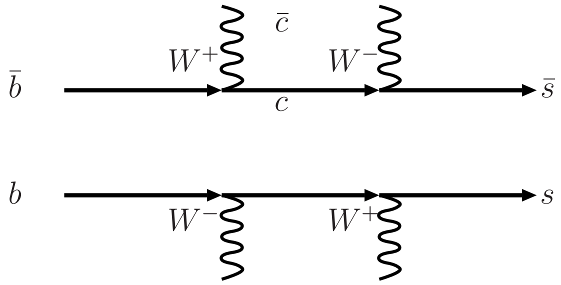

Figure 5.4: B meson cascade decay, $b \rightarrow c \rightarrow s$, $\bar{b} \rightarrow \bar{c} \rightarrow \bar{s}$

software level. So, we can separate sample into two categories that B meson has the same flavor (SF) or opposite flavor (OF). The time dependent mixing asymmetry of such events is given by

$$A(\Delta t) = \frac{P_{OF} - P_{SF}}{P_{OF} + P_{SF}} = (1 - 2w_l)\cos(\Delta m_d \Delta t).$$

Figure 5.5 and 5.6 show the reconstructed $\cos\theta_{B(D^*l\nu)}$ and M_{bc} and ΔE for $D^{(*)}\pi$, $D^*\rho$, $J/\psi K^{(*)}$. Figure 5.7 shows $A(\Delta t)$ distributions for each r interval.

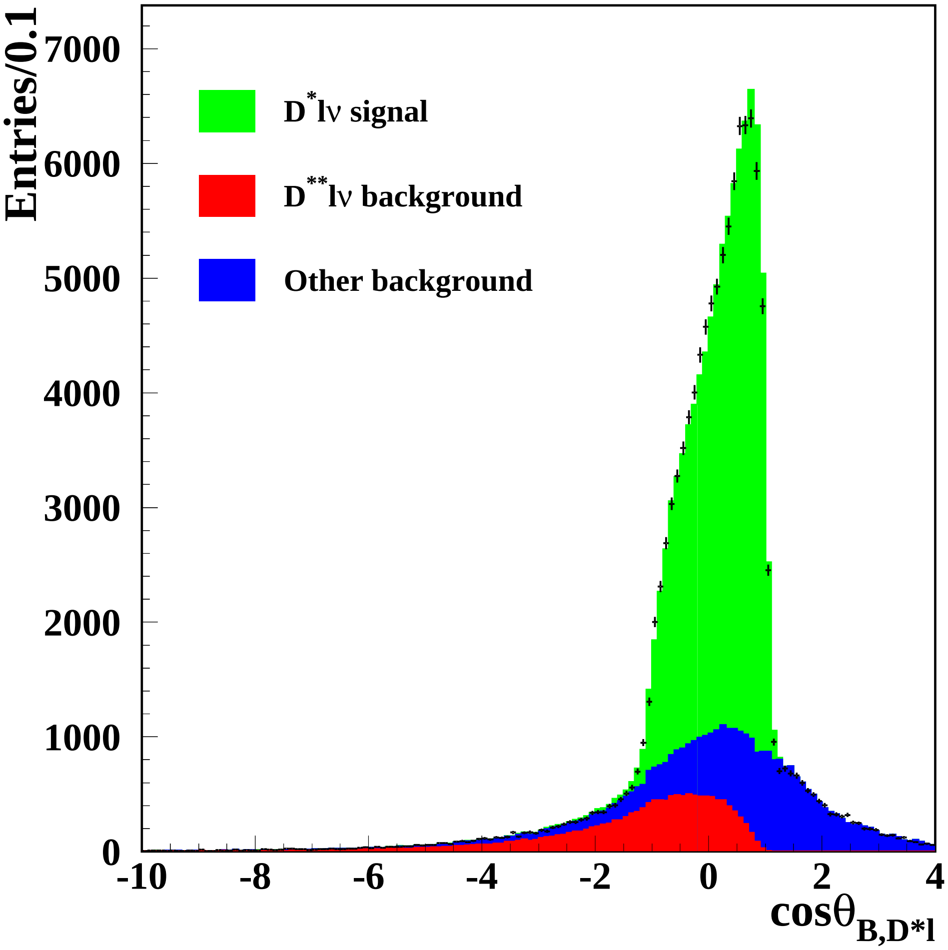

Figure 5.5: $B \to D^*l\nu$ event's $\cos\theta_B$ distribution. Cross points are the experimental Data. Green, red and blue parts are $B \to D^*l\nu$ event, $B \to D^-l\nu$ background events, and the sum of other backgrounds by Monte Carlo.

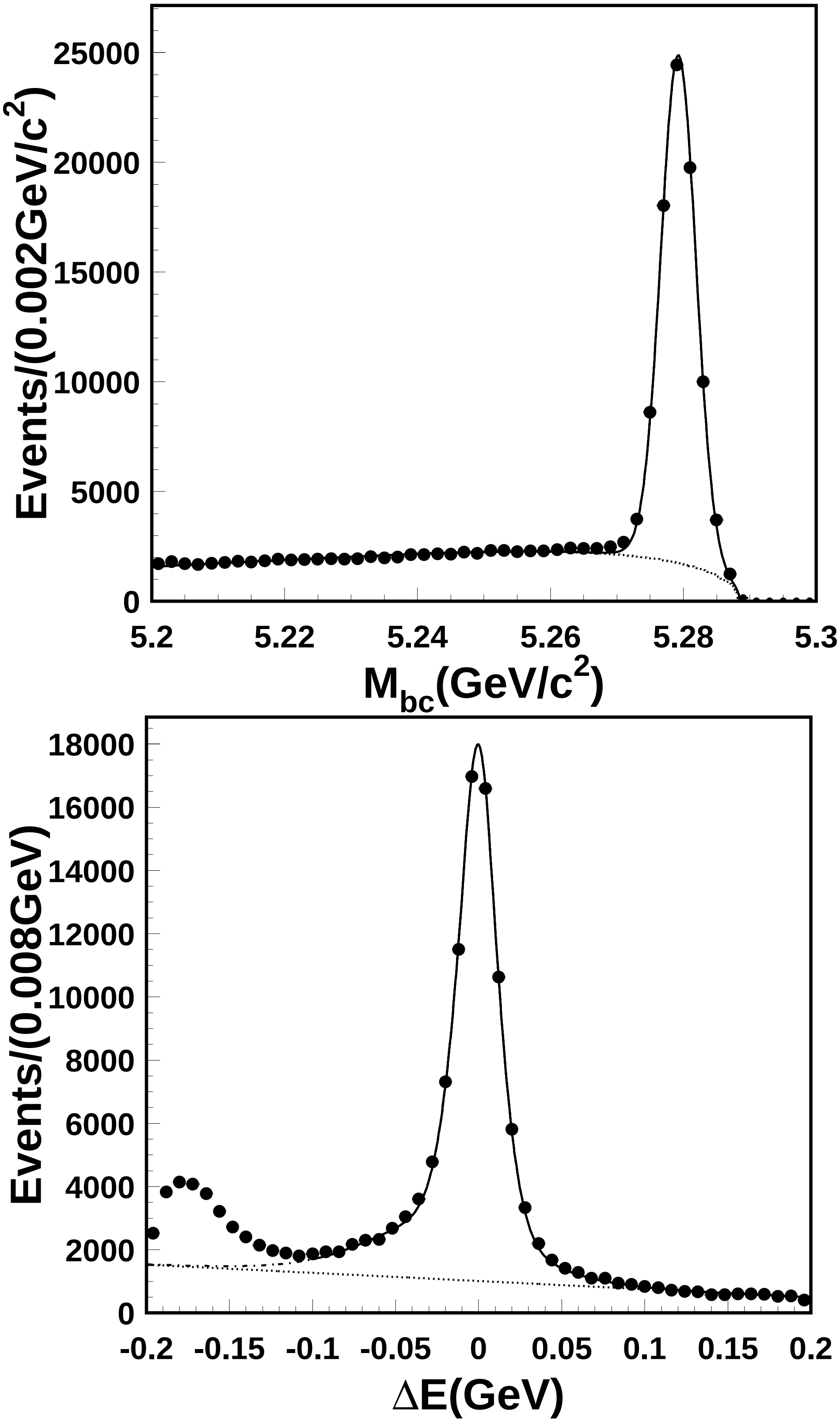

Figure 5.6: Beam-constrain-mass distribution (upper) and ΔE distribution (lower) for the reconstructed events as $D^{(*)}\pi,\ D^{*}\rho,\ J/\psi K^{(*)}$.

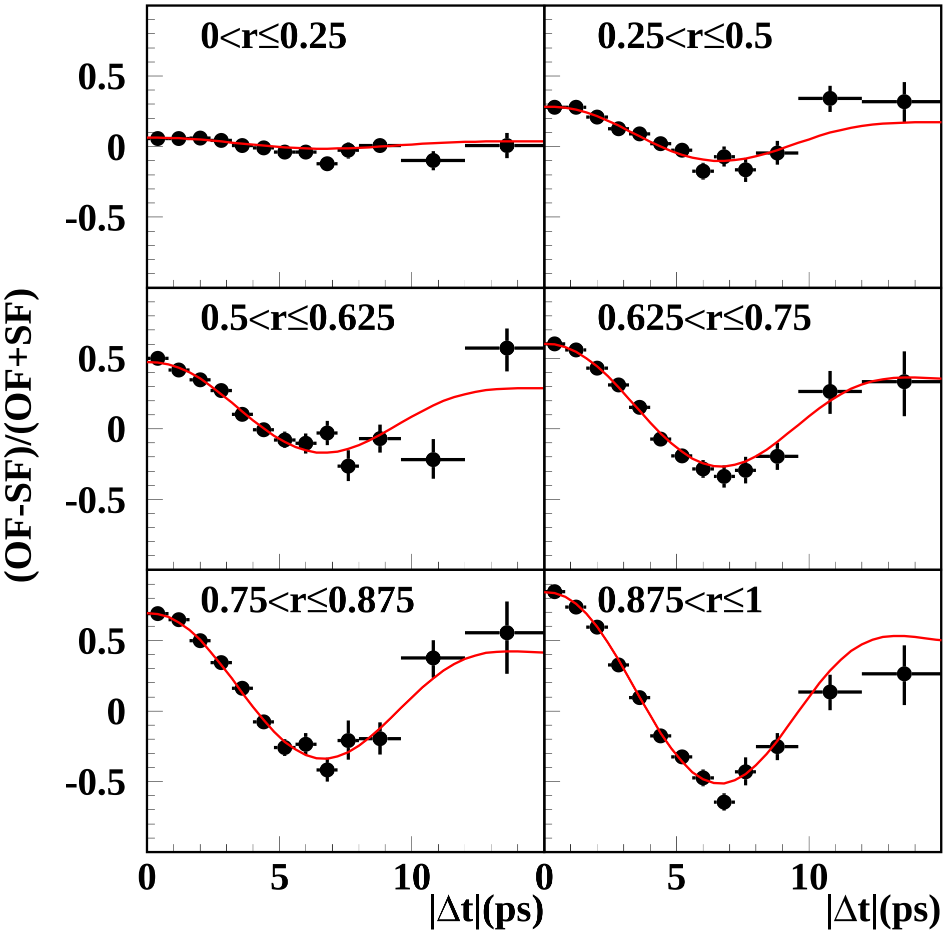

Figure 5.7: 6 r bin mixing plot

The event fractions and wrong-tag fractions are summarized in Table 5.1. The total effective tagging efficiency is determined to be $\epsilon_l \equiv \sum_{l=1}^{6} \epsilon_l (1-2w_l)^2 = 0.287 \pm 0.005$, where ϵ_l is the event fraction for each r interval. The error includes both statistical and systematic uncertainties.

l	r interval	ϵ_l	w_l	Δw_l	ϵ_{eff}^l
1	0.000-0.250	0.398	0.464±0.006	-0.0011±0.006	0.002±0.001
2	0.250-0.500	0.146	0.331±0.008	+0.0004±0.010	0.017±0.002
3	0.500-0.625	0.104	0.231±0.009	-0.0011±0.010	0.030±0.002
4	0.625-0.750	0.122	0.163±0.008	-0.0007±0.009	0.055±0.003
5	0.750-0.875	0.094	0.109±0.007	+0.0016±0.009	0.057±0.002
6	0.875-1.000	0.136	0.020±0.005	+0.0003±0.006	0.126±0.003

Table 5.1: The event fractions ϵ_l, wrong tag fractions w_l, wrong-tag fraction differences $\Delta\epsilon_l$, and average effective tagging efficiencies $\epsilon_{eff}^l = \epsilon_l (1-2w_l)^2$ for each r interval. The errors include both statistical and systematic uncertainties. The event fractions are obtained from the $B^0 \to J/\psi\ K_S^0$ simulation.

5.2 Signal and background

When we measure the CP-asymmetry parameter, $\sin 2\phi_1$, we define the following PDF equation,

$$P_i(\Delta t, \sin 2\phi_1) = (1 - f_{ol})[f_{sig} P_{sig} + (1 - f_{sig}) P_{bkg}] + f_{ol} P_{ol}$$

where P_{sig} and P_{bkg} are PDF for signal and background events which are obtain from the theoretically expected Δt distributions. It is necessary to also incorporate the experimental effects as resolution function which are describe latter. Each PDF are also described later. f_{sig} is the signal fraction which is calculated from p_B^* fit result for each candidate (KLM and ECL candidate). P_{ol} and f_{ol} are called "outlier component" which is wide Gaussian and small number of events with large Δ t. f_{ol} is small such as 5.82×10^{-4} for multiple track vertices in SVD, and 0.031 for single track vertex in SVD, which are determined from the B meson lifetime measurement.

After we determine each PDFs, we measure $\sin 2\phi_1$ by the unbinned maximum-likelihood fit for Δ t distribution from data. For fitting, we use the world average values for Δm_d and τ_B^0, which are parameter of each PDFs. We determine the $\sin 2\phi_1$ parameter in the PDFs by maximizing the combined likelihood of all candidates given by the following equation,

$$\mathbf{L} = \prod_i^n P_i(\Delta t, \sin 2\phi_1)$$

where n is the number of reconstructed $B^0 \to J/\psi\ K_L^0$ events. A statistical error of $\sin 2\phi_1$ is obtained as the difference between $\sin 2\phi_1$ values at the minumum of $-2\ln L$ and at the minimum $-2\ln L$ plus 1.

In the following section we describe how to define each fraction, PDF and resolution function.

5.2.1 Signal PDF

The probability density function expected for the signal distribution is given by

$$\mathbf{P}(\Delta t, q, w_l, \Delta w_l, \eta) = \int_{-\infty}^{+\infty} P(\Delta t') \cdot R(\Delta t - \Delta t') d(\Delta t').$$

We fix the B^0 lifetime, τ_{B^0}, and mass difference, Δm_d, at their world average values. Signal PDF is convolved with the appropriate $R_{sig}(\Delta t)$ to determine the likelihood value for event as a function of $\sin 2\phi_1$:

$$P_{sig} = \frac{e^{|\Delta t|/\tau_{B^0}}}{4\tau_{B^0}} [1 - q\Delta w_l - q\eta(1 - 2w_l) \sin 2\phi_1 \sin(\Delta m_d \Delta t)] \bigotimes R_{sig}(\Delta t). \quad (5.1)$$

5.2.2 Resolution function

Resolution function R_{sig} is parametrized by sum of two Gaussian functions. The "main" component of two Gaussians consist of three components of the SVD vertex resolution, charmed mesons lifetime, and the effect of the motion of the B mesons in the $\Upsilon(4S)$ CMS. The "tail" component of two Gaussians is caused by poor reconstructed tracks. $R_{sig}(\Delta t_i \Delta t')$ is described as the following equation,

$$\begin{aligned} R_{sig}(\Delta t' - \Delta t) &= (1 - f_{tail}) \cdot G(\Delta t_i - \Delta t'; \mu_{\Delta t}^{main}, \sigma_{\Delta t}^{main}) \\ &+ f_{tail} \cdot G(\Delta t_i - \Delta t'; \mu_{\Delta t}^{tail}, \sigma_{\Delta t}^{tail}) \\ G(\Delta t; \mu, \sigma) &= \frac{1}{\sqrt{2\pi}} exp \left[-\frac{1}{2} \left(\frac{\Delta t - \mu}{\sigma} \right)^2 \right] \end{aligned}$$

where f_{tail} is the fraction of the tail part of the resolution function, σ and μ are the resolution of proper-time difference and the mean shift of the proper-time difference, respectively.

5.2.3 Background PDF

We categorize the background events into four types as follows,

1 CP eigenstate mode

2 B^0 backgrounds

3 $B^\pm$ backgrounds

4 combinatorial background with fake J/ψ.

CP-eigenstate

If B meson decays into CP-eigenstate, PDF of backgrounds is the same as that of signal, but CP-eigenstate value, η is different from that of real $B^0 \to J/\psi\ K_L^0$ case. We define η as the following value:

a $B \to J/\psi K^{*0}(K^{*0} \to K_L^0 \pi^0)$;
mixture of CP even and odd state. We measured η in $B \to J/\psi K^{*0}(K^{*0} \to K_S^0 \pi^0)$ case, and we expect η value of $B \to J/\psi K^{*0}(K^{*0} \to K_S^0 \pi^0)$ is the same as $B \to J/\psi K^{*0}(K^{*0} \to K_L^0 \pi^0)$ case. In this thesis we select $\eta = -0.62 \pm 0.04$, which is mixture of $\eta = -1$ (81%) and $\eta = +1$ (19%) state.

b $B \to \psi(2S)\ K_L^0$, $\chi_{c1}\ K_L^0$, $J/\psi\ \pi^0$;
for these decay, we select $\eta = +1$.

c $B \to J/\psi\ K_S^0$ and other $B \to c\bar{c}\ K_S^0$;
for these decay, we select $\eta = -1$.

For these backgrounds, we use the resolution function R_{sig} for signal, as resolution function for background. Because these backgrounds are reconstructed by proper combinations of tracks.

B^0 background

If neutral B^0decays into no CP-asymmetry state, we treat Δt distribution as the following formula,

$$P_{B^0}^{bkg} = \frac{e^{-|\Delta t|/\tau_{B^0}}}{4\tau_{B^0}} \bigotimes R_{sig}(\Delta t)$$

where τ_{B^0} is real neutral B^0 lifetime, 1.542 ps.

Figure 5.8 shows the lifetime fit result for neutral B^0 background in Monte Carlo. We obtain $\tau_{B^0} = 1.5056 \pm 0.0086581\ ps$ by the fit. We use world average τ_{B^0} value when we measure $\sin 2\phi_1$.

$B^\pm$ background

We treat $B^\pm$ decay background separately. Because lifetime of $B^\pm$ meson is different from that of neutral B^0 meson. In charged $B^\pm$ decay, there are some type of final states which is $B^\pm \to J/\psi\ K_L^0\ X$, where X is charged tracks. But we reconstruct these event as $B^0 \to J/\psi\ K_L^0$. Hence X is used when we estimate B_{tag} side vertex. As a result, we estimate shorter Δt and $B^\pm$ lifetime. Thus we treat charged $B^\pm$ meson lifetime as the following formula,

$$P_{B^\pm}^{bkg} = \frac{e^{-|\Delta t|/\tau_{B^\pm}^{bkg}}}{4\tau_{B^\pm}^{bkg}} \bigotimes R_{sig}(\Delta t)$$

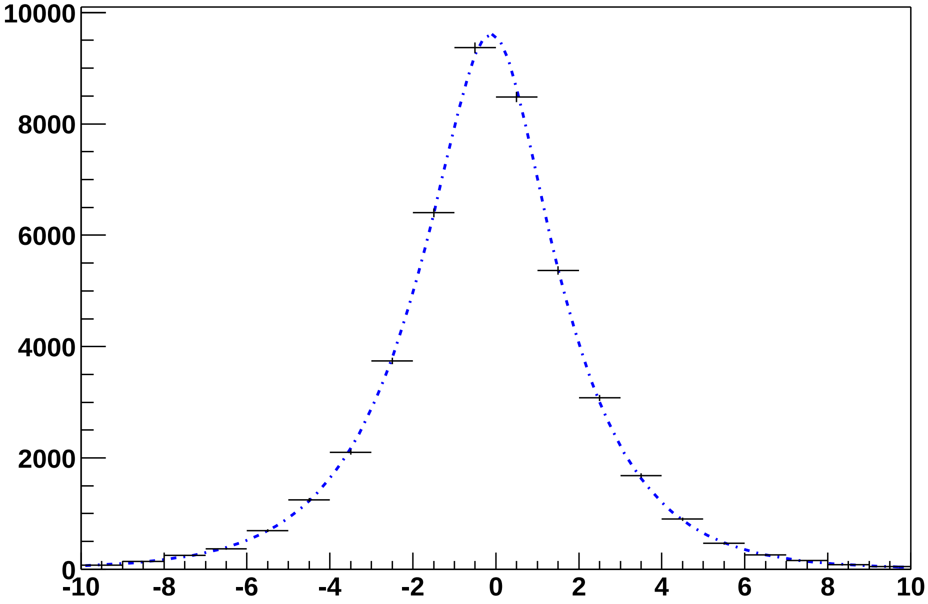

Figure 5.8: Δt plot for B^0 background in Monte Carlo

where $P^{bkg}_{B^\pm}$ is effective lifetime, and shorter than real charged $B^\pm$ meson lifetime, 1.674 ps. We estimate $\tau^{bkg}_{B^\pm}$ from charmonium inclusive Monte Carlo sample to be $\tau^{bkg}_{B^\pm} = 1.4945 \pm 0.0083274\ ps$. Figure 5.9 shows the lifetime fit result for charged $B^\pm$ background in Monte Carlo.

Fake J/ψ background

We treat own resolution function R_{comb}, different from R_{sig}, for combinatorial backgrounds. We define R_{comb} as the following equation,

$$\begin{aligned} R^{comb}(\Delta t' - \Delta t) &= (1 - f^{comb}_{tail}) \cdot G(\Delta t' - \Delta t; \mu^{comb,main}_{\Delta t}, \sigma^{comb,main}_{\Delta t}) \\ &+ f^{comb}_{tail} \cdot G(\Delta t' - \Delta t; \mu^{comb,tail}_{\Delta t}, \sigma^{comb,tail}_{\Delta t}) \\ G(\Delta t; \mu, \sigma) &= \frac{1}{\sqrt{2\pi}} exp\left[-\frac{1}{2}\left(\frac{\Delta t - \mu}{\sigma}\right)^2\right]. \end{aligned}$$

Figure 5.10 shows lifetime fit result for combinatorial backgrounds from J/ψ mass sideband data.

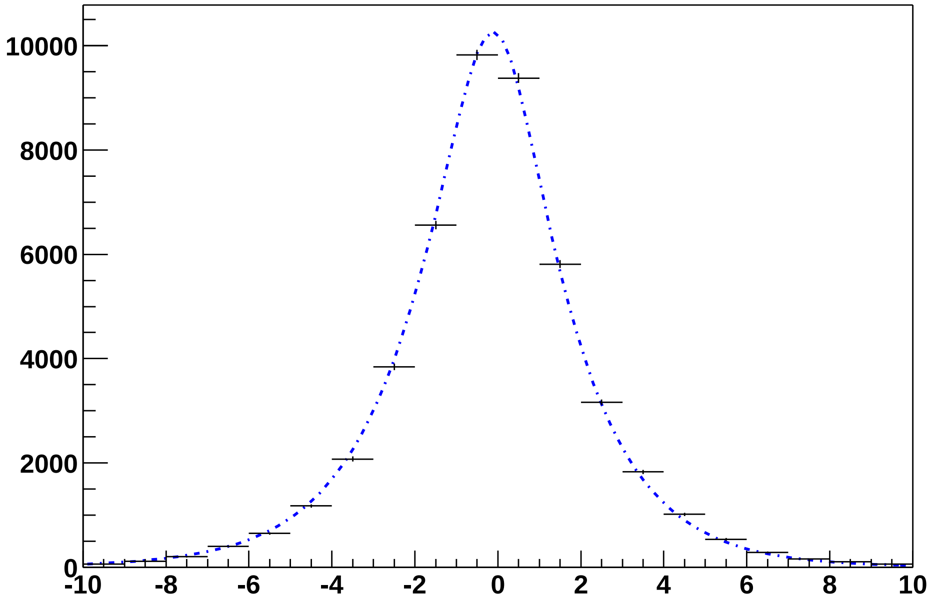

Figure 5.9: Δt plot for $B^{\pm}$ background in Monte Carlo

5.2.4 Signal and background fraction

Now, we know each PDFs for signal and each backgrounds. Next we need to estimate the fractions for signal and each backgrounds. These are signal fraction, f_{sig}, background with true K_L^0, f^{bkg}_{w/K_L^0}, background without true K_L^0, f^{bkg}_{w/oK_L^0}, and background with fake J/ψ, $f_{fakeJ/\psi}$ from p_B^* fit. We can use f_{sig} and $f_{fakeJ/\psi}$ directly when we try to fit CP-asymmetry. But we can not use f^{bkg}_{w/K_L^0} and f^{bkg}_{w/oK_L^0}. Because, when we measure $\sin 2\phi_1$, we treat backgrounds more minutely. To obtain each background fractions, we use the fit for p_B^* distribution in Monte Carlo after all selections. For fitting to p_B^* distributions for backgrounds, we use following functions:

· Reverse Crystal-Ball function, F_{RCB},

$$\begin{aligned} F_{RCB}(x) &= A\exp\left(-\frac{1}{2}\left(\frac{x-\mu}{\sigma}\right)^2\right) && \text{if } \frac{x-\mu}{\sigma} < a \\ &= A\exp\left(-\frac{1}{2}a^2\right)\left[1-\frac{a}{n}\left(\frac{x-\mu}{\sigma}-a\right)\right]^{-n} && \text{if } \frac{x-\mu}{\sigma} > a \end{aligned}$$

· Threshold function,

$$F_{thr}(x) = A(x-\mu)\exp(c_1(x-\mu)+c_2(x-\mu)^2).$$

Figure 5.11 and 5.12 shows fit result for each background components. We get each background fraction for event-by-event.

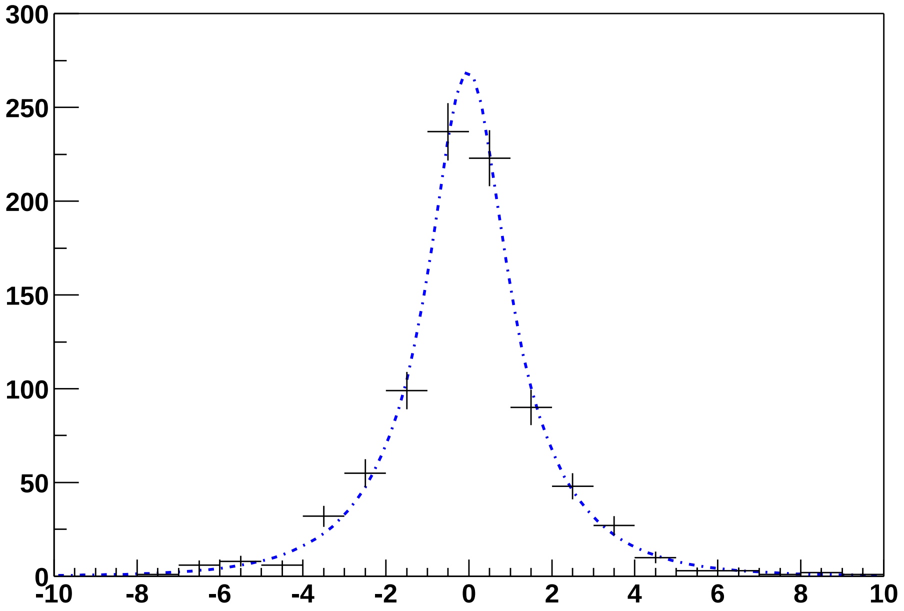

Figure 5.10: Δt plot for J/ψ mass sideband data

Finally, we determine background fraction and PDFs as follows,

$$\begin{aligned}(1-f^{sig})P^{bkg}_{total} &= f^{bkg}_{total}P^{bkg}_{total}\\ &= f^{bkg}_{CP}P^{bkg}_{CP}+f^{bkg}_{B^0}P^{bkg}_{B^0}+f^{bkg}_{B^\pm}P^{bkg}_{B^\pm}+f^{bkg}_{comb}P^{bkg}_{comb}\\ &= f^{bkg}_{J/\psi K^{*0}}P^{bkg}_{J/\psi K^{*0}}+f^{bkg}_{even}P^{bkg}_{even}+f^{bkg}_{odd}P^{bkg}_{odd}+f^{bkg}_{B^0}P^{bkg}_{B^0}+f^{bkg}_{B^\pm}P^{bkg}_{B^\pm}+f^{bkg}_{comb}P^{bkg}_{comb}\end{aligned}$$

where $f^{bkg}_{J/\psi K^{*0}}+f^{bkg}_{even}+f^{bkg}_{odd}+f^{bkg}_{B^0}+f^{bkg}_{B^\pm}+f^{bkg}_{comb}=f^{bkg}_{total}$.

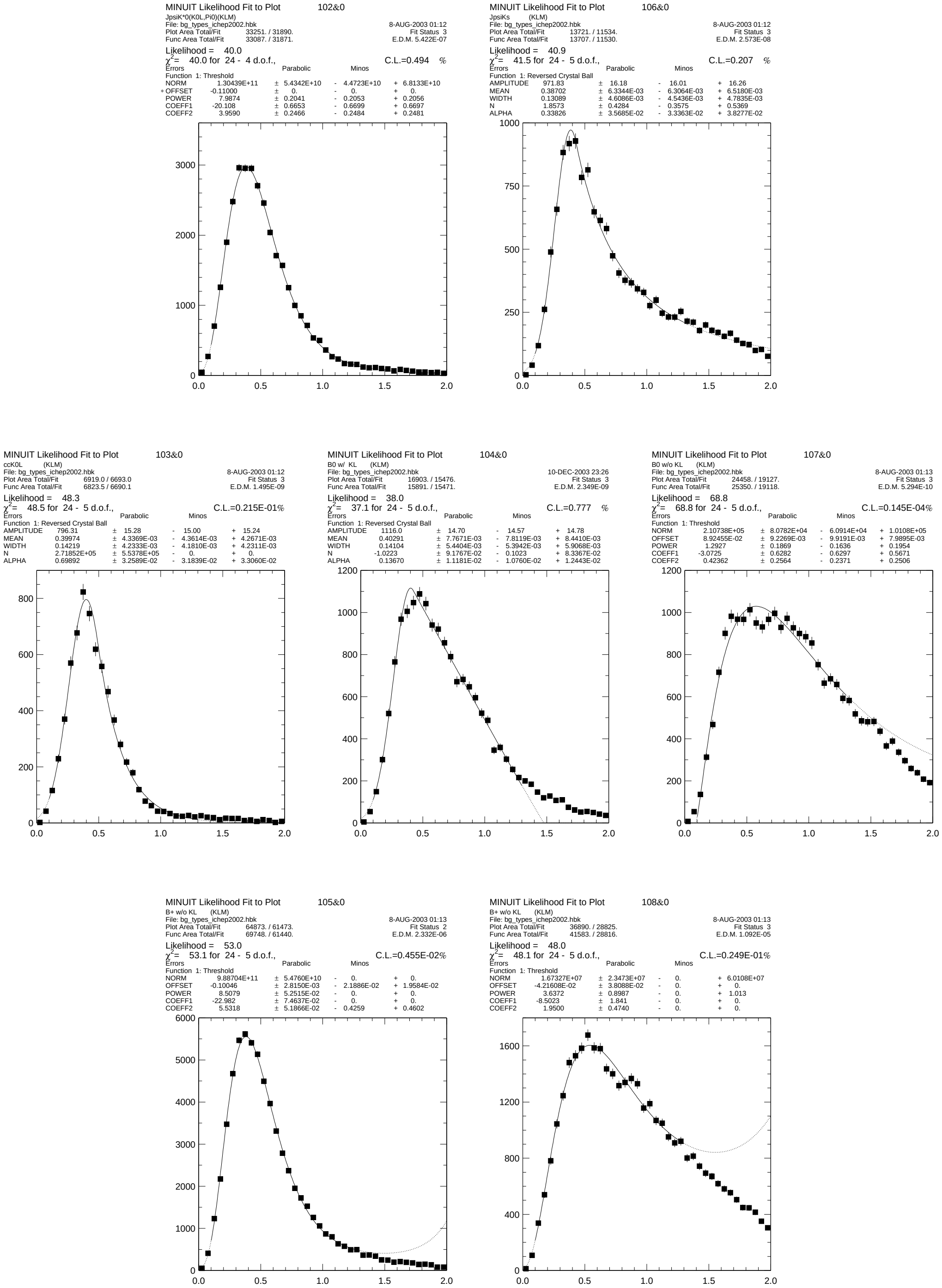

```
MINUIT Likelihood Fit to Plot          102&0
JpsiK*0(K0L,Pi0)(KLM)
File: bg_types_ichep2002.hbk                                   8-AUG-2003 01:12
Plot Area Total/Fit          33251. / 31890.                       Fit Status  3
Func Area Total/Fit          33087. / 31871.                  E.D.M. 5.422E-07
Likelihood =    40.0
χ2=    40.0 for  24 -  4 d.o.f.,                           C.L.=0.494    %
Errors                              Parabolic            Minos
Function  1: Threshold
 NORM          1.30439E+11     ±  5.4342E+10    -  4.4723E+10    +  6.8133E+10
*OFFSET       -0.11000         ±     0.         -     0.         +     0.
 POWER          7.9874         ±  0.2041        -  0.2053        +  0.2056
 COEFF1       -20.108          ±  0.6653        -  0.6699        +  0.6697
 COEFF2         3.9590         ±  0.2466        -  0.2484        +  0.2481
```

```
MINUIT Likelihood Fit to Plot          106&0
JpsiKs        (KLM)
File: bg_types_ichep2002.hbk                                   8-AUG-2003 01:12
Plot Area Total/Fit          13721. / 11534.                       Fit Status  3
Func Area Total/Fit          13707. / 11530.                  E.D.M. 2.573E-08
Likelihood =    40.9
χ2=    41.5 for  24 -  5 d.o.f.,                           C.L.=0.207    %
Errors                              Parabolic            Minos
Function  1: Reversed Crystal Ball
AMPLITUDE      971.83          ±   16.18        -   16.01        +   16.26
MEAN           0.38702         ±  6.3344E-03    -  6.3064E-03    +  6.5180E-03
WIDTH          0.13089         ±  4.6086E-03    -  4.5436E-03    +  4.7835E-03
N               1.8573         ±  0.4284        -  0.3575        +  0.5369
ALPHA          0.33826         ±  3.5685E-02    -  3.3363E-02    +  3.8277E-02
```

```
MINUIT Likelihood Fit to Plot          103&0
ccK0L         (KLM)
File: bg_types_ichep2002.hbk                                   8-AUG-2003 01:12
Plot Area Total/Fit          6919.0 / 6693.0                       Fit Status  3
Func Area Total/Fit          6823.5 / 6690.1                  E.D.M. 1.495E-09
Likelihood =    48.3
χ2=    48.5 for  24 -  5 d.o.f.,                           C.L.=0.215E-01%
Errors                              Parabolic            Minos
Function  1: Reversed Crystal Ball
AMPLITUDE      796.31          ±   15.28        -   15.00        +   15.24
MEAN           0.39974         ±  4.3369E-03    -  4.3614E-03    +  4.2671E-03
WIDTH          0.14219         ±  4.2333E-03    -  4.1810E-03    +  4.2311E-03
N              2.71852E+05     ±  5.5378E+05    -     0.         +     0.
ALPHA          0.69892         ±  3.2589E-02    -  3.1839E-02    +  3.3060E-02
```

```
MINUIT Likelihood Fit to Plot          104&0
B0 w/  KL       (KLM)
File: bg_types_ichep2002.hbk                                  10-DEC-2003 23:26
Plot Area Total/Fit          16903. / 15476.                       Fit Status  3
Func Area Total/Fit          15891. / 15471.                  E.D.M. 2.349E-09
Likelihood =    38.0
χ2=    37.1 for  24 -  5 d.o.f.,                           C.L.=0.777    %
Errors                              Parabolic            Minos
Function  1: Reversed Crystal Ball
AMPLITUDE      1116.0          ±   14.70        -   14.57        +   14.78
MEAN           0.40291         ±  7.7671E-03    -  7.8119E-03    +  8.4410E-03
WIDTH          0.14104         ±  5.4404E-03    -  5.3942E-03    +  5.9068E-03
N             -1.0223          ±  9.1767E-02    -  0.1023        +  8.3367E-02
ALPHA          0.13670         ±  1.1181E-02    -  1.0760E-02    +  1.2443E-02
```

```
MINUIT Likelihood Fit to Plot          107&0
B0 w/o KL       (KLM)
File: bg_types_ichep2002.hbk                                   8-AUG-2003 01:13
Plot Area Total/Fit          24458. / 19127.                       Fit Status  3
Func Area Total/Fit          25350. / 19118.                  E.D.M. 5.294E-10
Likelihood =    68.8
χ2=    68.8 for  24 -  5 d.o.f.,                           C.L.=0.145E-04%
Errors                              Parabolic            Minos
Function  1: Threshold
NORM           2.10738E+05     ±  8.0782E+04    -  6.0914E+04    +  1.0108E+05
OFFSET         8.92455E-02     ±  9.2269E-03    -  9.9191E-03    +  7.9895E-03
POWER           1.2927         ±  0.1869        -  0.1636        +  0.1954
COEFF1        -3.0725          ±  0.6282        -  0.6297        +  0.5671
COEFF2         0.42362         ±  0.2564        -  0.2371        +  0.2506
```

```
MINUIT Likelihood Fit to Plot          105&0
B+ w/o KL       (KLM)
File: bg_types_ichep2002.hbk                                   8-AUG-2003 01:13
Plot Area Total/Fit          64873. / 61473.                       Fit Status  2
Func Area Total/Fit          69748. / 61440.                  E.D.M. 2.332E-06
Likelihood =    53.0
χ2=    53.1 for  24 -  5 d.o.f.,                           C.L.=0.455E-02%
Errors                              Parabolic            Minos
Function  1: Threshold
NORM           9.88704E+11     ±  5.4760E+10    -     0.         +     0.
OFFSET        -0.10046         ±  2.8150E-03    -  2.1886E-02    +  1.9584E-02
POWER           8.5079         ±  5.2515E-02    -     0.         +     0.
COEFF1        -22.982          ±  7.4637E-02    -     0.         +     0.
COEFF2          5.5318         ±  5.1866E-02    -  0.4259        +  0.4602
```

```
MINUIT Likelihood Fit to Plot          108&0
B+ w/o KL       (KLM)
File: bg_types_ichep2002.hbk                                   8-AUG-2003 01:13
Plot Area Total/Fit          36890. / 28825.                       Fit Status  3
Func Area Total/Fit          41583. / 28816.                  E.D.M. 1.092E-05
Likelihood =    48.0
χ2=    48.1 for  24 -  5 d.o.f.,                           C.L.=0.249E-01%
Errors                              Parabolic            Minos
Function  1: Threshold
NORM           1.67327E+07     ±  2.3473E+07    -  0.            +  6.0108E+07
OFFSET        -4.21608E-02     ±  3.8088E-02    -  0.            +     0.
POWER           3.6372         ±  0.8987        -  0.            +   1.013
COEFF1        -8.5023          ±   1.841        -  0.            +     0.
COEFF2          1.9500         ±  0.4740        -  0.            +     0.
```

Figure 5.11: KLM candidate p_B^* fit for backgrounds in Monte Calro

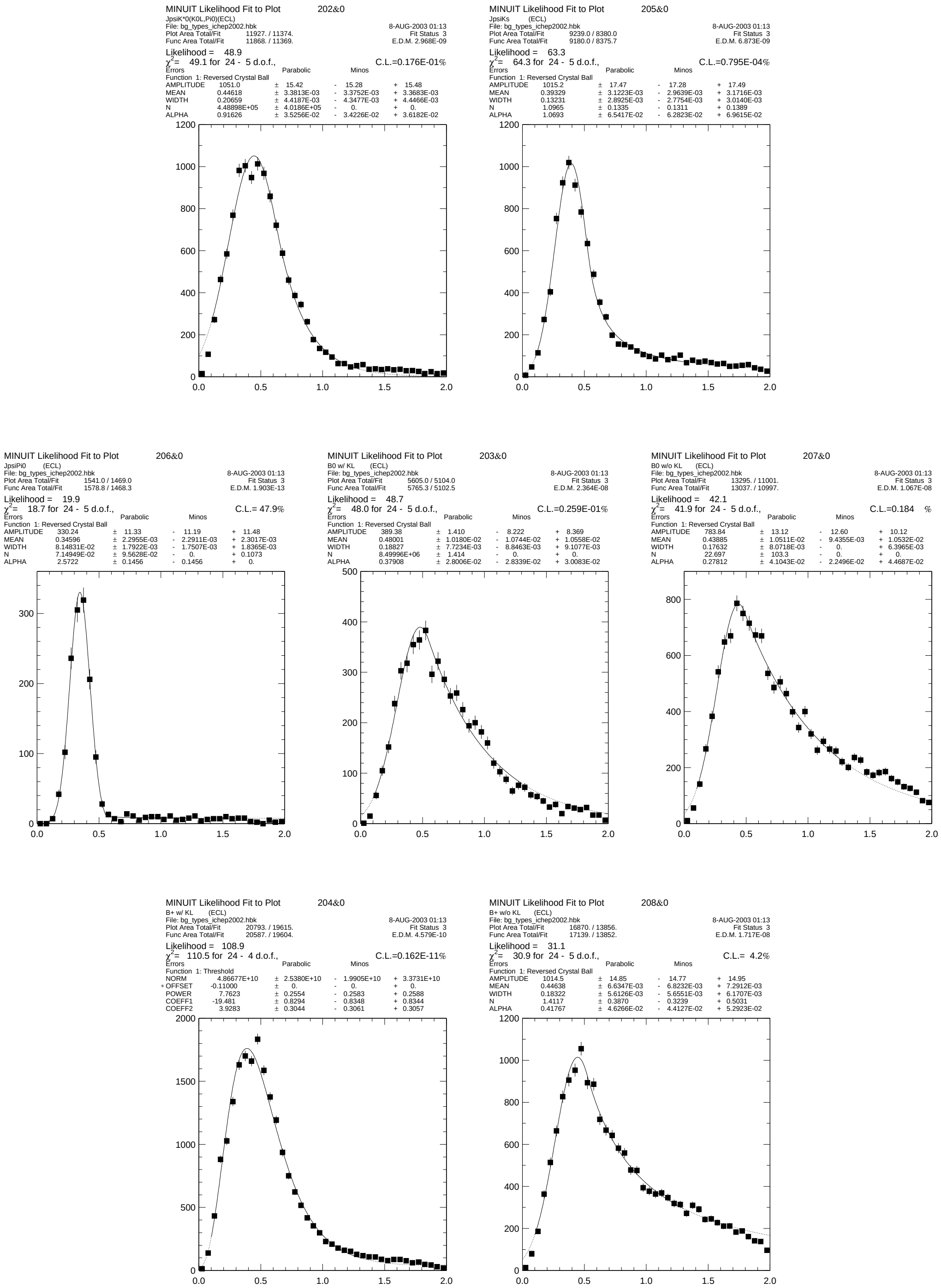

```
MINUIT Likelihood Fit to Plot          202&0
JpsiK*0(K0L,Pi0)(ECL)
File: bg_types_ichep2002.hbk                                  8-AUG-2003 01:13
Plot Area Total/Fit      11927. / 11374.                          Fit Status  3
Func Area Total/Fit      11868. / 11369.                      E.D.M. 2.968E-09
Likelihood =    48.9
χ2=    49.1 for  24 -  5 d.o.f.,                          C.L.=0.176E-01%
Errors                              Parabolic            Minos
Function  1: Reversed Crystal Ball
AMPLITUDE     1051.0          ±   15.42         -   15.28         +   15.48
MEAN          0.44618         ±  3.3813E-03     -  3.3752E-03     +  3.3683E-03
WIDTH         0.20659         ±  4.4187E-03     -  4.3477E-03     +  4.4466E-03
N             4.48898E+05     ±  4.0186E+05     -     0.          +     0.
ALPHA         0.91626         ±  3.5256E-02     -  3.4226E-02     +  3.6182E-02
```

```
MINUIT Likelihood Fit to Plot          205&0
JpsiKs        (ECL)
File: bg_types_ichep2002.hbk                                  8-AUG-2003 01:13
Plot Area Total/Fit      9239.0 / 8380.0                          Fit Status  3
Func Area Total/Fit      9180.0 / 8375.7                      E.D.M. 6.873E-09
Likelihood =    63.3
χ2=    64.3 for  24 -  5 d.o.f.,                          C.L.=0.795E-04%
Errors                              Parabolic            Minos
Function  1: Reversed Crystal Ball
AMPLITUDE     1015.2          ±   17.47         -   17.28         +   17.49
MEAN          0.39329         ±  3.1223E-03     -  2.9639E-03     +  3.1716E-03
WIDTH         0.13231         ±  2.8925E-03     -  2.7754E-03     +  3.0140E-03
N             1.0965          ±  0.1335         -  0.1311         +  0.1389
ALPHA         1.0693          ±  6.5417E-02     -  6.2823E-02     +  6.9615E-02
```

```
MINUIT Likelihood Fit to Plot          206&0
JpsiPi0       (ECL)
File: bg_types_ichep2002.hbk                                  8-AUG-2003 01:13
Plot Area Total/Fit      1541.0 / 1469.0                          Fit Status  3
Func Area Total/Fit      1578.8 / 1468.3                      E.D.M. 1.903E-13
Likelihood =    19.9
χ2=    18.7 for  24 -  5 d.o.f.,                              C.L.= 47.9%
Errors                              Parabolic            Minos
Function  1: Reversed Crystal Ball
AMPLITUDE     330.24          ±   11.33         -   11.19         +   11.48
MEAN          0.34596         ±  2.2955E-03     -  2.2911E-03     +  2.3017E-03
WIDTH         8.14831E-02     ±  1.7922E-03     -  1.7507E-03     +  1.8365E-03
N             7.14949E-02     ±  9.5628E-02     -     0.          +  0.1073
ALPHA         2.5722          ±  0.1456         -  0.1456         +     0.
```

```
MINUIT Likelihood Fit to Plot          203&0
B0 w/ KL       (ECL)
File: bg_types_ichep2002.hbk                                  8-AUG-2003 01:13
Plot Area Total/Fit      5605.0 / 5104.0                          Fit Status  3
Func Area Total/Fit      5765.3 / 5102.5                      E.D.M. 2.364E-08
Likelihood =    48.7
χ2=    48.0 for  24 -  5 d.o.f.,                          C.L.=0.259E-01%
Errors                              Parabolic            Minos
Function  1: Reversed Crystal Ball
AMPLITUDE     389.38          ±   1.410         -   8.222         +   8.369
MEAN          0.48001         ±  1.0180E-02     -  1.0744E-02     +  1.0558E-02
WIDTH         0.18827         ±  7.7234E-03     -  8.8463E-03     +  9.1077E-03
N             8.49996E+06     ±   1.414         -     0.          +     0.
ALPHA         0.37908         ±  2.8006E-02     -  2.8339E-02     +  3.0083E-02
```

```
MINUIT Likelihood Fit to Plot          207&0
B0 w/o KL      (ECL)
File: bg_types_ichep2002.hbk                                  8-AUG-2003 01:13
Plot Area Total/Fit      13295. / 11001.                          Fit Status  3
Func Area Total/Fit      13037. / 10997.                      E.D.M. 1.067E-08
Likelihood =    42.1
χ2=    41.9 for  24 -  5 d.o.f.,                          C.L.=0.184    %
Errors                              Parabolic            Minos
Function  1: Reversed Crystal Ball
AMPLITUDE     783.84          ±   13.12         -   12.60         +   10.12
MEAN          0.43885         ±  1.0511E-02     -  9.4355E-03     +  1.0532E-02
WIDTH         0.17632         ±  8.0718E-03     -     0.          +  6.3965E-03
N              22.697         ±   103.3         -     0.          +     0.
ALPHA         0.27812         ±  4.1043E-02     -  2.2496E-02     +  4.4687E-02
```

```
MINUIT Likelihood Fit to Plot          204&0
B+ w/ KL       (ECL)
File: bg_types_ichep2002.hbk                                  8-AUG-2003 01:13
Plot Area Total/Fit      20793. / 19615.                          Fit Status  3
Func Area Total/Fit      20587. / 19604.                      E.D.M. 4.579E-10
Likelihood =   108.9
χ2=   110.5 for  24 -  4 d.o.f.,                          C.L.=0.162E-11%
Errors                              Parabolic            Minos
Function  1: Threshold
 NORM          4.86677E+10     ±  2.5380E+10     -  1.9905E+10     +  3.3731E+10
*OFFSET       -0.11000         ±     0.          -     0.          +     0.
 POWER          7.7623         ±  0.2554         -  0.2583         +  0.2588
 COEFF1       -19.481          ±  0.8294         -  0.8348         +  0.8344
 COEFF2         3.9283         ±  0.3044         -  0.3061         +  0.3057
```

```
MINUIT Likelihood Fit to Plot          208&0
B+ w/o KL      (ECL)
File: bg_types_ichep2002.hbk                                  8-AUG-2003 01:13
Plot Area Total/Fit      16870. / 13856.                          Fit Status  3
Func Area Total/Fit      17139. / 13852.                      E.D.M. 1.717E-08
Likelihood =    31.1
χ2=    30.9 for  24 -  5 d.o.f.,                              C.L.=  4.2%
Errors                              Parabolic            Minos
Function  1: Reversed Crystal Ball
AMPLITUDE     1014.5          ±   14.85         -   14.77         +   14.95
MEAN          0.44638         ±  6.6347E-03     -  6.8232E-03     +  7.2912E-03
WIDTH         0.18322         ±  5.6126E-03     -  5.6551E-03     +  6.1707E-03
N             1.4117          ±  0.3870         -  0.3239         +  0.5031
ALPHA         0.41767         ±  4.6266E-02     -  4.4127E-02     +  5.2923E-02
```

Figure 5.12: ECL candidate p_B^* fit for backgrounds in Monte Carlo

5.3 Result of the fit

After flavor tagging and vertex reconstruction, we get 2332 events as $B^0 \to J/\psi\, K_L^0$ candidates reconstructed at Belle. The CP-asymmery parameter is obtained from Δ t distribution. We determine the most probable CP-asymmetry parameter by maximizing the likelihood function. We obtaine,

$$\sin 2\phi_1 = 0.747 \pm 0.128(statistical).$$

Figure 5.13 shows the decay time difference Δt and the time-dependent "raw" CP-asymmetry $A(\Delta t)$ distributions.

5.4 Systematic uncertainties

5.4.1 Vertex reconstruction

We check systematics from outliers by re-fitting the CP-fit with $\sin 2\phi_1$ parameter without nominal vertex cut, $|\Delta t| < 70ps$, and tightening to $|\Delta t| < 5ps$. For doing this, we study scale factor effect by re-fitting the $\sin 2\phi_1$ with scale factor to unity. We estimate the effect of vertexing by changing the reduced χ^2 cut for the reconstruction of vertex from < 100 to < 50 or < 200.

By loosening and tightening the track-quality criterion for the tag-side vertex reconstruction by 10%, charged-dependent bias of tracks for z-position could result in a detector-induced CP-asymmetry. We estimate that the position bias is small ($\pm 3\ \mu m$) by using cosmic rays and $\gamma\gamma \to \rho^0\rho^0 \to \pi^+\pi^-\pi^+\pi^-$ events. We study the effect on the $\sin 2\phi_1$ parameter by repeating the CP-fit with the track's z-position shifted by $\pm\ 3\mu m$. We find the effect on the $\sin 2\phi_1$ is negligible small.

5.4.2 Flavor tagging

To estimate systematics of wrong-tag fractions, we re-fit the $\sin 2\phi_1$ parameter by varying the wrong-tag fractions by its error for each r bin. The observed deviations in the $\sin 2\phi_1$ are added in quadrature.

5.4.3 Resolution function

After we vary all parameters of resolution function by $\pm\sigma$, we re-fit the CP-fit. The observed deviations in the $\sin 2\phi_1$ are added in quadrature. To check the dependence on the functional form of the resolution function, we re-fit the $\sin 2\phi_1$ parameter by using a different parameterization.

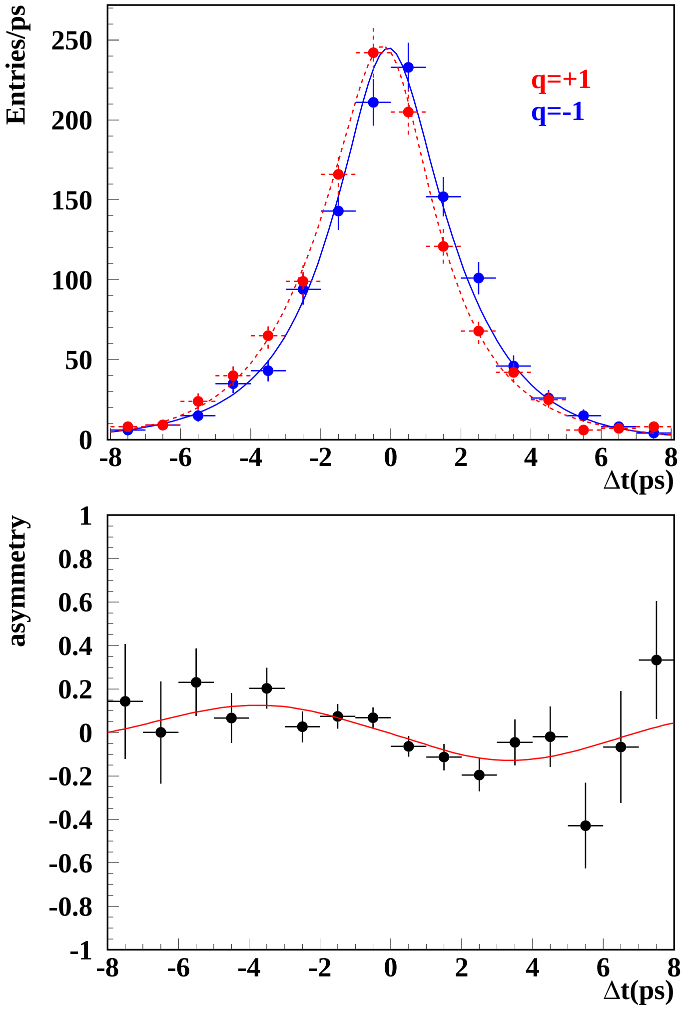

Figure 5.13: Δ t distribution (upper) and the time-dependent "raw" CP-asymmetry, $A(\Delta t)$, distribution (lower) for 2332 $B^0 \rightarrow J/\psi\ K_L^0$ candidates reconstructed at Belle.

5.4.4 Signal fraction

Signal fraction is obtained by normalization of fitting components of signal event $B^0 \to J/\psi\ K_L^0$, background with true K_L^0, $B \to J/\psi K_L^0 X$, background without K_L^0, $B \to J/\psi X$, and background with fake J/ψ. First three normalizations are determined from the fit to the p_B^* spectrum. Normalization of fourth components, which is fake J/ψ, is determined from J/ψ invariant mass fit. To estimate these systematic uncertainty from the signal fraction, we vary these components by $\pm\sigma$, where σ is their systematic error of nominal normalization. Then we get new signal fraction and re-fit the CP-asymmetry fit with new-parameters. When we fit normal p_B^* fit by floating the signal peak position, we vary this component by $\pm\sigma$ and fix to zero. From these fitting, we get new signal fraction and then try to re-fit the $\sin 2\phi_1$.

parameter	variation	$\Delta \sin 2\phi_1$
signal	$+\sigma$	0.025
signal	$-\sigma$	-0.019
BG w/ true K_L^0	$+\sigma$	-0.020
BG w/ true K_L^0	$-\sigma$	0.019
BG w/o true K_L^0	$+\sigma$	0.006
BG w/o true K_L^0	$-\sigma$	-0.007
BG fake J/ψ	$+\sigma$	0.008
BG fake J/ψ	$-\sigma$	-0.008
peak position	$+\sigma$	0.002
peak position	$-\sigma$	-0.003
peak position	fixed 0	-0.001

Table 5.2: Deviations in $\sin 2\phi_1$ when the signal and background normalizations are varied within their statistical uncertainties, or obtain with an alternative yield fit.

5.4.5 Background PDFs

When we estimate the background PDFs, we fit p_B^* shape using reverse-crystal-ball function or threshold function, excluding $0.0 < p_B^* < 0.1$ and $1.3 < p_B^* < 2.0\ GeV/c$. We include these regions and vary these functions parameters by $\pm\sigma$, and then re-fit the $\sin 2\phi_1$ to estimate systematics of background PDFs.

5.4.6 Physics assumption

When we try to fit the $\sin 2\phi_1$, we fix the neutral B meson lifetime, mass, and mixing parameter at their world average values of $\tau_{B^0} = 1.542 \pm 0.016\ ps$, $m_{B^0} = 5.2794 \pm 0.0005\ GeV/c^2$ and $\Delta m_d = 0.489 \pm 0.008$, respectively. To estimate systematics from these parameters, we vary the parameters by their errors. The effective CP-eigenvalue of $B \to J/\psi\ K^{*0}(K^{*0} \to K_L^0\ \pi^0)$ decay is mixing with $\eta = +1$ and $\eta = -1$ states. The fraction of $\eta = +1$ state is 0.19 ± 0.02. It is varied by its error to estimate the effect due to the fraction error.

5.4.7 Δ t shape

Effective lifetime of the background from charged $B^{\pm}$ is decided to be $\tau_{B^{\pm}}^{bkg} = 1.4945 \pm 0.0083274$ ps by Monte Carlo. The lifetime for combinatorial background is obtained by the same way. We re-fit the CP-fit by varing the effective liftime by $\pm\sigma$ obtained above.

5.4.8 Total systematics

We estimate total systematic error from above results. The total systematic error is obtained to be 0.057. Table 5.3 gives a summary of the observed deviations in $\sin 2\phi_1$.

class of parameters	systematics error
vertex reconstruction	0.013
flavor tagging	0.014
resolution function	0.009
fit bias	0.008
signal purity	0.045
BG composition	0.026
BG fit region	0.005
physic parameters	0.005
BG shape in Δt	0.002
tag side interference	0.001
total	0.057

Table 5.3: Contributions to the systematic error on $\sin 2\phi_1$. Each entry shows the accumulative uncertainty arising from a class of cuts and parameters used the CP-fit.

Chapter 6

Discussion and Conclusion

Using $140/fb$ data sample ($152M$ $B\bar{B}$ pairs) collected at the $\Upsilon(4S)$ resonance with the Belle detector at KEKB asymmetric e^+e^- collider, we reconstruct 2332 $B^0 \to J/\psi\ K_L^0$ decay candidates with a purity of 62%. From the maximum likelihood fit to these candidates, we obtained:

$$\sin 2\phi_1 = 0.747 \pm 0.128(statistical) \pm 0.057(systematic).$$

6.1 Comparison with other measurements at Belle

We also measured $B^0 \to J/\psi\ K_S^0$ and other $c\bar{c}K_S^0$, whose CP-eigenstate value is opposite to $B^0 \to J/\psi\ K_L^0$. We found 3085 events with a purity of 93.3%. The maximum likelihood fit to these candidates yields:

$$\sin 2\phi_1 = 0.668 \pm 0.075(statistical).$$

In Chapter 2, we showed that CP-asymmetry in $B^0 \to J/\psi\ K_L^0$ and $B^0 \to J/\psi\ K_S^0$ decay is to be equal in magnitude and opposite in sign. Figure 6.1 shows "raw" CP-asymmetry distributions for these two decay modes. The CP-asymmetry sign of $B^0 \to J/\psi\ K_S^0$ is opposite to that of $B^0 \to J/\psi\ K_L^0$. The amplitude of "raw" CP-asymmetry curve for $B^0 \to J/\psi\ K_L^0$ is smaller than that of $B^0 \to J/\psi\ K_S^0$. This difference is caused by the difference of the dilution factor because $B^0 \to J/\psi\ K_L^0$ background level is larger.

In Figure 6.2, top distribution shows Δt distributions for the events with $q \cdot \eta_{cp} = -1$ and $+1$. Solid and open points are for the events with $q \cdot \eta_{cp} = +1$ and -1 , respectively, when it is combined with all CP modes. Middle and bottom distributions show the "raw" CP-asymmetry for the samples with the flavor tagging quality of $0 < r \leq 0.5$ and $0.5 < r \leq 1$, respectively.

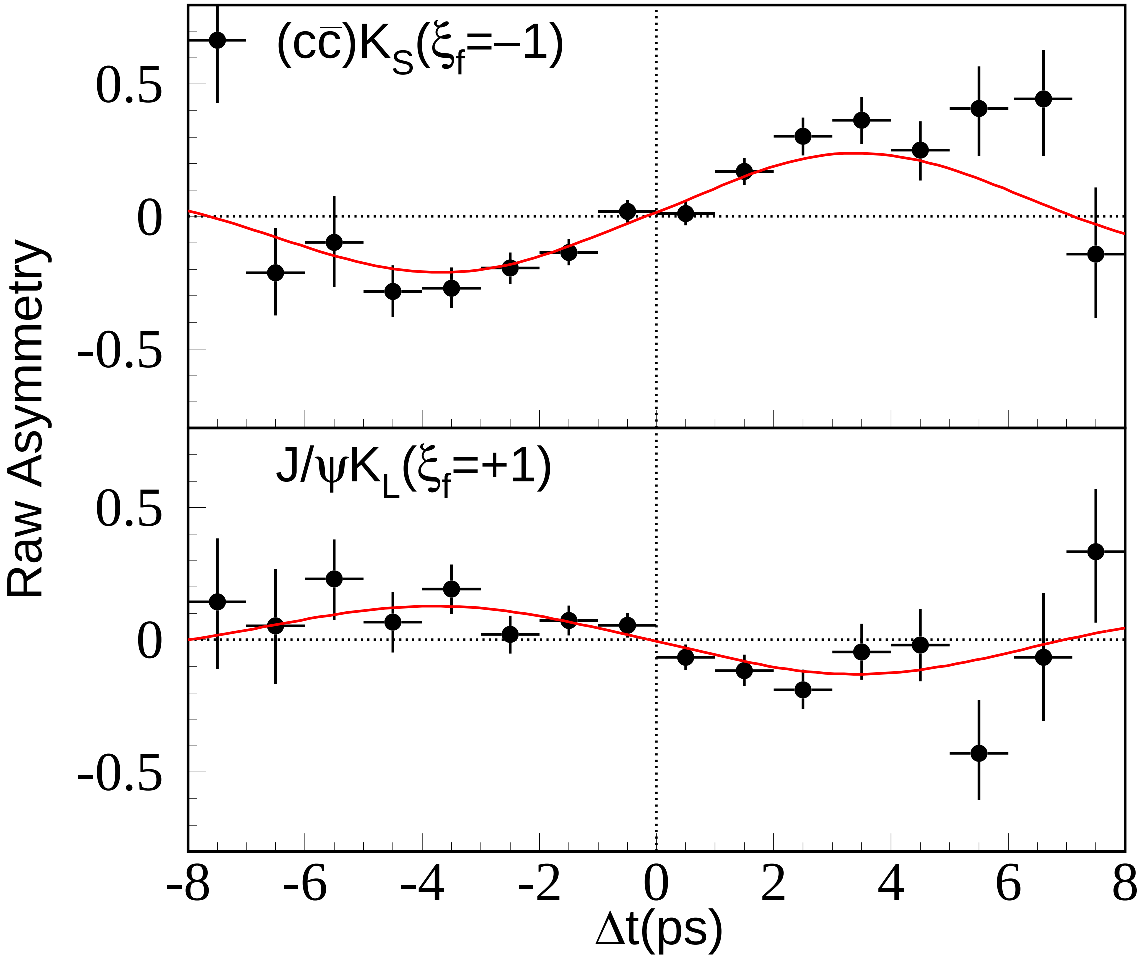

Figure 6.1: "Raw" CP-asymmetry distributions for $c\bar{c}K_S^0$ (upper) and $J/\psi K_L^0$ (lower).

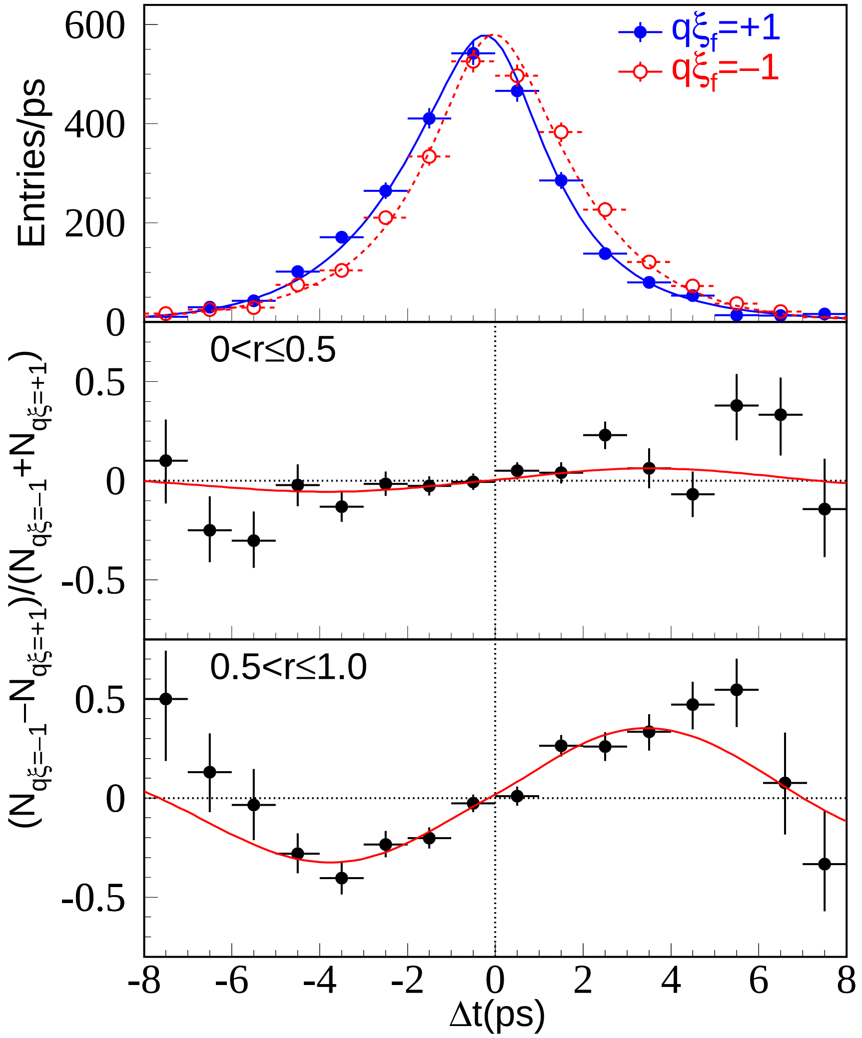

Figure 6.2: Δ t distributions (top) for the events with $q \cdot \eta_{cp} = +1$ (solid) and -1 (open) combined all CP modes, and "Raw" CP-asymmetry distributions for the events with the flavor tagging dilution parameter of $0 < r \leq 0.5$ (middle) and $0.5 < r \leq 1$ (bottom).

6.2 Other measurements of $\sin 2\phi_1$

The other statistically significant measurement of $\sin 2\phi_1$ comes from the BaBar experiment. It is in good agreement with Belle result. The comparison with the most recent results from other experiments is shown in Figure 6.3. The average of these is $\sin 2\phi_1 = 0.736 \pm 0.049$.

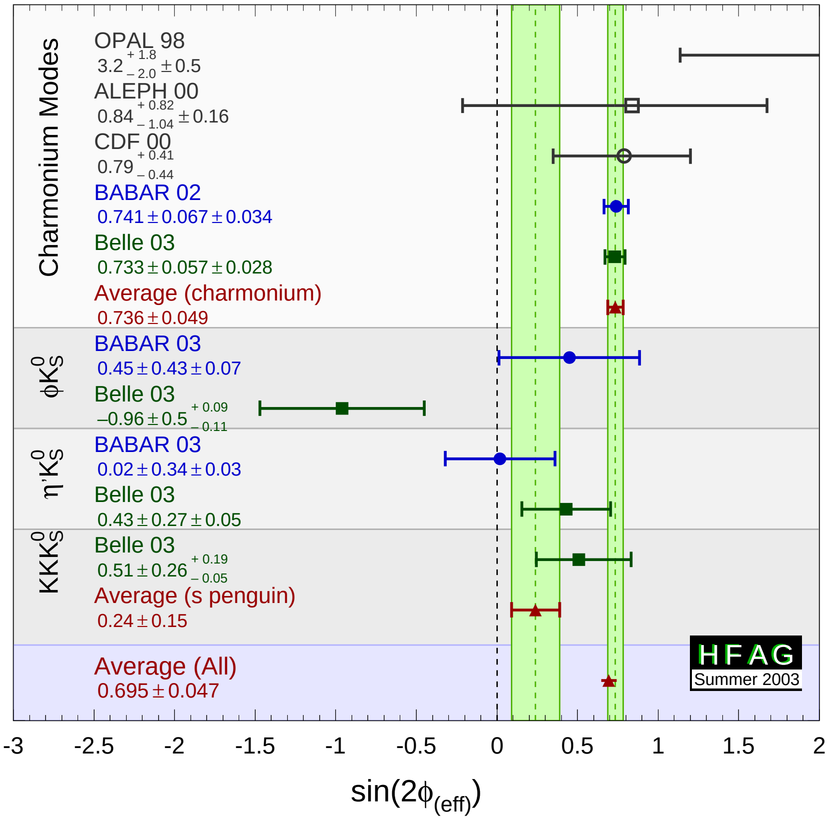

Figure 6.3: Comparison with other experiments.

6.3 Experimental status of unitarity triangle

Figure 6.4 shows the 68% and 95% confidence level intervals of the world-average $\sin 2\phi_1$, together with constraints of $\bar{\rho} - \bar{\eta}$ plane from other measurements of K and B decays. This plot is generated by The Heavy Flavor Averaging Group (HFAG).

1. $|V_{ub}|$ is measured using inclusive and exclusive semileptonic B meson decay, involving $b \rightarrow u$ transition.

2. $|V_{cb}|$ is measured using inclusive and exclusive semileptonic B meson decay, involving $b \rightarrow c$ transition.

3. $|V_{td}|$ can be obtained from B meson mixing measurements. B_d^0 meson mixing is governed by the box diagram shown in Figure 2.4, $\Delta m_d \propto |V_{tb}^* V_{td}|$.

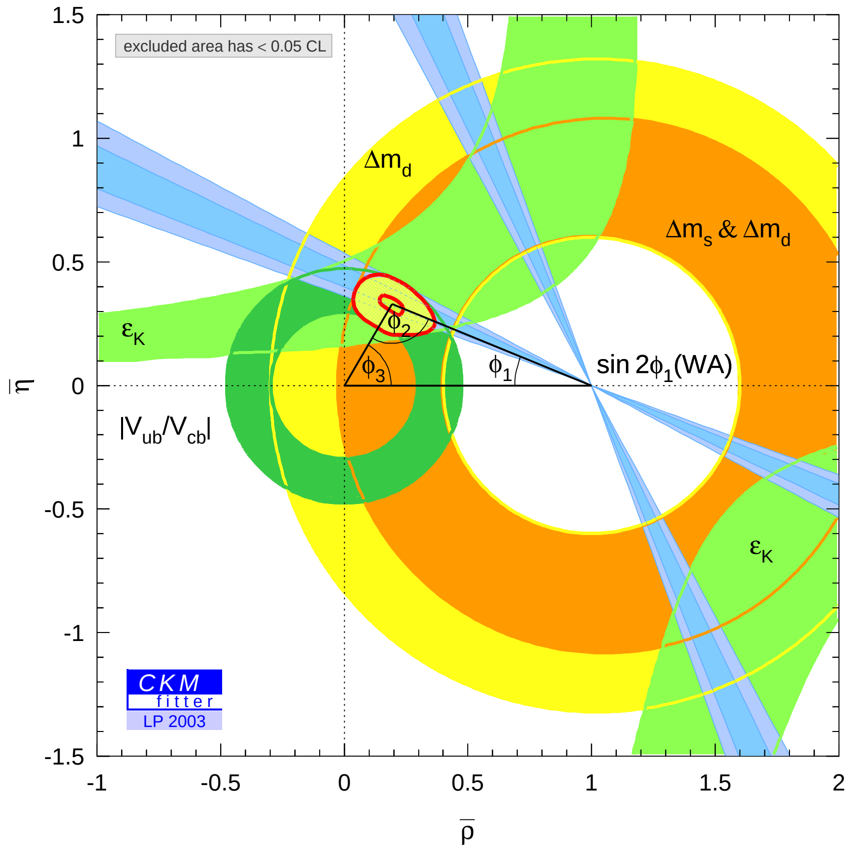

Figure 6.4: $\rho - \eta$ plane with constraints from different measurements. The hatched areas are four ϕ_1 solutions that correspond to the 68% and 95% confidence level intervals of the world-average $\sin 2\phi_1$. The 95% confidence-level regions from other measurements are shown shaded.

We compare our result from B-factory experiment with other experimental results on the $\bar{\rho}-\bar{\eta}$ plane. We find Belle results is shooting the center of the constraint region obtained from other experiments. The KM-mechanism gives a consistent description for the CP-asymmetry.

6.4 Summary

We have measured CP-asymmetry parameter $\sin 2\phi_1$ at the KEKB asymmetric e^+e^- collider using a data sample of $140/fb$ collected at the $\Upsilon(4S)$ resonance with the Belle detector.

We found 2332 candidates of neutral B mesons decaying into the CP-eigenstate $B^0 \rightarrow J/\psi\ K_L^0$, after the event selection and vertex reconstruction. Using these events, we obtain $\sin 2\phi_1$ by unbinned maximum likelihood fit

$$\sin 2\phi_1 = 0.75 \pm 0.13.$$

We also observed $\sin 2\phi_1$ using other CP-eigenstate modes ($B^0 \rightarrow J/\psi\ K_S^0$, $B^0 \rightarrow \psi(2S)\ K_S^0$, $B^0 \rightarrow \chi_{c1}\ K_S^0$, $B^0 \rightarrow \eta_c\ K_S^0$ which CP-eigenstate values are odd):

$$\sin 2\phi_1 = 0.73 \pm 0.06.$$

The result of $\sin 2\phi_1$ using $B^0 \rightarrow J/\psi\ K_L^0$ mode is consistent with the results obtained using other $B^0 \rightarrow c\bar{c}\ K_S^0$. The sign of CP-eigenvalue is clearly opposite each other from the asymmetry distributions. It is verified that KM mechanism describes correctly the CP-violation in the standard model.

Bibliography

[1] A. D. Sakharov, Pisma Zh. Eksp. Teor. Fiz. **5**, 32 (1967).

[2] J. H. Christenson, Cronin, Fitch and Turlay, Phhys. Rev. **13** 138 (1964)

[3] AA. Carter and A.I.Sanda, Phys. Rev. Lett **45** (1980) 952; Phys. Rev. D23, 1567(1981); I.I. Bigi and A. I. Sanda, Nucl. Phys. 193, 851 (1981).

[4] N. Cabibbo, Phys. Lett. **10** 531 (1963)

[5] M. Kobayashi and T. Maskawa, *Prog.Theor.Phys.* **49** 652 (1973)

[6] L. Wolfenstein, Phys. Rev. Lett. **51** 1945 (1983)

[7] S. Kurokawa and E. Kikutani, Nucl. Instrum. and Meth. **A499**, 1(2003).

[8] Belle Collaboration, A. Abashian *et al.*, Nucl. Instrum. and Meth. **A479**, 117(2002).

[9] V.Chabaud *et al.*, Nucl. Instrum. and Meth. **A368**, 314(1996).

[10] G. Alimonti *et al.*, Nucl. Instrum. and Meth. **A453**, 71(2000)

[11] H.Hirano *et al.*, Nucle. Instrum. and Meth. **A455**, 294(2000); M. Akatsu *et al.*, Nucl. Instr. and Meth. **A454**, 322(2000)

[12] T. Iijima *et al.*, Nucl. Instrum. and Meth. **A453**, 321(2000)

[13] K. Kichimi *et al.*, Nucl. Instr. and Meth. **A453**, 315(2000)

[14] H. Ikeda *et al.*, Nucl. Instr. and Meth. **A441**, 401(2000); K. Hanagaki*et al.*, Nucl. Instr. and Meth., hep-ex/010844.

[15] A.Abashian *et al.*, Nucl. Instr. and Meth. **A449**, 112(2000)

[16] K. Hanagaki *et al.*, (Belle KID group), Belle note 321, unpublished.

[17] H. Kakuno, Belle note 384, unpublished.

[18] M. Yamaga, Measurement of CP violation in $B^0 \to J/\psi + K_L$ decay at KEK B-factory, PhD thesis, Tohoku University, 2001.

[19] T. Higuchi, Observation of CP Violation with B^0 Meson Decaying to the $J/\psi Ks$ State, PhD thesis, Univ. of Tokyo, 2002

[20] M. Yokoyama, Observation of Large CP Violation in the Neutral B Meson System Using $B^0 \rightarrow J/\psi K_L Decay$, PhD thesis, Univ. of Tokyo, 2002

[21] S. E. Vahsen Measurement of CP Violation in $B^0 \rightarrow J/\psi K_L Decays$, PhD thesis, Princeton University, 2003

[22] K. Abe *et al.*, Phys. Rev **D66**, 032007(2002).

[23] K. Abe *et al.*, Phys. Rev. Lett **88**, 171801(2002).

[24] K. Abe *et al.*, Phys. Lett **B538**, 11(2002).

[25] A.Alavi-Harati *et al.*,Phys.Rev.Lett.**83**,1,(1999)